SANDIA REPORT

Effect of Dielectric Photoemission on Surface Breakdown: An LDRD Report

Roy E. Jorgenson, Larry K. Warne, Andreas A. Neuber, John Krile, James Dickens and Hermann G. Krompholz

Sandia National Laboratories

Effect of Dielectric Photoemission on Surface Breakdown: An LDRD Report

Roy E. Jorgenson and Larry K. Warne
Electromagnetics and Plasma Physics Analysis Dept.
Sandia National Laboratories
P. O. Box 5800
Albuquerque, NM 87185-1152

Andreas A. Neuber, John Krile, James Dickens and Hermann G. Krompholz
Department of Electrical and Computer Engineering
Texas Tech University
P. O. Box 43102
Lubbock, TX 79409-3102

Abstract

The research discussed in this report was conceived during our earlier attempts to simulate breakdown across a dielectric surface using a Monte Carlo approach. While cataloguing the various ways that a dielectric surface could affect the breakdown process, we found that one obvious effect – photoemission from the surface – had been ignored. Initially, we felt that inclusion of this effect could have a major impact on how an ionization front propagates across a surface because of the following argument chain: (1) The photon energy required to release electrons from a surface via photoemission is less than the photon energy required to ionize gas molecules directly. (2) The mean free path of a photon in gas is longer for low-energy photons than for high-energy photons. (3) Photoionization is a major effect in advancing the ionization front for breakdown in gas without a surface, therefore, we know that even high-energy photons can be released from the head of a streamer and propagate some distance through the gas. Our hypothesis, therefore, was that photons with energies near the threshold of photoemission could travel further in front of the streamer before being absorbed than higher-energy photons needed for photoionization, yet the lower-energy photons, with the help of the surface, could still create seed electrons for new avalanches. Thus, the streamer would advance more rapidly next to a surface than in gas alone. Additionally, the photoemission from the surface would add to the electrons in the avalanche and cause the avalanche to grow faster. After some study, however, we are forced to conclude that although photoemission does contribute to avalanche growth at fields near breakdown threshold, secondary electron emission causes electrons to stick to the surface and cancels out the growth due to photoemission. This conclusion assumes a discharge that occurs over a short period of time so that charging of the surface, which could alter its secondary electron emission characteristics, does not occur. This report documents the numerical work we did on investigating this effect and the experimental work we did on pre-breakdown phenomena in gas.

Acknowledgment

Contents

Figures

Tables

Intentionally Left Blank

Effect of Dielectric Photoemission on Surface Breakdown: An LDRD Report

1   Introduction

One of Sandia's responsibilities is to ensure safety while conducting certain operations involving high explosives during a lightning storm. The procedure is to first determine the highest voltage present inside a reinforced, concrete structure that has been struck by lightning, as shown in Figure 1. In order to prevent breakdown to objects that are sensitive to current flowing through them, such as detonators, a standoff distance is imposed between the sensitive objects and the place where the high voltage exists. The breakdown voltage as a function of electrode distance is well known for parallel-plate geometries and for certain non-uniform geometries (rod-plane, sphere-sphere, etc...)[1]. Many times, however, a dielectric surface is present in the vicinity of the electrodes, which modifies not only the fields between the electrodes, but serves as a possible source or sink of electrons during the breakdown process. In Figure 1, for example, we see that a dielectric strap isolates a crane hook, which is at a high voltage, from a sensitive object being lifted. We also see a dielectric spacer that isolates a piece of equipment from the sensitive object. The equipment is connected to the power grid and subject to high-voltage surges due to a lightning strike. Finally, we see a dielectric table surface, which may cause us to modify the imposed standoff distance from the high-voltage wall to the sensitive object.

Another Sandia responsibility is to predict the breakdown path in certain components that are exposed to high voltage due to lightning strike or unintentionally applied AC power lines. Figure 2 shows a connector cross section where high voltage on one line breaks down to another line over the dielectric face of the connector. The wire-to-wire path may be of concern for safety. Another breakdown path shown in Figure 2 involves breakdown through wire insulation that has cracked due to aging. The wire-to-shell path may be of concern for reliability. In both of these cases, the dielectric surface is on both sides of the breakdown path.

The above examples are just a few of the many practical applications where knowledge of breakdown across a dielectric surface at atmospheric pressure is important. In 1998 we began to study this problem and found that the literature was empirical in nature and there was disagreement about whether the dielectric raised or lowered the breakdown voltage. Figure 3, for example, which is widely quoted in breakdown literature [2],[3], shows the breakdown field as a function of gap distance between two parallel-plate electrodes, with and without a dielectric spacer bridging the gap. The figure indicates that the dielectric surface reduces the breakdown voltage by as much as a factor of two. Later we found that the original paper giving these results was focused on the effect of humidity on breakdown and the indicated drop in breakdown voltage was explained by humidity on the surface of the dielectric [4].

In order to study the breakdown process we simulated the growth of an avalanche across a dielectric surface using a Monte Carlo technique [5]. During the course of that work, it became obvious that we had missed an effect that could play a major role in the propagation of an avalanche across a dielectric surface – that of photoemission from the surface. This report documents extensions made to the Monte Carlo code to account for photoemission and experiments that were performed at Texas Tech University to discover the effect a dielectric surface has on pre-breakdown phenomena.
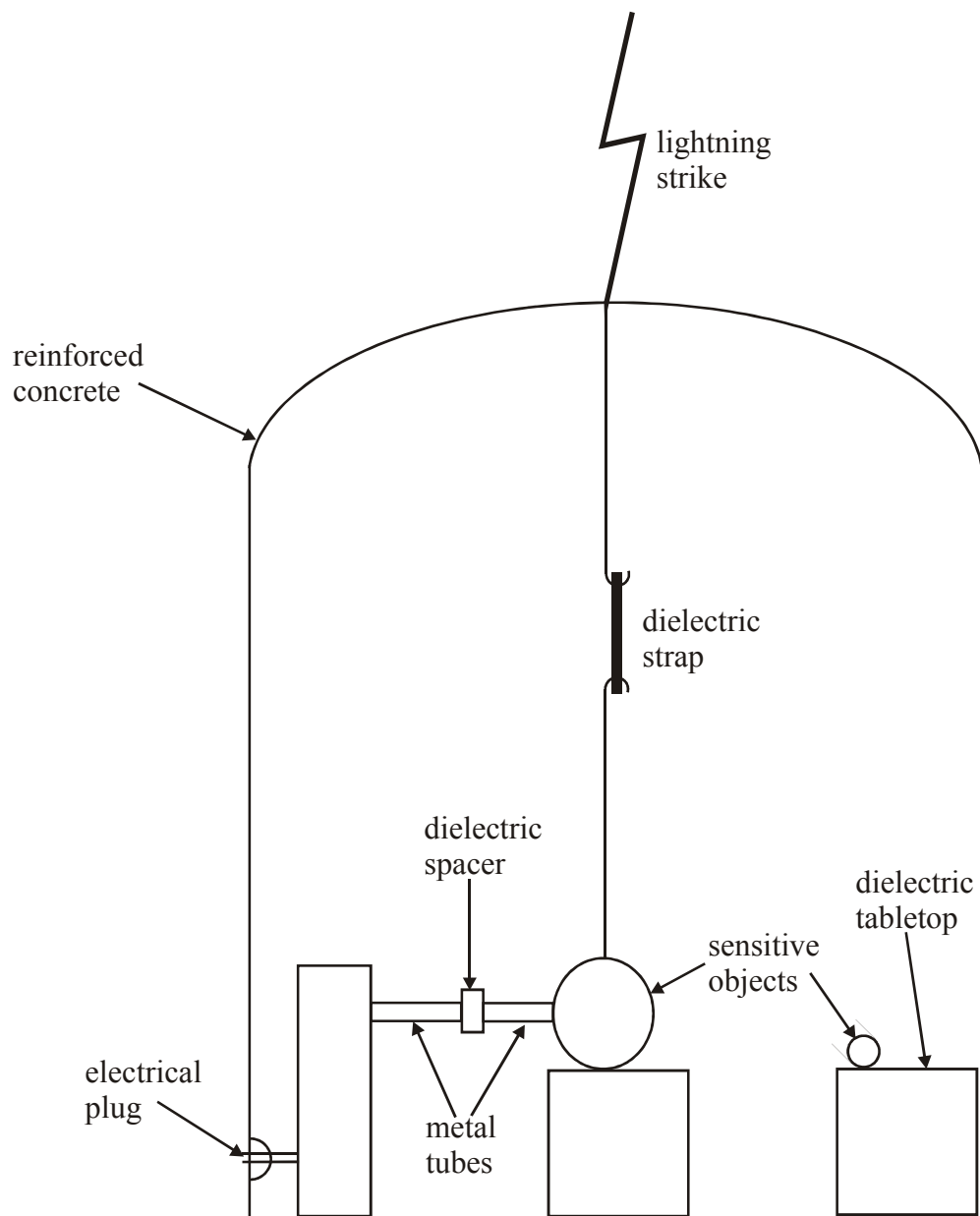
Figure 1. Breakdown Across Dielectrics in an Explosive Handling Bay

dielectric

connector
shell

breakdown
path across
connector face

breakdown path
through crack

V
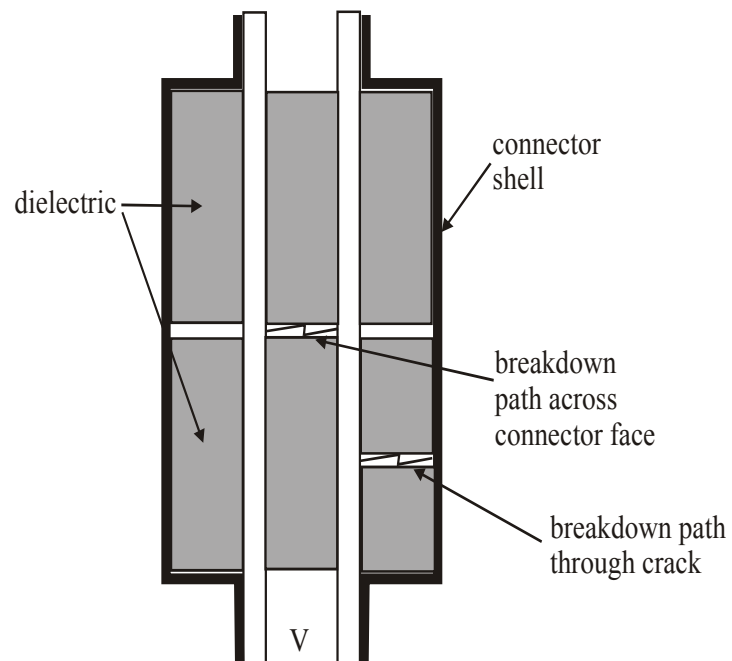
Figure 2. Connector Breakdown
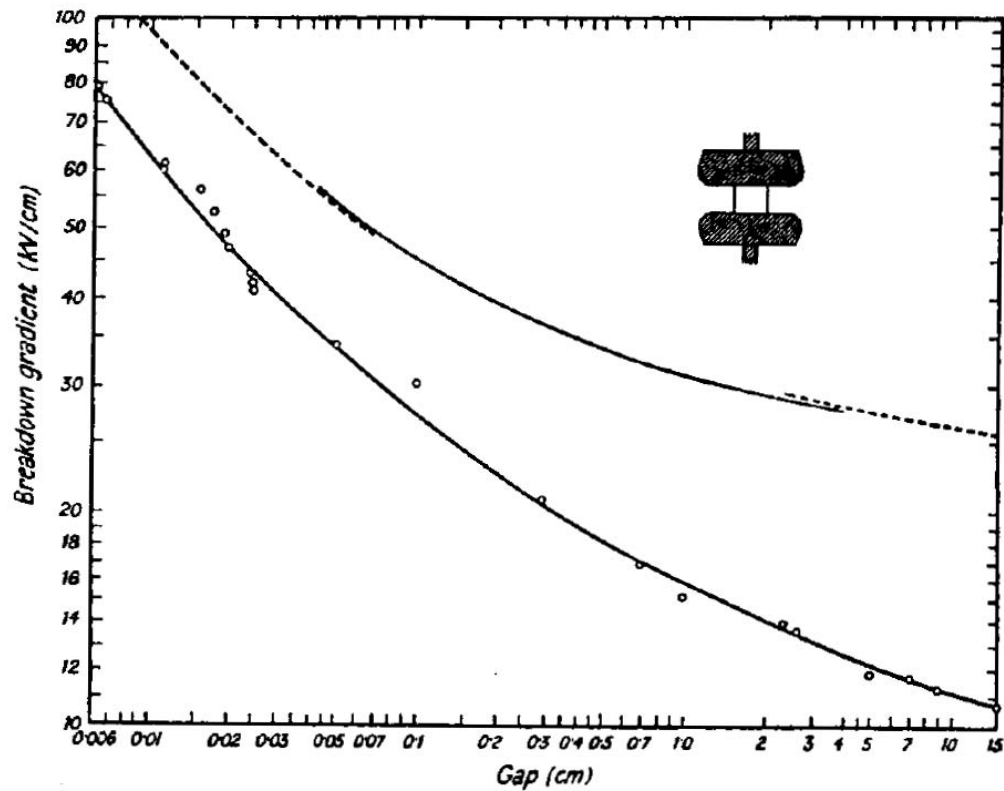
FIG. 7.35. 60 c./s. breakdown voltage characteristic for the sparkover across the surface of a glass or porcelain cylinder in air. The upper curve gives the breakdown characteristic of a uniform field in the absence of the cylinder.

Figure 3. Breakdown Voltage versus Distance With and Without Dielectric Spacer [2]

18

Dielectric Half-space
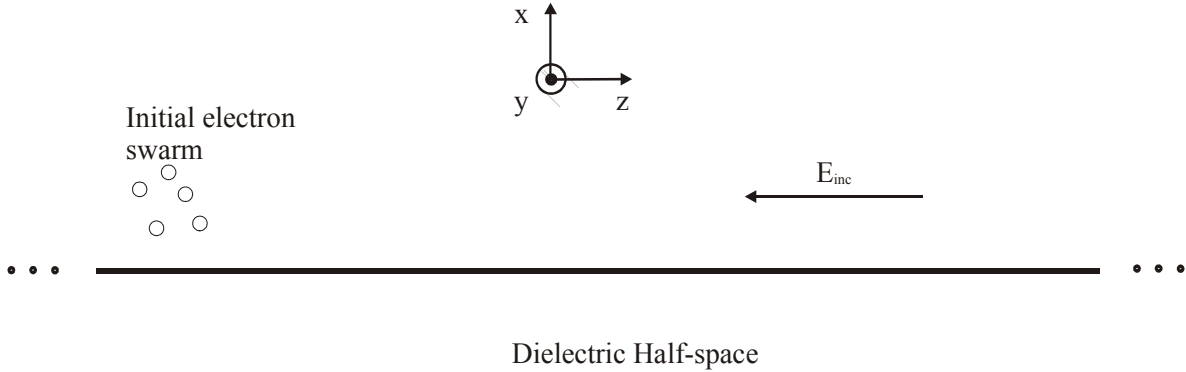
Figure 4. Simplified Problem Geometry

2 Problem Description

As seen in the previous section, the geometries that we are actually concerned with involve breakdown across complex surfaces with complex electrodes that lead to highly non-uniform fields. In order to study the problem, however, we will simplify the geometry to one of an infinite, dielectric, half-space with no electrodes as shown in Figure 4. A uniform electric field, $\overline{E}_{inc} = -\hat{z}E_{inc}$ is applied parallel to the surface of the dielectric, which fills the region $x \leq 0$. At time $t = 0$, a small number of initial electrons (~ 10) uniformly distributed in a small sphere about the origin (radius $\sim 1\mu$m), are allowed to move in the electric field. We track the progress of each individual electron as it is accelerated by the electric field and undergoes collisions with the background neutral gas molecules and with the dielectric surface using the Monte Carlo computer code described in [5]. We can thus observe the behavior of the electron swarm as the breakdown develops.

3 Description of Effect of Dielectric Photoemission

As the electrons are released, they are accelerated by the electric field until they collide with one of the neutral gas molecules. Initially, the electron energy is low enough that most of the collisions are elastic. As the electron energy increases, the collisions become inelastic, transferring energy to and exciting the neutral gas molecule. Eventually, the electron energy becomes large enough that the collision ionizes the neutral, which adds to the number of electrons in the problem. The ionizing collisions lead to an exponential growth in the number of electrons, which is called an electron avalanche.

When a high-energy collision occurs, a photon may be released which has enough energy to ionize a second neutral at some distance from the collision site. The photoionization site serves as a seed electron for a new avalanche. As the avalanches coalesce, they form ionization wavefronts called streamers that propagate toward both the cathode (at approximately 1×10^8 to 4×10^8 cm/s) and anode (at approximately 1.5 to 2 times the speed of the cathode-directed streamer) [6]. This process is shown in Figure 5.

The photons energetic enough to ionize a neutral (15.5 ev in N_2) need a high energy collision in order to form, and therefore, are not common. Second, high energy photons are readily absorbed in gas at atmospheric pressure [7]. Lower energy photons are more numerous and are not as readily absorbed, but do not have the energy to ionize a gas neutral directly. When a dielectric surface is introduced, however, an electron may be released from the surface when a lower energy photon strikes the surface. In polyethylene, for example, the band gap is 4 ev and work function is 4.5 ev [8], so an 8.5 ev photon should have the energy
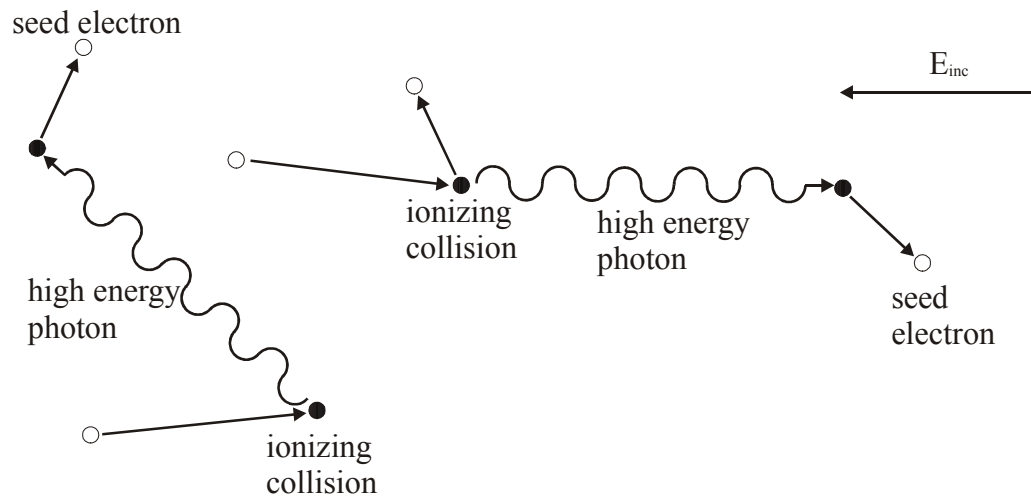
Figure 5. Photoionization Process

exciting
collision

lower-energy
photon

E_{inc}

photoemission

Dielectric Half-space
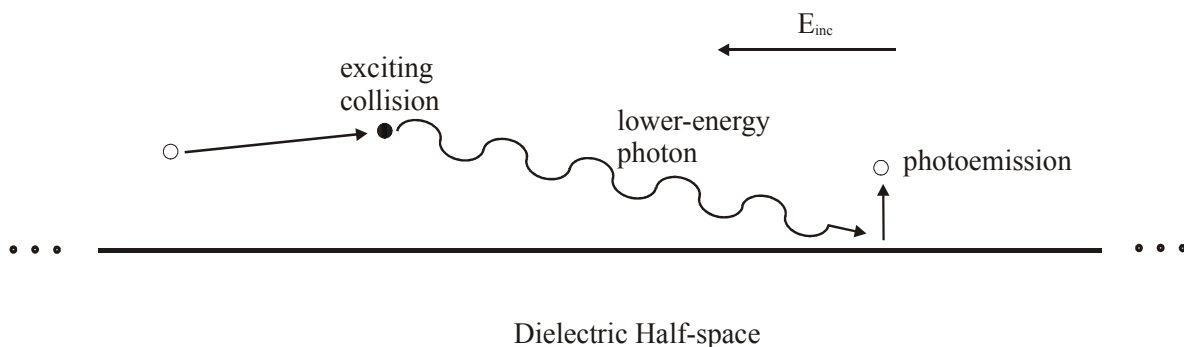
Figure 6. Dielectric Photoemission Process

to release an electron from the dielectric surface, which will serve as a seed for a new avalanche. Because the lower energy photons associated with photoemission can travel farther before being absorbed than the higher energy photons associated with photoionization, it is postulated that an ionization wave next to a surface will travel with greater velocity than an ionization wave without a surface. Also, since the surface serves as a source of electrons, the number of electrons as a function of distance that the avalanche travels should also increase. This process is shown in Figure 6.

Of course the introduction of the surface introduces other processes that could serve as a sink or source of electrons. We will use the Monte Carlo code to evaluate the effect of each of these processes.

4 Past Work

Evidence that photoemission affects breakdown across a dielectric surface can be found in the literature. Mahajan and Sudarshan [9] compared electron and ion avalanches in a parallel-plate gap bridged by different solid insulators to avalanches in an unbridged gap. The gap was 1 cm wide in nitrogen and the insulator materials included Plexiglas, polyethylene, Teflon, nylon and PVC. At the same time they measured the optical activity associated with the avalanche.

For most insulator samples tested, they found that the growth of the primary electron avalanche was slightly inhibited by the presence of the insulator. The growth of the primary ion avalanche was unaffected. Secondary avalanches in a Townsend type discharge were strongly suppressed by the presence of the insulator. Photon activity was also suppressed by the insulator. The suppression of the various avalanches was attributed to a buildup of surface charge on the insulator.

If the bridging insulator was made of nylon, the results were found to be quite different. The growth of the primary electron avalanche was much larger across the nylon insulator than in a plain gas gap. In the plain gas gap, the growth was exponential in nature, but this was not true for the nylon bridged gap. The presence of nylon substantiality widened the pulsewidth of the avalanche. The ion avalanche remained unaffected. During the entire avalanche, there was photon activity. The nylon bridged gap had a breakdown voltage approximately half that of the unbridged gap.

Photoemission was proposed as the explanation for the strange behavior of nylon. The work function of a dielectric is low (5-10 ev) compared to the ionization potential of nitrogen (15 ev). The seeding of new avalanches due to photoemission causes the avalanche pulse to be spread out. Since there was no increase in number of ions, competing processes such as photoionization of the gas or additional electrons emitted from the cathode due to ion impact can be ruled out. If the avalanche was started a few millimeters

away from the surface, the large electron avalanche was not observed indicating that the surface affects the breakdown. The authors did not explain why nylon was the only insulator to exhibit this behavior.

Tom et al. [10] looked at flashover voltage of insulators bridging a nitrogen or argon gap between plane electrodes. The insulators were quartz filled epoxy resin, unfilled epoxy resin and Teflon. They found that if the insulator was pre-charged with positive or negative charge using a corona, the breakdown voltage was lower than that of an uncharged insulator. They attributed this to photoemission from the surface that provided an extra electron contribution to the primary avalanche.

Verhaart et al. [11] examined avalanche growth next to a Teflon insulator in N_2, CO_2, and SF_6. They assumed that three processes were active in the avalanche: ionization, attachment and photoemission. They measured the total growth coefficient, obtained the ionization and attachment coefficient from literature and assumed the remaining component was due to photoemission from the insulator. They found no photoemission effect in CO_2. They attributed this to the fact that the spectrum of CO_2 exhibits no emission in the energy range greater than 6 ev and Teflon has a small quantum yield when the photons have energies less than 6 ev. In N_2 photoemission was observed if the insulator was negatively charged prior to conducting the experiment. No photoemission was observed if the insulator was positively charged or was neutral. In SF_6 photoemission was observed no matter how the insulator was charged. Both N_2 and SF_6 have a spectrum with emission in the 10 ev range, where the quantum efficiency of Teflon is high enough to exhibit photoemission.

Jaksts and Cross [12] measured avalanches across polyethylene and Teflon insulators in N_2. In an N_2 gap without an insulator they measured a primary avalanche and secondary avalanches that originated from the cathode due to photoemission. In the bridged gap, they measured additional avalanches that they attributed to photoemission from the insulator surface initiated by photons from the primary avalanche from an excited state having a lifetime of 20 μs. Both spacers gave similar results, indicating that the exciting mechanism was the same in the gas. They also determined that the insulating surface did not affect the primary avalanche significantly.

Allen et al. [13],[14],[15] studied the propagation of streamers across a parallel-plate air gap bridged by different solid insulators, 12 cm thick (insulator materials included Teflon, nylon and glazed ceramic). The streamer was formed by imposing a positive pulsed voltage on a point electrode located in a small aperture cut in the anode. They noted that the streamer propagated across the insulator with two components. One had the same speed as that of gas alone and the other was faster The fast component was offered as evidence that photoemission was an important effect at the surface. They also measured the minimum field needed to propagate the streamer across the gap as being 400 kV/m in air. The bridged gaps needed a higher field to propagate the streamer.

5 Dielectric Surface Effects Included in the Calculation

In the following sections we will discuss three ways that the dielectric surface can affect the growth of a nearby avalanche. We included these effects in the Monte Carlo code.

5.1 Electric Field Modification

If the dielectric modifies the electric field in any way, nearby avalanches would be affected. First, since charged particles travel along electric field lines, a change in field direction could cause the particles to collide with (or be directed away from) the dielectric surface, causing a change in secondary emission characteristics. Secondary emission will be discussed in the next section. Second, it is well known that the

rate of avalanche growth is exponentially dependent on the magnitude of the electric field [16]. Therefore, if the dielectric increases the electric field, even slightly, we expect the avalanche to grow more rapidly.

The infinite, dielectric half-space described in Figure 4 does not modify the applied electric field $\left(\overline{E}_{inc}\right)$, since it is assumed to be tangential to the dielectric surface and tangential fields are continuous across a dielectric interface. The electric field due to a charge located above the surface, on the other hand, has a component normal to the surface and is, therefore, modified by the dielectric. This field can be calculated simply by using images – the dielectric is eliminated and the field due to the original charge is added vectorially to the field due to the image charge. Each charged particle q located at (x, y, z), where $x > 0$, has an image particle located at $(-x, y, z)$. The image particle has a charge of

$$q' = \frac{1 - \epsilon_r}{1 + \epsilon_r} q$$

where ϵ_r is the relative permittivity of the dielectric [17].

5.2 Secondary Electron Emission

As the electrons collide with the dielectric surface, they either stick to the surface, charging it negatively, or release secondary electrons from the surface leaving behind positive charge. This process is known as secondary electron emission. The number of secondary electrons released from the surface per incident primary electron (δ) is plotted as a function of the primary electron energy in Figure 7. Note that the energy regions $\varepsilon < \varepsilon_I$ and $\varepsilon > \varepsilon_{II}$ (where $\delta < 1$), are where the primary electrons stick to the surface. Note also that there is a maximum number of secondary electrons released from the surface (δ_m), which occurs when the primary electron has an energy of ε_m.

A simple, one-dimensional model of secondary electron emission, where the secondaries are assumed to exit the dielectric along the same direction as the incident primaries, is derived following the method of Dionne [18]. The definition of secondary emission is

$$d\delta = N(x, \varepsilon)f(x)dx \tag{1}$$

where $N(x, \varepsilon)$ is the average number of secondaries produced per incident primary of energy ε in the layer having thickness dx located a distance x into the dielectric from its surface. $N(x, \varepsilon)$ is assumed to be proportional to average energy loss per unit path length

$$N(x, \varepsilon) = -\frac{1}{\zeta}\left(\frac{d\varepsilon}{dx}\right) \tag{2}$$

where ζ is the energy required to excite one secondary electron in the solid.

The factor $f(x)$ is the probability that a secondary migrates to and escapes from the surface.

$$f(x) = Be^{-ax} \tag{3}$$

where B is the escape probability and e^{-ax} is the migration probability. The parameter a is the absorption constant. Substituting Equations 3 and 2 in Equation 1 and integrating over the depth d, which represents the maximum depth that the primaries can penetrate, we obtain

$$\delta = -\frac{B}{\zeta}\int_0^d \left(\frac{d\varepsilon}{dx}\right)e^{-ax}dx \tag{4}$$

A basic assumption of secondary electron emission theory is that a primary electron loses its energy as it penetrates the dielectric according to a power law

$$\frac{d\varepsilon}{dx} = -\frac{A}{\varepsilon^n} \tag{5}$$

where A is a constant characteristic of the material and $n > 0$. Solving Equation 5 we obtain an expression
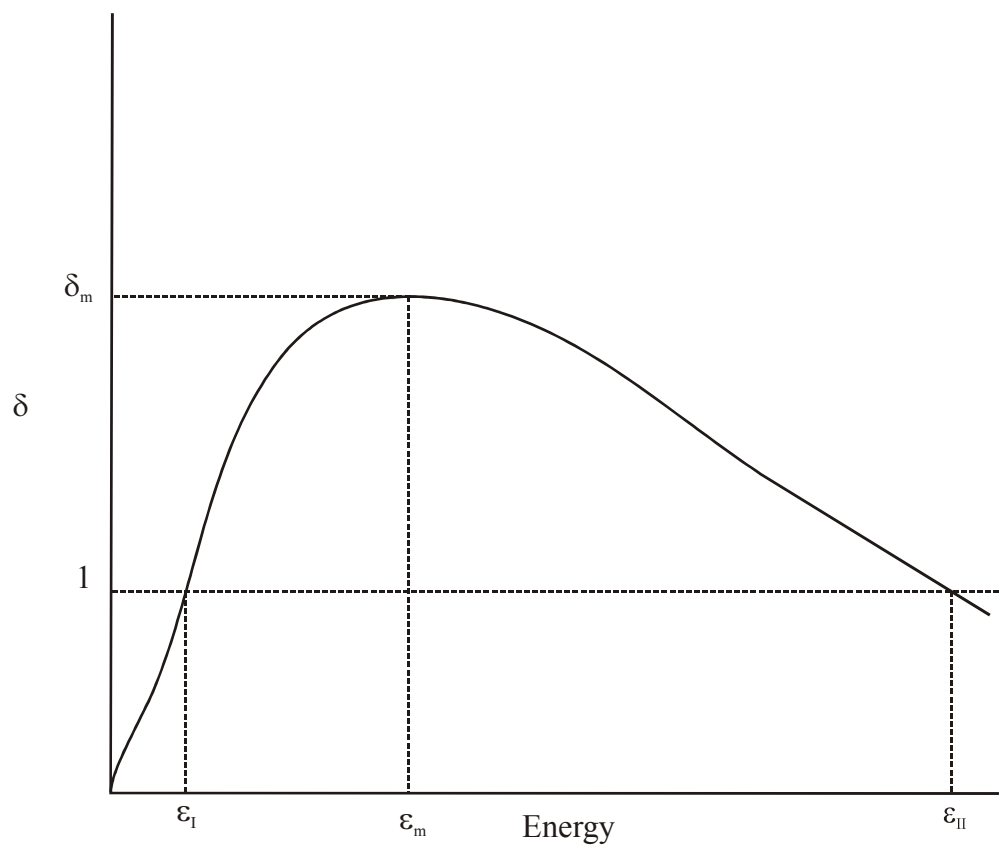
Figure 7. Sample Secondary Electron Emission Curve

for the energy of the electron

$$\varepsilon^{n+1}(x) = \varepsilon_p^{n+1} - A(n+1)x$$

where ε_p is the energy of the primary at $x = 0$. The maximum penetration depth d can be found by finding the value of x where $\varepsilon^{n+1}(x) = 0$ or

$$d = \frac{\varepsilon_p^{n+1}}{A(n+1)} \tag{6}$$

One model of secondary electron emission is called the power law model. It assumes that all primaries reach depth d. On their way they release energy in accordance with Equation 5. In this report we will use the constant loss model. It assumes that not all the primaries reach depth d because some of them are scattered. The energy of each individual electron still follows Equation 5 but the electrons being scattered cause the average energy loss throughout the range to be constant [19], i.e.,

$$\left\langle \frac{d\varepsilon}{dx} \right\rangle = -\frac{\varepsilon_p}{d} \tag{7}$$

Note that the number of primaries decreases linearly with respect to depth and because of Equation 2 the number of secondaries is constant with respect to depth. Substituting Equation 7 into Equation 4 and performing the integration we obtain

$$
\begin{aligned}
\delta &= -\frac{B}{\zeta} \int_0^d \left\langle \frac{d\varepsilon}{dx} \right\rangle e^{-ax} dx \\
&= +\frac{B}{\zeta} \frac{\varepsilon_p}{d} \int_0^d e^{-ax} dx \\
&= +\frac{B}{\zeta} \frac{\varepsilon_p}{d} \frac{1 - e^{-ad}}{a}
\end{aligned}
$$

Recall from Equation 6 that $\varepsilon_p = ((n+1)dA)^{1/(n+1)}$ so

$$
\begin{aligned}
\delta &= \frac{B}{\zeta} \frac{((n+1)dA)^{1/(n+1)}}{d} \frac{1 - e^{-ad}}{a} \tag{8} \\
&= \frac{B}{\zeta} \left(\frac{A(n+1)}{a} \right)^{1/(n+1)} \frac{(d)^{1/(n+1)}}{(a)^{1-1/(n+1)} d} 1 - e^{-ad} \\
&= \frac{B}{\zeta} \left(\frac{A(n+1)}{a} \right)^{1/(n+1)} \frac{1 - e^{-ad}}{(ad)^{n/(n+1)}}
\end{aligned}
$$

The quantity ad can be related to the energy of the primary particle (ε_p) by Equation 6, therefore,

$$
\begin{aligned}
ad &= \frac{a}{A(n+1)} \varepsilon_p^{n+1} \\
&= K^{n+1} \varepsilon_p^{n+1}
\end{aligned}
$$

where $K = [a/A(n+1)]^{1/(n+1)}$ is a constant. Letting $Z = K\varepsilon_p$, we substitute $ad = Z^{n+1}$ in Equation 8 and obtain

$$\delta = \frac{B}{\zeta} \left(\frac{A(n+1)}{a} \right)^{1/(n+1)} \frac{1 - e^{-Z^{(n+1)}}}{Z^n}$$

Measurements of secondary electron emission from metal, inorganic insulators and polymer insulators indicate that if the secondary electron emission curves are plotted as a function of $\varepsilon_p/\varepsilon_m$ and normalized so that the maximum value attained is 1, the resulting curve applies to a wide range of materials in a given class. In this way we obtain a universal yield curve, which can be used to obtain the secondary electron
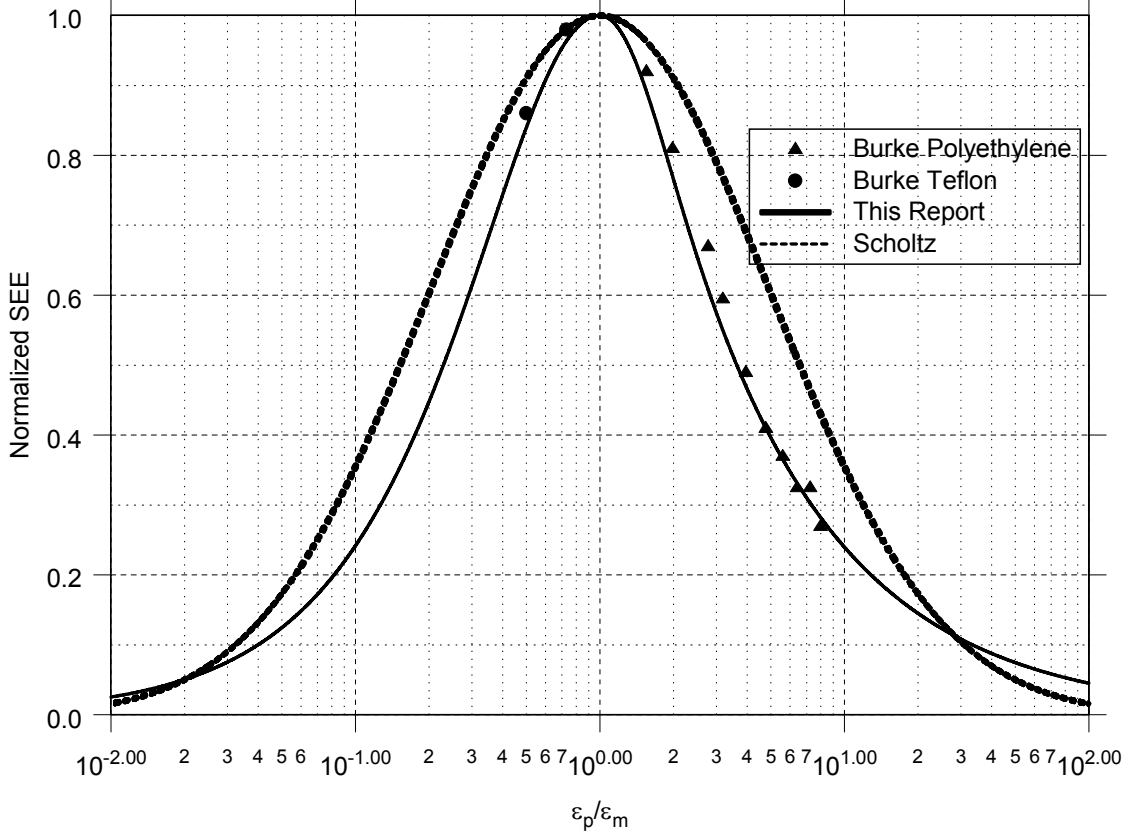
Figure 8. Normalized Secondary Electron Emission

emission curve for a particular material if we substitute the material's values of δ_m and ε_m. The universal curve for different classes of material (metal, inorganic insulator, or polymer) is found by matching various values of n to experimental data. First we define the function

$$g_n\left(Z\right) = \frac{1 - e^{-Z^{(n+1)}}}{Z^n}$$

Then the universal yield curve is

$$\frac{\delta}{\delta_m} = \frac{g_n\left(Z_m\varepsilon_p/\varepsilon_m\right)}{g_n\left(Z_m\right)}$$

where Z_m is the value where $g_n\left(Z\right)$ reaches its maximum. Note that the argument of the numerator is such that when ε_p equals ε_m, the quantity δ/δ_m equals one, as required. Below $\varepsilon_p/\varepsilon_m = 1$, we set $n = 0.35$. to match the data in Scholtz [21], who we found had the most complete secondary electron emission data over the low energy range. Above $\varepsilon_p/\varepsilon_m = 1$, we set $n = 0.725$ to match the data found in Burke [20], who had data in the high energy range for a number of polymers. The resulting curve is shown in Figure 8 along with normalized experimental data from Burke and Scholtz.

The low energy range (0 to 50 ev) is of greatest interest to us because these are typical energies of electrons in the avalanche. Unfortunately, most studies on secondary electron emission are in the high

Material	δ_m	ε_m	ϵ_r
Polyethylene	2.71	250	2.25
Teflon	2.12	400	2.1
Nylon	2.42	250	3.88

Table 1.Polymer Secondary Electron Emission Parameters [20]

energy (Kev) range because of their role in scanning electron microscopes. We assume that the parameters given in Table 1 taken from the high-energy studies of Burke [20] and Willis and Skinner [22] apply also to lower energy electrons.

We had implemented this effect previously in the Monte Carlo code [5] using a crude linear approximation of the curve. We had specific data for traditional insulators, such as glass, and mica, but none for polymers. After we implemented the photoemission models discussed below, it became apparent that secondary electron emission served as a sink of electrons while photoemission served as a source. Since these two effects balanced each other, we had to make the secondary electron emission models more accurate and find secondary emission data for polymers – the material that exhibited photoemission.

5.3   Photoemission

This section discusses how we implemented photoemission in the Monte Carlo code. Photoemission consists of three phases: First, an electron collides with a gas molecule which excites and in the process of returning to the ground state emits a photon with a given energy. The photon then propagates through the gas and hits the surface. Finally, the surface emits an electron, which serves as a seed for a new avalanche.

5.3.1 Photon Emission due to Collision

As the electron passes through N_2 gas, collisional cross section data are used to determine if the electron collides with a neutral, and if so whether it is scattered elastically, whether it excites the neutral, or whether it ionizes the neutral [5]. If the neutral is excited by the collision, further cross section data exist which predict the neutral's new energy level. The cross section data used in this report were obtained by numerically integrating measurements of differential cross section, which were, in turn extracted from electron energy loss data over a range of angles [23]. This method yields the absolute cross section for a given energy level, separating the direct excitation of the level (from the ground level) and the cascade excitation of the level (from higher energy energy levels). Another method of obtaining the cross section is to pass electrons of known energy through the gas and measure the absolute intensity of the radiation produced [24]. This method measures the apparent cross sections and is unable to separate the direct from the cascade contributions. For this report, the apparent cross section is preferable because we are interested in knowing what photons are released due to a collision regardless of how the energy levels were excited. We could only find apparent cross section data on three levels, however, $(C^3\Pi_u, B^3\Pi_g, a^1\Pi_u)$ and we were forced to use the more complete (eleven levels) absolute cross section data [23].

Once the neutral is in an excited level it returns to the ground level via a series of energy loss mechanisms one of which is radiation of a photon. Other non-radiative processes, such as molecular disassociation or vibration, compete with radiation to de-excite the molecule. For radiation to occur, the non-radiative processes must be slower and this is usually not the case. Typical times to radiate are $10^{-9}s$, while typical times for vibrational de-excitation are $10^{-13}s$. Therefore, most molecules absorb photons, but do not emit them. Also, the energy re-radiated from an excited molecule is usually far less than the energy absorbed. [25]

Because of the complexity in the emission of radiation, we will apply two types of bounding

Figure 9. N_2 Energy Level Diagram [26]

approximations when obtaining results. In the first case we will assume that once a collision that excites the neutral to a higher energy level occurs, all the energy lost by the electron is immediately returned in the form of a single photon having an energy equal to that of the threshold energy – the energy that the colliding electron lost during the collision. For example, if a collision excites the N_2 molecule to the $C^3\Pi_u$ level, (see Figure 9 and Table 2, column 2), a single photon is created having an energy of 11.03 ev. This bounding assumption maximizes the photon energy.

In a second case, which is still bounding but more realistic, a number of photons are released immediately during the neutral's return to the ground level. The wavelengths of the photons are within the known spectral bands associated with the original energy level and the lower energy levels the neutral could de-excite to on its way back to the ground state. To roughly account for the fact that some of the energy could go into non-radiating processes, the photon energy is picked to be uniformly distributed within the energy range of the spectral band. For example, if a collision excites the N_2 molecule to the $C^3\Pi_u$ level, (see Figure 9 and Table 2, column 4), three photons are created. The first, which has an energy uniformly distributed between 2.27 and 4.63 ev, corresponds to de-excitation from $C^3\Pi_u$ to $B^3\Pi_g$ (Second

Energy Level Label	Threshold Energy (ev)	Spectral Band	Photon Energy Range (ev)
$A^3\Sigma_u^+$	6.17	Vegard-Kaplan	2.33 - 9.92
$B^3\Pi_g$	7.35	First Positive	0.49 - 2.59
		Vegard-Kaplan	2.33 - 9.92
$W^3\Delta_u$ (not shown)	7.36	Saum-Benesch	8.24 - 8.61
$B'^3\Sigma_u^-$	8.16	Ogawa-Tanaka-Wilkinson	5.54 - 11.07
$a'^1\Sigma_u^-$	8.40	Wilkinson-Mulliken	6.20 - 11.48
$a^1\Pi_g$	8.55	Lyman-Birge-Hopfield	4.77 - 12.40
$w^1\Delta_u$	8.89	McFarlane Infrared	0.15 - 0.41
		Lyman-Birge-Hopfield	4.77 - 12.40
$C^3\Pi_u$	11.03	Second Positive	2.27 - 4.63
		First Positive	0.49 - 2.59
		Vergard-Kaplan	2.33 - 9.92
$E^3\Sigma_g^+$	11.88	Herman-Kaplan	4.53 - 5.82
		Vergard-Kaplan	2.33 - 9.92
$a''^1\Sigma_g^+$	12.25	Dressler-Lutz	12.27
Singlet Systems	13.0	Gaydon-Herman	3.38 - 5.59
		Lyman-Birge-Hopfield	4.77 - 12.40
Singlet - Ground	13.0	Various names	9.54 - 15.50

Table 2.Excitation Energy Levels and Spectral Bands

Positive). The second, which has an energy uniformly distributed between 0.49 and 2.59 ev, corresponds to de-excitation from $B^3\Pi_g$ to $A^3\Sigma_u^+$ (First Positive). Finally, the third electron, which has an energy uniformly distributed between 2.33 and 9.92 ev, corresponds to de-excitation from $A^3\Sigma_u^+$ to the ground state (Vergard-Kaplan). Some of the states are meta-stable, which means that the neutral can remain in that state for a long period without releasing the photon, but as a bounding approximation we allowed the decay to occur immediately.

The eleven cross sections used in this report are summarized in Table 2. The first column gives the name of the energy level to which the neutral is raised. The second column gives the threshold energy of the cross section. The third column gives the name of the spectral band associated with de-excitation from this energy level (and levels below it) and the fourth column gives the energy range of the spectral band. The spectral band information was found in [26] and [27]. The last three rows of the table deserve comment. In all the other rows, if there were two paths that the neutral could take back to the ground state, one was associated with a strong system and the other was associated with a weak system. We chose the path containing the strong spectral band. In this case, both systems were weak so we included both systems and used a uniformly distributed random variable to choose between the two with equal weighting.

5.3.2 Propagation of Photons through Gas

Once the photon is released at the collision site it propagates in a direction uniformly distributed over 4π steradians of solid angle. Half of the created photons propagate away from the surface and leave the problem space. The remaining photons intersect the surface at some location based on the direction of travel and the location of the collision point above the surface.

We assume that as the photon travels toward the surface, it moves a distance r through N_2 that is in the ground state. As the photon interacts with an N_2 neutral it raises the neutral to an excited state, but this time, unlike the electron collision process, we assume that the neutral does not re-radiate the photon, but rather de-excites through non-radiative processes. This is consistent with what is known about photon

behavior in this energy range: that luminescence in the far-ultraviolet range due to absorption is rare [25] and fluorescence requires photons having wavelengths less that 661 Angstroms (Å) [28], which are higher energy (18.8 ev) than the photons generated by the collision cross sections. Therefore, as the photon travels through the gas, it is absorbed with some probability.

Figure 10 shows the absorption coefficient (κ_{stp}) of N_2 as a function of wavelength in the 600 - 1000 Å range [29]. Figure 11 shows the 900 - 1000 Å absorption characteristics in greater detail. Strong, sharp absorption bands exist from 1000 to 796 Å. At wavelengths shorter than 796 Å, a slowly increasing absorption that underlies the band structure occurs due to the ionization continuum. The presence of this continuum effectively absorbs all photons having wavelengths less than 796 Å within 10 μm of the place where the photon is created. There are other continuums due to disassociation that start to occur at 970 Å, but these are relatively weak $(\kappa_{stp} = $ 5-15 cm$^{-1})$ [31]. Weak absorption has been observed at wavelengths longer than 1000 Å with absorption coefficients of the strongest bands (1000 - 1040 Å) less than 0.5 cm^{-1}. We therefore ignore absorption of wavelengths longer than 1000 Å. This data was scaled to be valid at standard temperature and pressure (760 Torr, 273^{0}K) so in order to use this data at other pressures and temperatures

$$\kappa = \kappa_{stp}\frac{p}{760}\frac{273}{T}$$

where p is the gas pressure in Torr and T is the temperature in degrees Kelvin.

The absorption coefficient reduces the light intensity I exponentially as it travels the distance r.

$$I = I_0 e^{-\kappa r}$$

On a per photon basis this is implemented by generating a random number Y having an exponential distribution

$$Y = -\frac{1}{\kappa}\ln(X)$$

where X is distributed uniformly between 0 and 1.0 and rejecting all photons where $Y < r$.

5.3.3 Emission of Electrons from Surface

When a photon of sufficient energy hits a surface, an electron is emitted. In metals, the photon must have enough energy to overcome the work function of the surface (typically around 2.5 ev) [33]. In polymers, the photon must have enough energy to move the electron from the valence to the conduction band across the band gap (4 ev) and then overcome the work function (4.5 ev) [34]. There is evidence that 4 ev will release electrons from the surface of certain polymers, but the quantum yield is very low $(10^{-11} - 10^{-10})$ [35].

When an electron is released from metal, another electron in the conduction band takes its place so that the metal remains neutral. When an electron is released from a dielectric, however, the surface of the dielectric remains positively charged, which could have an effect on subsequent release of electrons from a photoemission site during breakdown. The charging of the surface is such a powerful effect that measuring the photoemission is problematic – the experimentalists have to use thin films of dielectric over metal electrodes[36], use a new dielectric sample for each measurement [35], or neutralize the positive charge with a spray of electrons [37].

Fujihira found that over a given energy range, the cube root of the quantum yield of a polymer plotted as a function of photon energy was linear [8]. We also note that if the photon energy becomes high enough, the quantum yield saturates at a fixed value [37][10]. Therefore, we chose the following fit function to calculate the quantum yield:

$$Q = \begin{cases} 0 & \text{if } E_p < E_l \\ [s(E_p - E_l)]^3 & \text{if } E_l < E_p < E_b \\ Q_s & \text{if } E_b < E_p \end{cases}$$
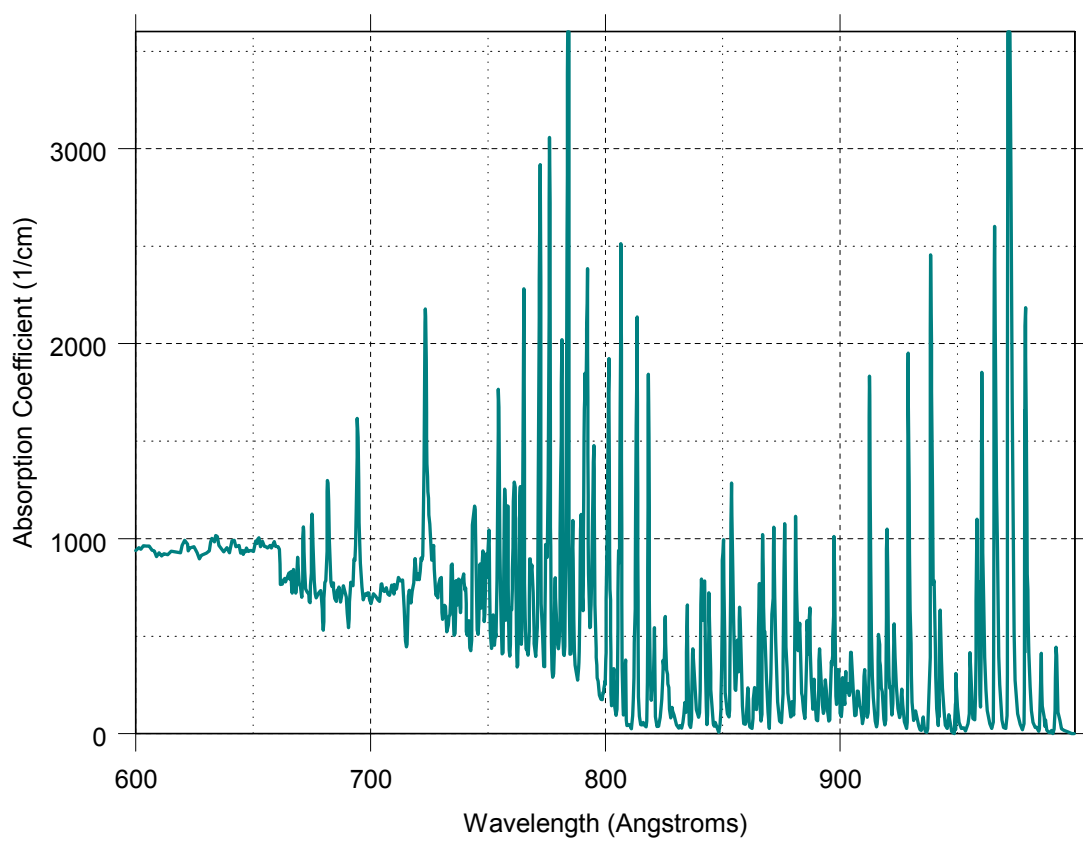
Figure 10. N_2 Absorption Coefficient Over the 600-1000 Å Range
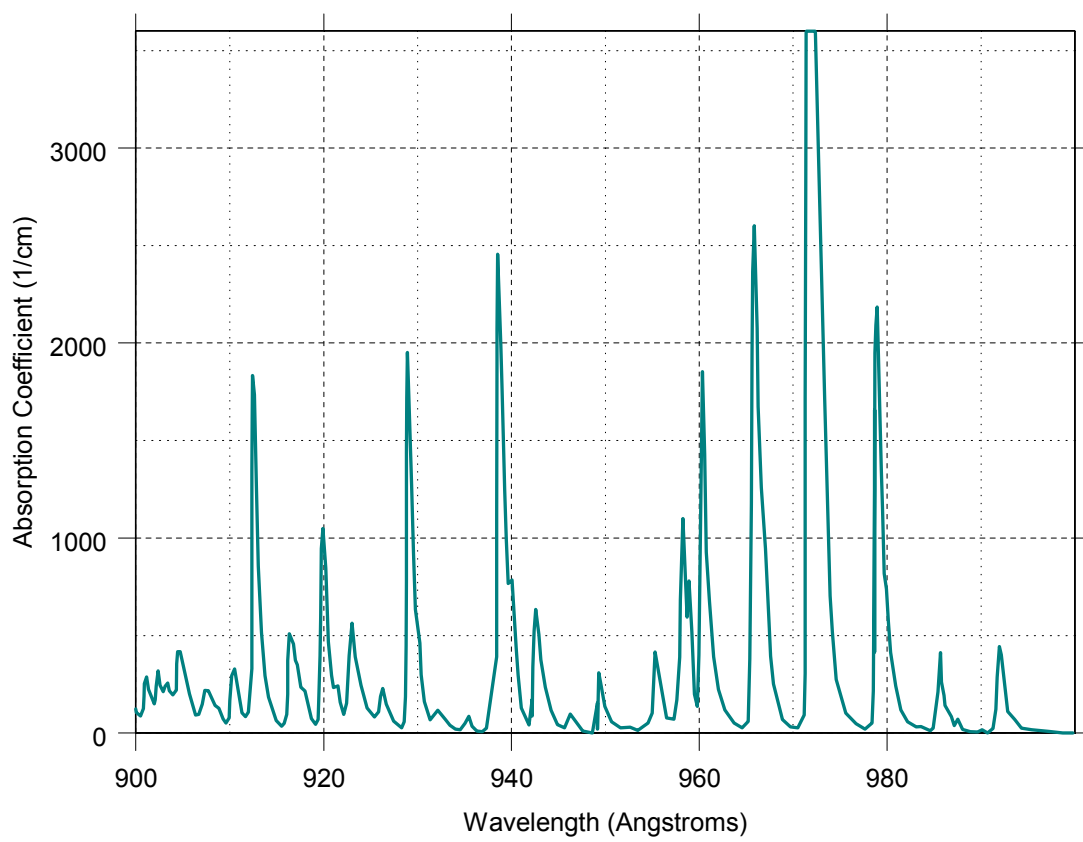
Figure 11. N$_2$ Absorption Coefficient Over the 900 - 1000 Å Range. (Detail of Figure 10)

Material	E_l (ev)	s (ev^{-1})	E_b (ev)	Q_s
Teflon	5.85	1.825×10^{-2}	37.85	0.199
Polyethylene	7.84	9.592×10^{-2}	13.67	0.176

Table 3.Polymer Photoemission Parameters

Where Q is the quantum yield, E_p is the photon energy, E_l is the lowest energy at which one can detect photoemission and E_b is the energy above which the quantum yield saturates. Q_s is the quantum yield at saturation, and s is the slope of the cube root of the quantum yield in the energy range $[E_l, E_b]$. The parameters for two materials are shown in Table 3.

Figure 12 shows experimental data from Guzhov [37] and Tom [10] plotted along with the fit function for Teflon, while Figure 13 shows experimental data from Guzhov [37] and Fujihira [8] plotted along with the fit function for polyethylene.

6   Simulation Results

We ran two sets of simulations. In the first set, which we term "bounding assumptions," we made assumptions that accentuated the photoemission process in order to ascertain if the effect was detectable in the best of circumstances. In the second set, which we term "realistic assumptions," we made more realistic assumptions to see if the effects we observed during the first set with respect to photoemission remained.

The first set of results are shown in Figures 14 through 24 and summarized in Table 4. The assumptions were that an excitational collision always resulted in the release of a single photon which had an energy equal to that of the threshold energy. No absorption was allowed as the photon traveled through the gas. Thus we maximize the energy of the photons released due to an excitation collision and thus obtain maximum yield of photoemission from the surface.

Figure 14 shows the number of photons as a function of time when the accelerating field is 8 MV/m. All of the simulations start with 1000 electrons and 1000 ions uniformly distributed in a hemisphere 1μm in radius in the gas above the dielectric and centered at the origin. All of the Figures are for Teflon except for Figure 24, which is for polyethylene. Note in Figure 14 that the 1000 initial electrons quickly drop to 200 electrons in the first 0.1 ns. This is because most of the electrons stick to the surface due to secondary electron emission. The gas pressure is 760 Torr, which means that the field applied here is approximately 2.7 times the threshold field required for breakdown (3 MV/m). Eventually the number of electrons grows exponentially in time and as they move in space $e^{\alpha x}$. For this field level $\alpha = 1.69 \times 10^4$ m^{-1}.

Figure 15 shows the number of ionizing and exciting collisions as a function of time. At this field level, for each ionizing collision there are approximately 100 exciting collisions, but each ionizing collision produces a new electron, while only a small fraction of exciting collisions produce a new electron through the photoemission process. Figure 16 demonstrates this by plotting the cumulative number of electrons added to the problem space due to three processes: collisional ionization, photoionization and photoemission as a function of time. At this field level the electrons added due to collisional ionization is much greater than the electrons added by both photoionization and photoemission processes. Further, photoionization adds more electrons than photoemission.

Figure 17 shows the cumulative number of electrons in the problem space lost to the surface due to secondary electron emission, which in this energy regime takes electrons out of the problem space, and photoemission, which adds electrons to the problem space. This figure shows that the net effect of the surface is to take electrons from the problem space and inhibit the growth of the number of electrons.
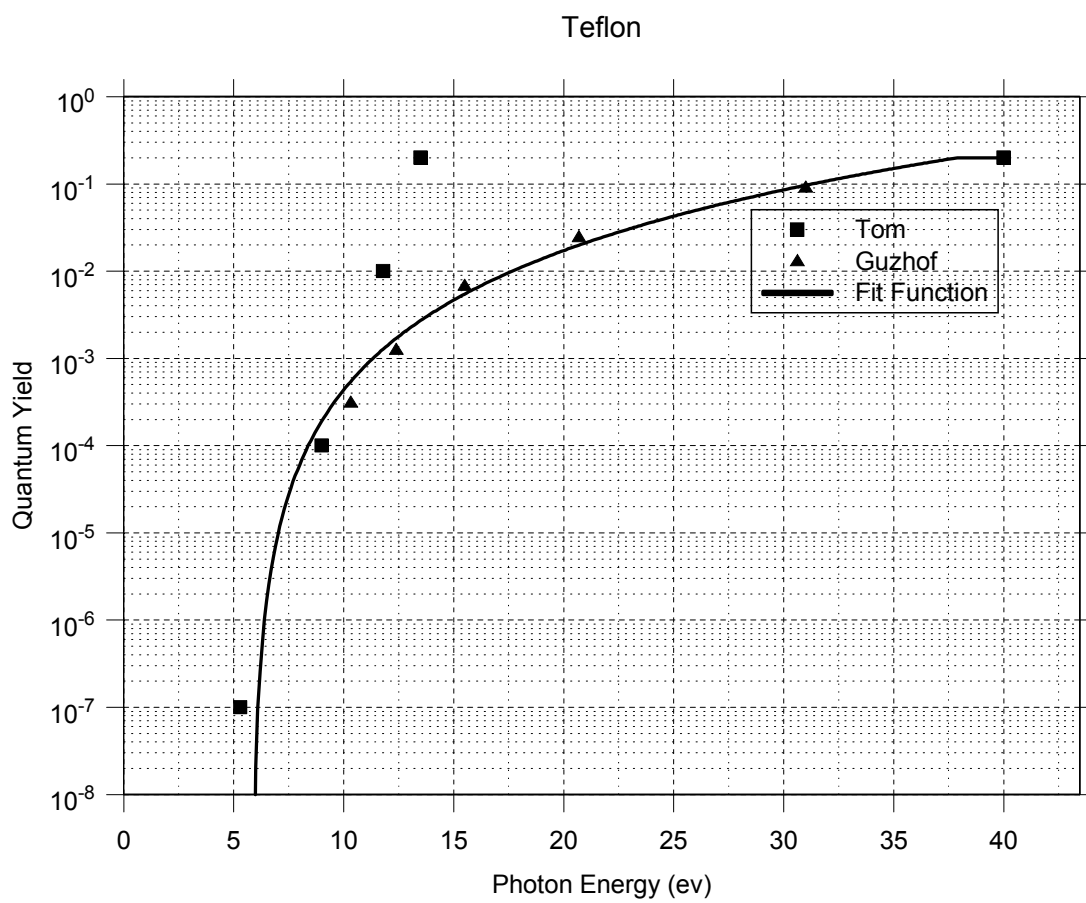
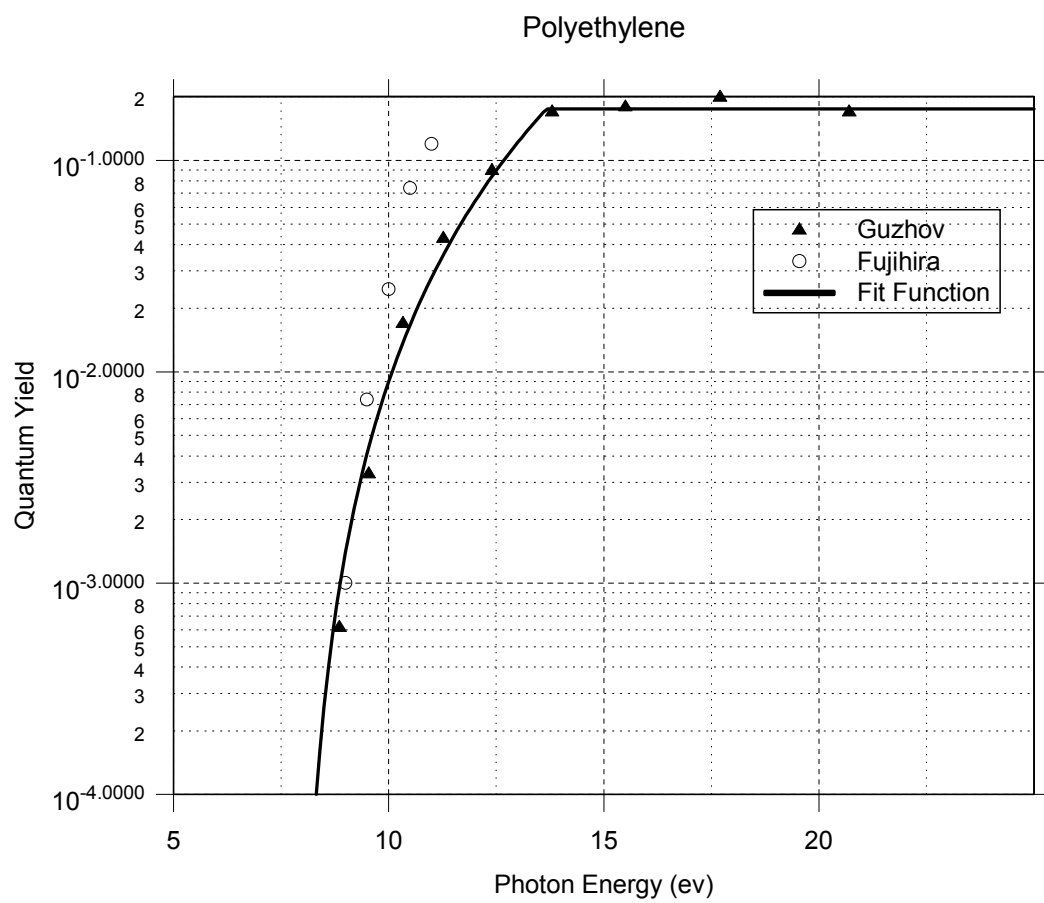Figure 12. Photoemission from Teflon

Figure 13. Photoemission from Polyethylene

Nitrogen at 760 Torr
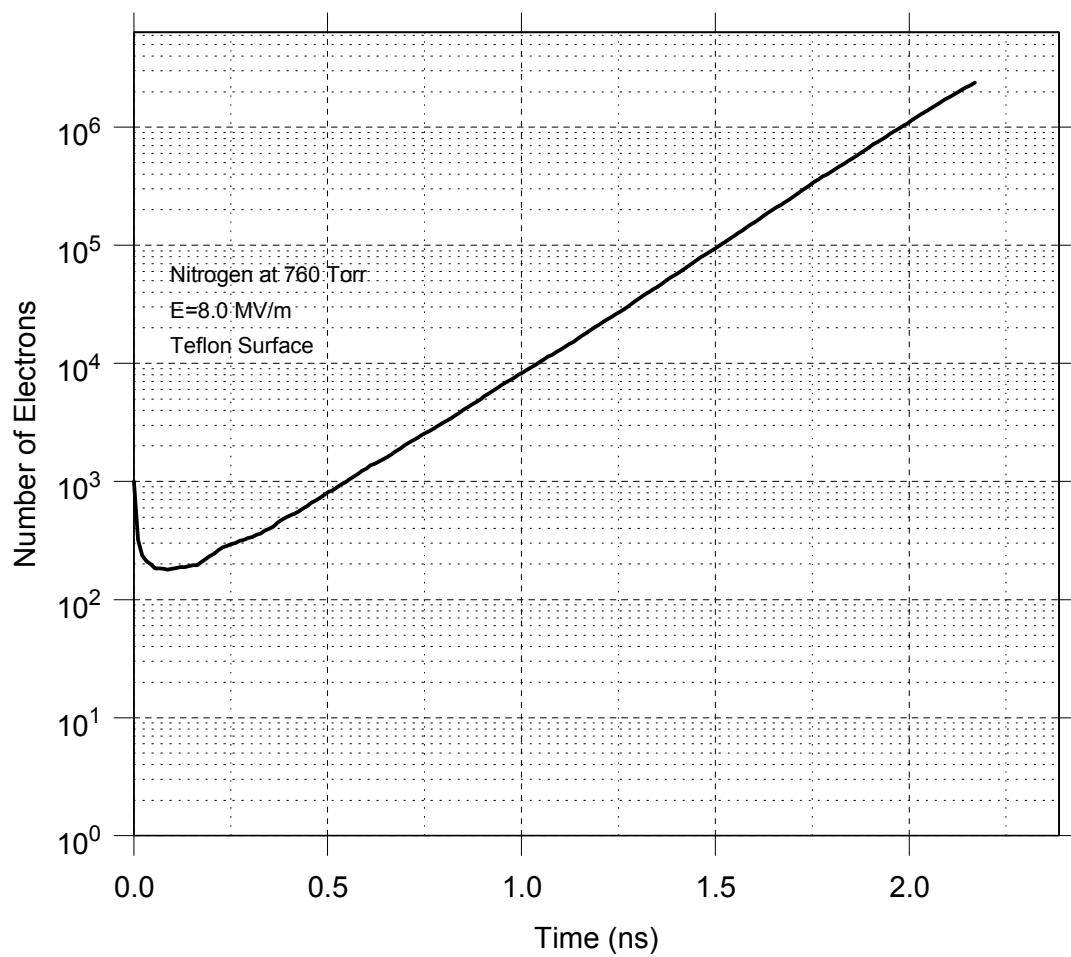E=8.0 MV/m
Teflon Surface

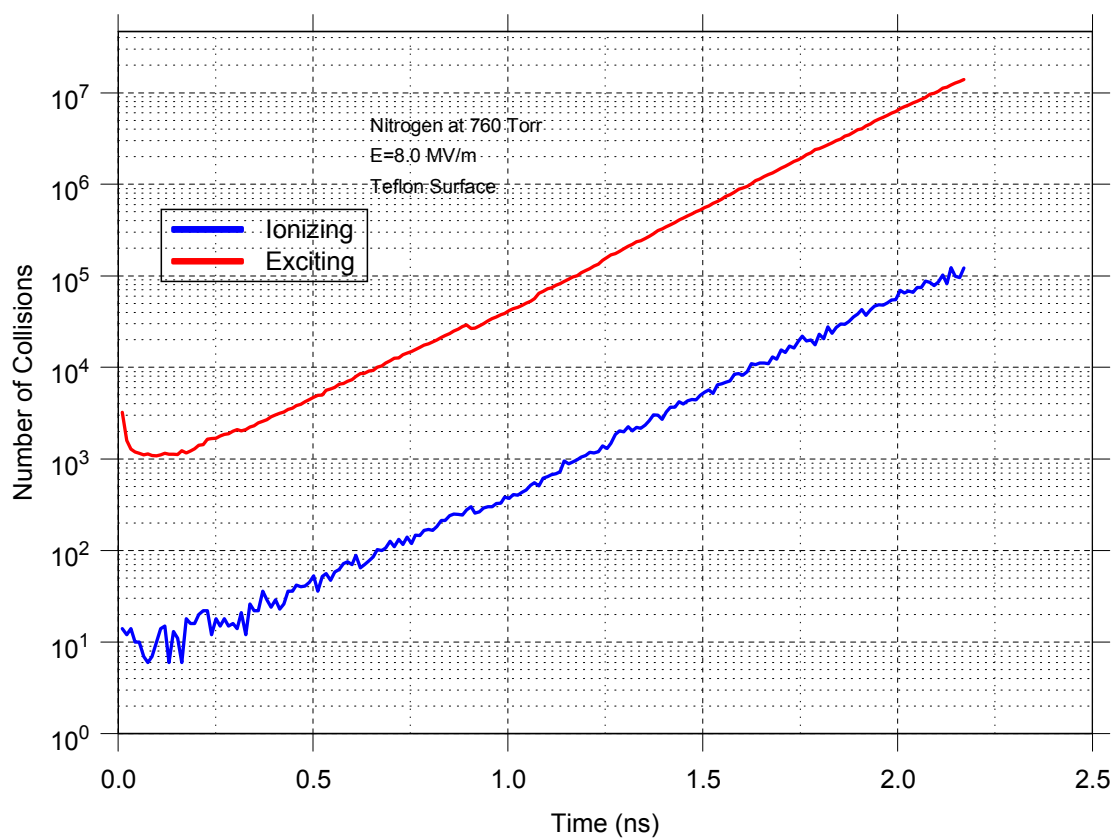Figure 14. Number of Electrons versus Time

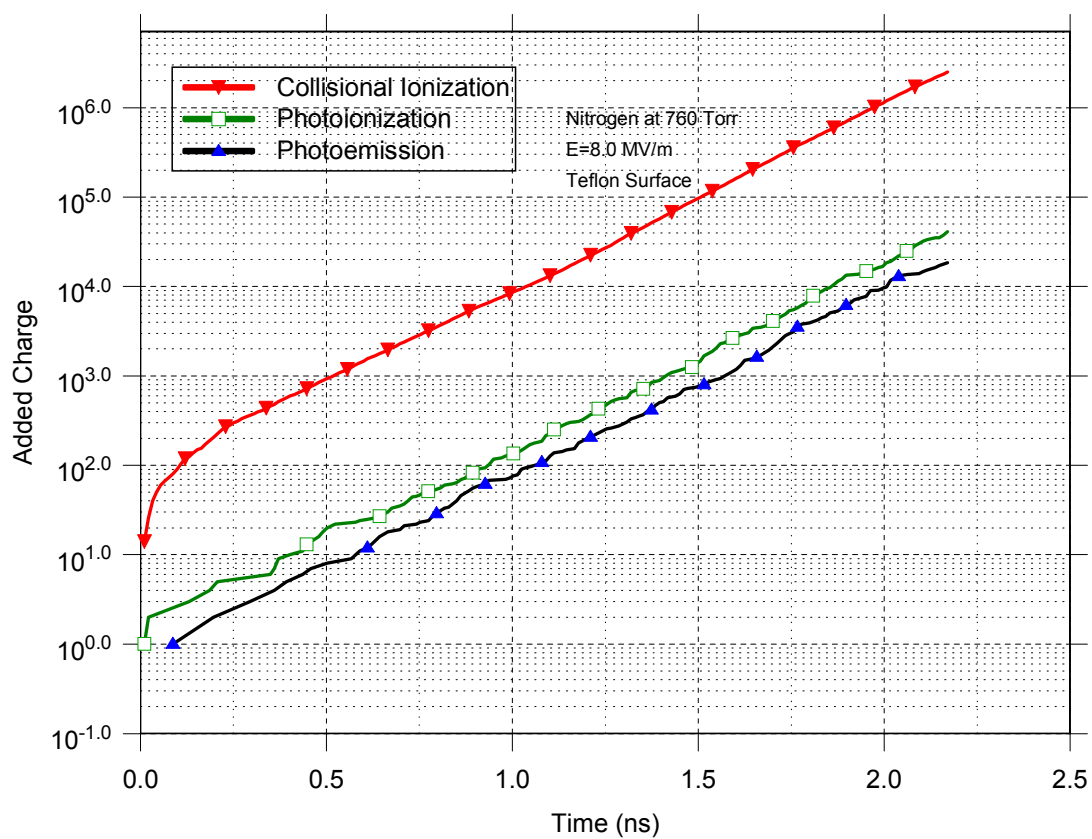Figure 15. Number of Ionizing and Exciting Collisions versus Time

Figure 16. Electrons Added to the Avalanche Due to Three Processes versus Time
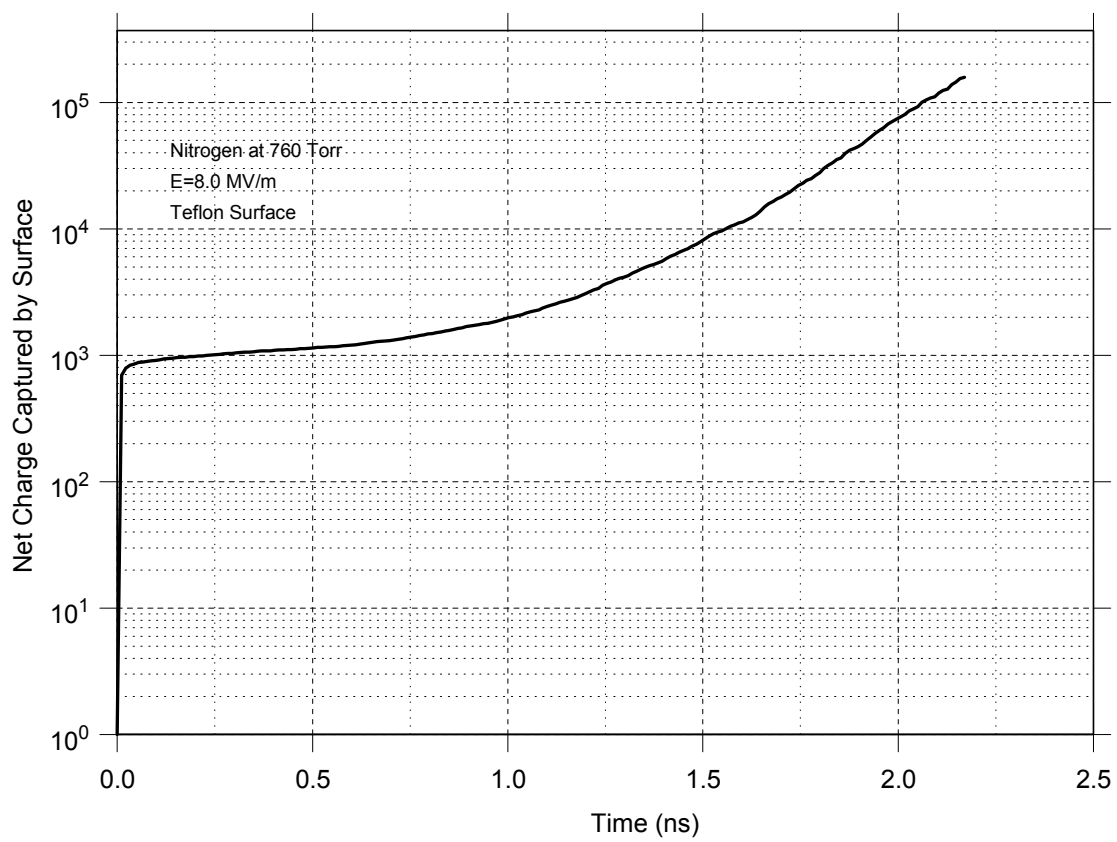
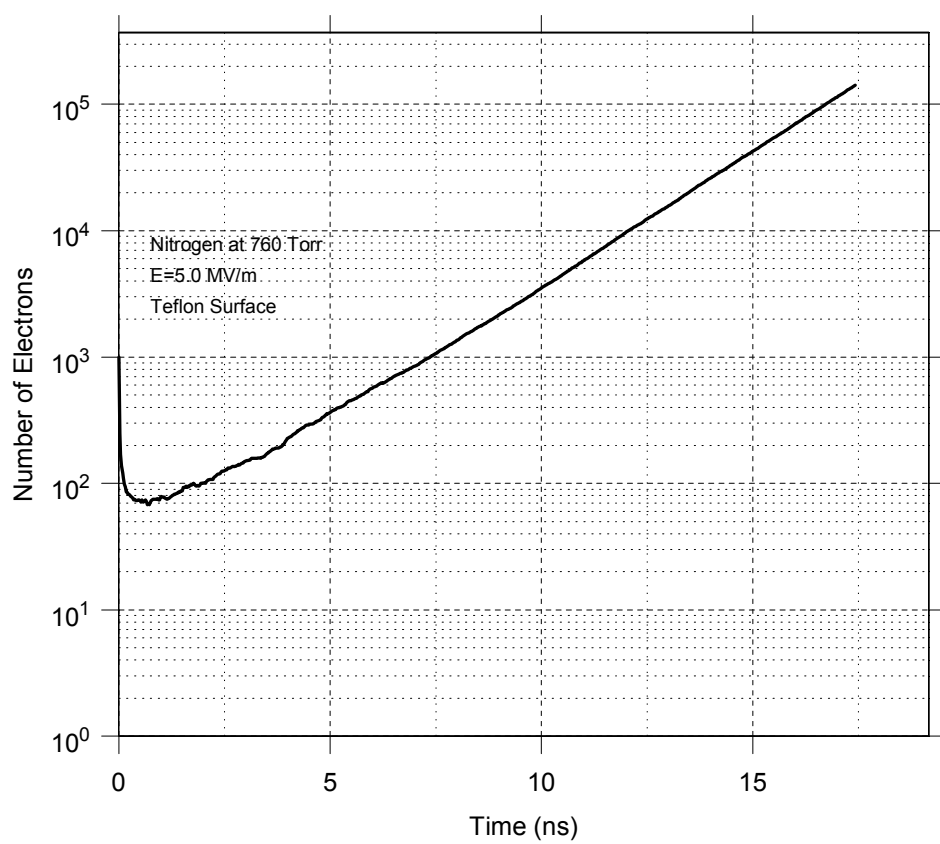Figure 17. Accumulated Electrons Lost to the Surface versus Time

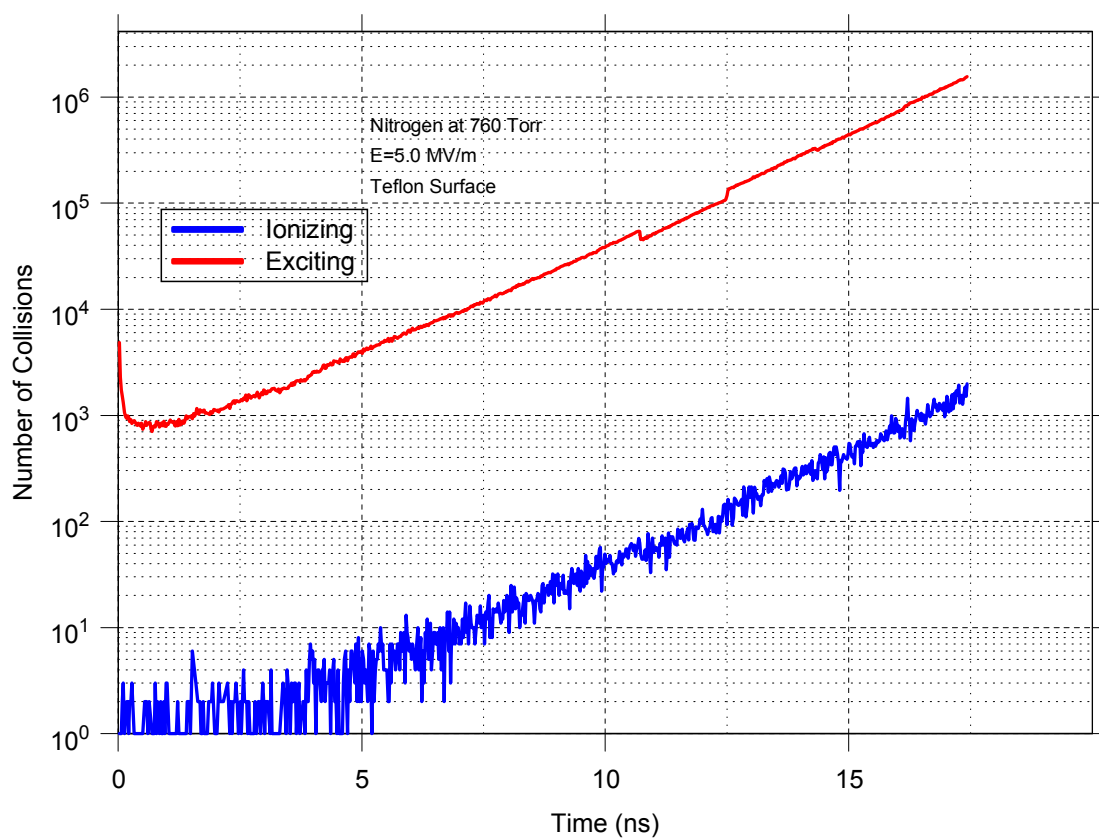Figure 18. Number of Electrons versus Time

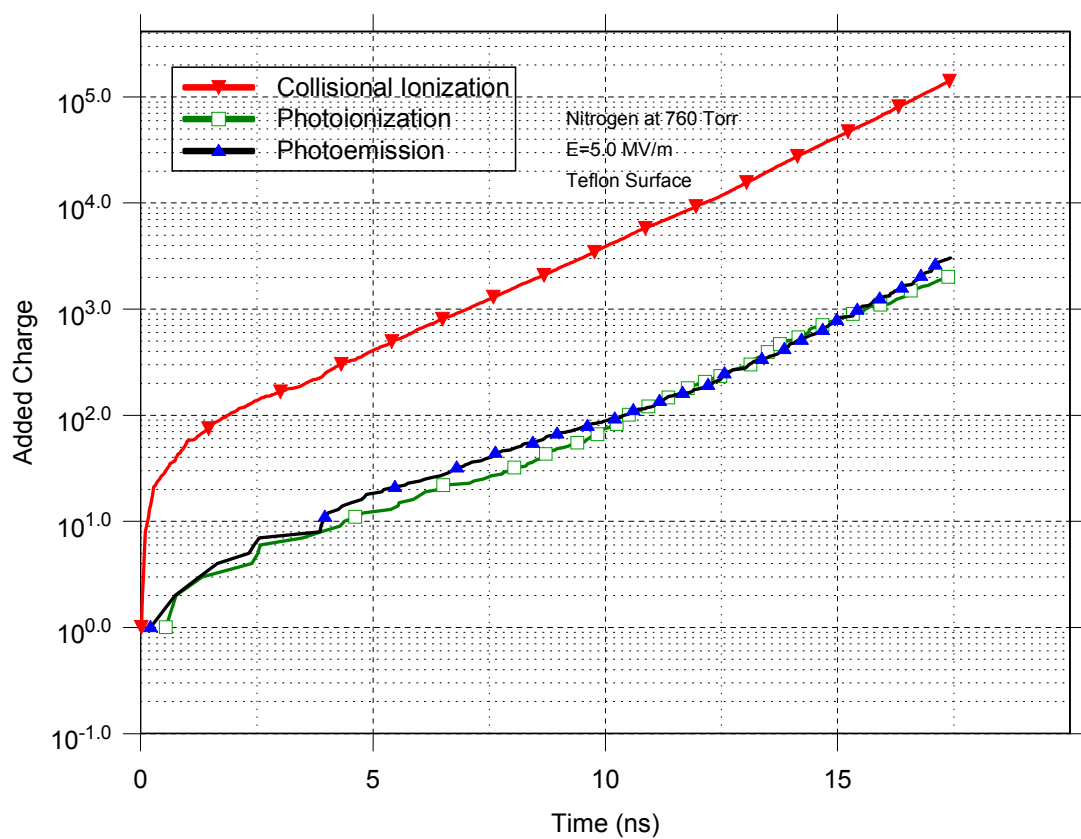Figure 19. Number of Exciting and Ionizing Collisions versus Time

Figure 20. Electrons Added to the Avalanche Due to Three Processes versus Time
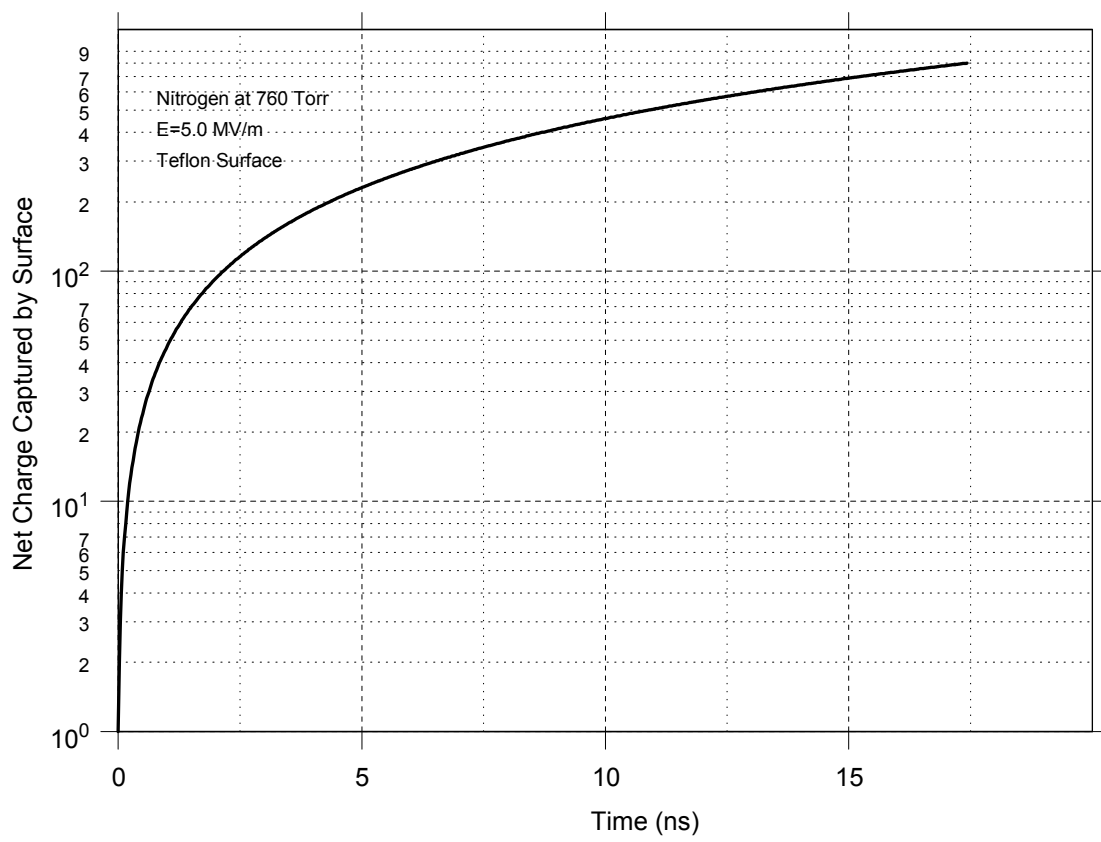
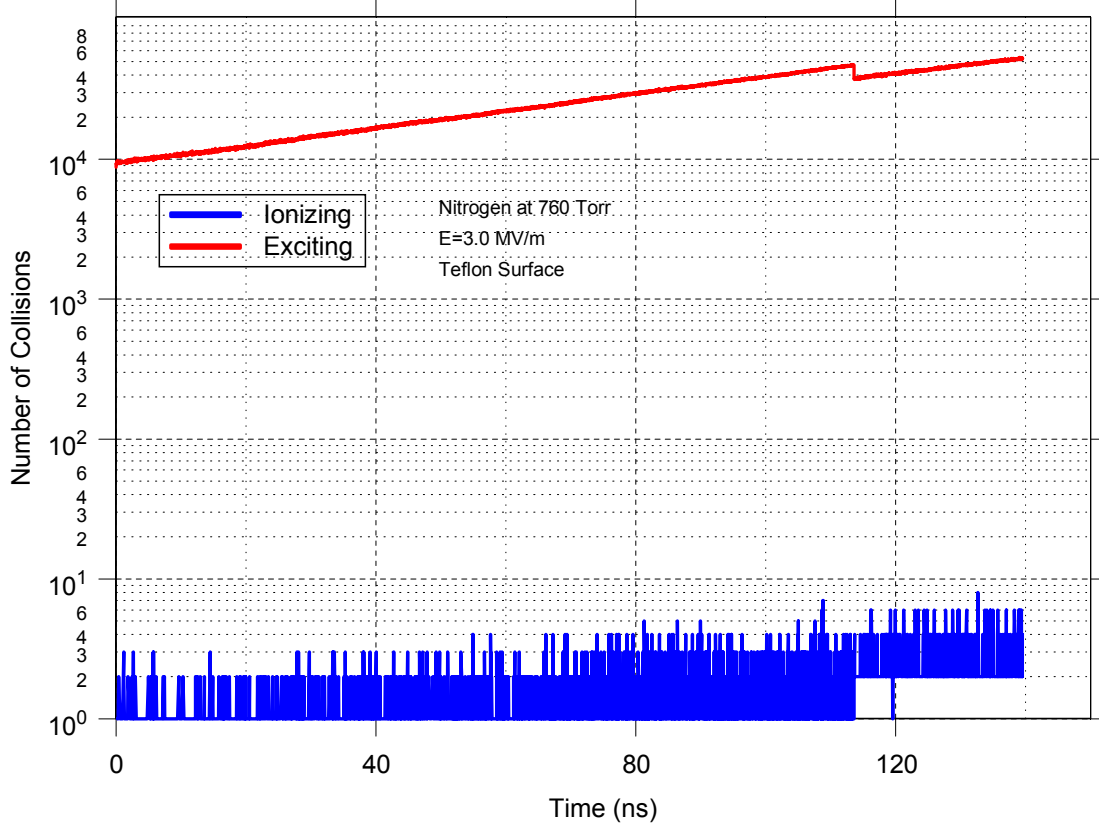Figure 21. Accumulated Electrons Lost to the Surface versus Time

Figure 22. Number of Exciting and Ionizing Collisions versus Time

Figures 18-21 shows the same information as Figures 14-17 except that the field is now 5 MV/m. The electron growth rate has slowed, $\alpha = 2.8 \times 10^3$ m^{-1}. There are roughly 1000 times as many exciting collisions as ionizing collisions (Figure 19). The electrons added due to photoemission is comparable to the electrons added due to photoionization. Electrons added due to collisions still dominate (Figure 20). Again, there is a net loss of electrons due to the surface (Figure 21).

Finally, we reduce the field to 3 MV/m (breakdown threshold). In order to measure the growth of electrons in a reasonable length of compute time, we eliminated the effect of secondary electron emission and therefore, eliminated the electron sink. Figure 22 shows that there are now 10,000 times as many exciting collisions as ionizing collisions. Figure 23 shows that at this field level the photoemission is now bigger than the photoionization although the collision ionization still dominates. This changes in Figure 24, where the surface is now polyethylene. Here the photoemission is bigger than both photoionization and collision processes.

These results as well as results for other field levels are summarized in Table 4. Column one is the dielectric material. Column two is the drive field. Since we ran the simulations for different times, we normalized the results by the number of electrons due to collision processes. Column three is the number of electrons created by photoemission processes divided by the number of collision electrons. Column four
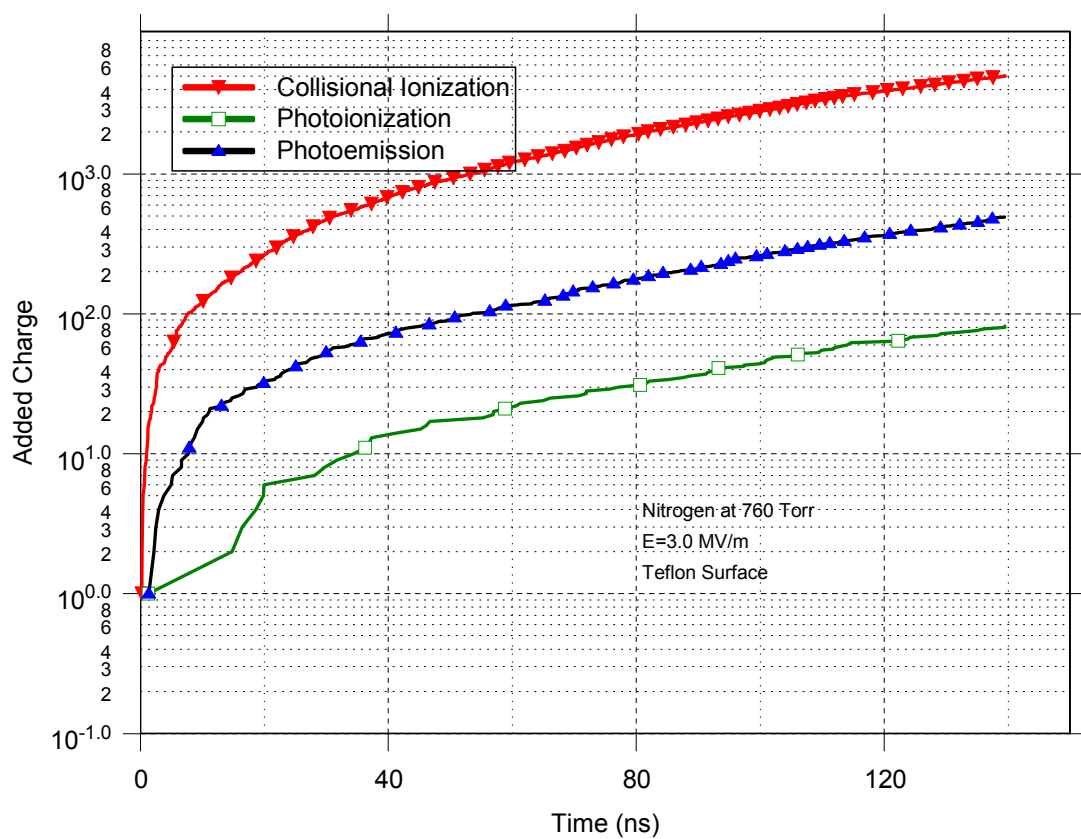
44

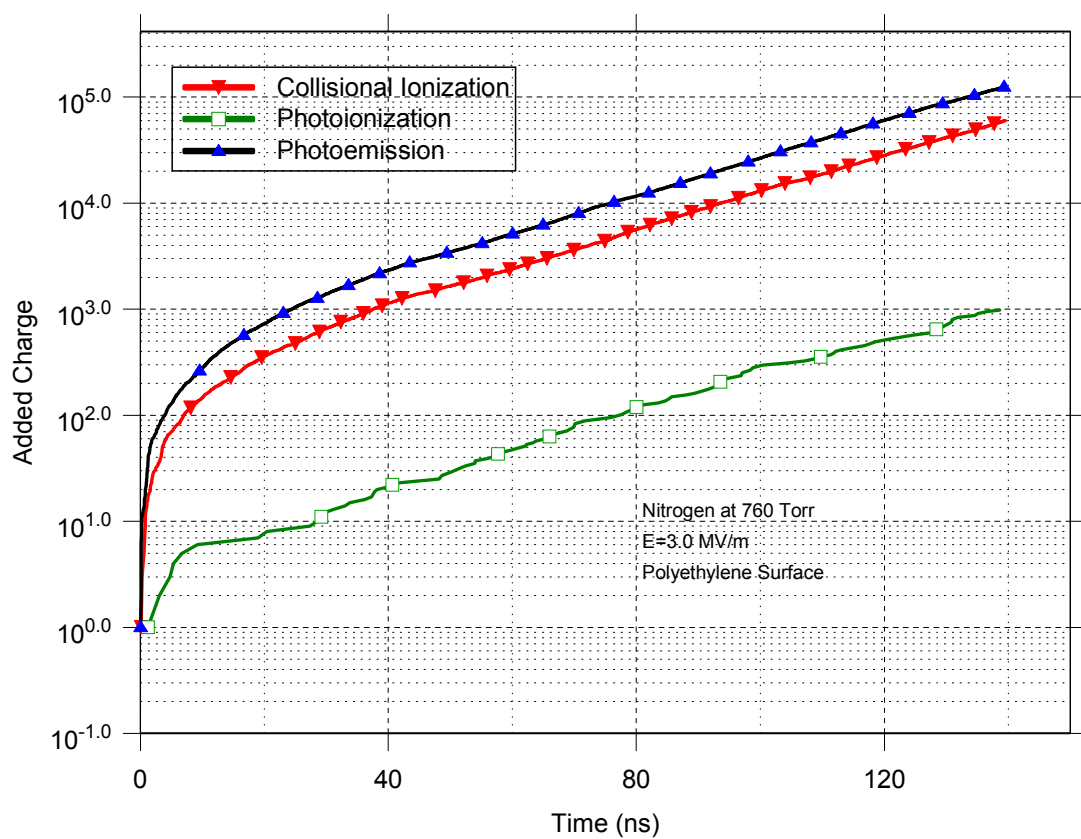Figure 23. Electrons Added to the Avalanche Due to Three Processes versus Time

Figure 24. Electrons Added to the Avalanche Due to Three Processes versus Time

Material	Field (MV/m)	PE/Coll (%)	PI/Coll (%)	Net Surface/Coll (%)	α (m^{-1})
Teflon	8	0.741	1.63	-6.33	1.69×10^4
Teflon	6	1.25	1.82	-6.70	6.55×10^3
Teflon	5	2.13	1.42	-6.76	2.80×10^3
Teflon	4	3.71	1.99	-4.87	796
Teflon	3	9.83	1.63	SEE turned off	130
Polyethylene	8	32.6	1.73	-3.60	1.98×10^4
Polyethylene	6	45.6	1.86	-5.95	7.40×10^3
Polyethylene	5	63.0	2.06	-6.57	3.22×10^3
Polyethylene	4	97.4	1.94	-8.86	845.
Polyethylene	3	207.	1.60	SEE turned off	332.

Table 4.Results with Bounding Assumptions

is the number of electrons created by photoionization divided by the number of collision electrons. Column five is the net electrons supplied by the surface (photoemission and secondary electron emission) divided by the collision electrons. Finally, column six is the exponential growth parameter α.

Note that for all materials and fields, the photoionization remains relatively constant at approximately 2%. Photoemission increases relative to the collision ionization as the field decreases. Polyethylene, for example, shows more photoemission than collision ionization at 3 MV/m by a factor of 2. Secondary electron emission causes the dielectric to act as a sink as shown by the negative numbers in the fifth column. Because it has more photoemission activity, polyethylene has a slightly larger value of α than Teflon for all values of field.

Table 5 shows the same information as Table 4 except that the realistic assumptions are in place. The photons released due to a collision have an energy in accordance with known spectral bands as described in Section 5.3.1. Absorption of the photon as it travels through the gas is in accordance with Figure 10. Although the absolute percentages of columns 3 and 5 have changed from Table 4, the trends are the same.

7 Breakdown Experiments

Experiments in breakdown across an insulating surface at atmospheric pressure were conducted at Texas Tech University. The goal was to study the combined role of elementary processes involving the surface (such as secondary electron emission, photoemission, gas desorption, and so forth) prior to breakdown and by varying the experimental conditions, indirectly obtain information on the surface processes. The experiments and results are discussed in the following sections.

7.1 Setup

It is well known that the dynamics of surface flashover require a temporal resolution in the nanosecond time regime. Hence, the test apparatus has to be carefully designed to ensure that the shape of the transient signals is due to the flashover itself and is not distorted by the external electrical circuit. This high temporal resolution has been achieved by designing a surface flashover chamber that exhibits coaxial geometry with an impedance of 52 Ω everywhere in the system between the two connections of the dual, high-voltage power supply and the two coaxial cables extending to the left and right in Figure 25. Any transient signal launched in the system from the flashover gap will be reflected at the power supply connections back toward the gap. Since the coaxial cables are about 65 ns in electrical length, we observe the reflected current with our current sensors, which are located close to the gap, after about 130 ns.

Material	Field (MV/m)	PE/Coll (%)	PI/Coll (%)	Net Surface/Coll (%)	α
Teflon	8	0.34	1.78	-5.47	1.76×10^4
Teflon	5	1.17	1.58	-7.80	2.78×10^3
Teflon	3	8.64	1.33	SEE turned off	126.
Polyethylene	8	10.9	1.52	-5.86	2.00×10^4
Polyethylene	5	28.3	1.84	-7.29	2.81×10^3
Polyethylene	3	163.	1.72	SEE turned off	297.

<div align="center">Table 5.Results with Realistic Assumptions</div>

The current sensors have a sensitivity of 0.1 V/A or 0.2 V/A, as indicated in Figure 25. To achieve a better resolution, some of the sensor signals are amplified by 30 dB before being fed into the high-speed oscilloscope. A trigger-delay generator provides timing to the intensified cameras so that the camera gate can be positioned with respect to the current waveform as needed. Most experiments were performed with an 80 ns electrical gate, which results in a 68 ns optical gate for the cameras.

The surface flashover chamber features gas-tight feed-throughs that conserve the impedance of 52 Ω as the transition from small inner conductor to larger inner conductor inside the chamber is made (see Figure 26). We utilized nylon screws to press the sample firmly to the electrodes since it is known that an air gap between the electrodes and dielectric has a major influence on the hold-off voltage.

Most tests were done using the standard electrode geometry shown in Figure 26, which exhibits a weak electric field component normal to the dielectric surface. Some tests, however, (mainly for side-on imaging of the flashover) were conducted using the modified electrode geometry shown in Figure 27, which exhibits a large electric field component normal to the dielectric surface.

Without the presence of the dielectric sample, the discharge is known to preferentially follow the electric field lines. It is unknown what effect the dielectric surface will have on the discharge path as this has not yet been studied in detail. For electrodes buried in Lexan, the electric field lines are shown in Figure 28. The magnitude of the electric field is depicted in Figures 29 and 30, showing the side-on and top view, respectively. All field simulations were carried out using Maxwell Ansoft 3D-field simulator software.

Since camera imaging of the discharge provides just a single picture of the developing discharge, an approach utilizing fiber-optics was chosen to spatially resolve light emission from the discharge gap, see Figure 31. The fiber output was connected either to a spectrograph, capturing spectra in the range from 180 nm to 800 nm, or to a photo multiplier tube (PMT), one for each channel. At present, up to 3 channels, gathering light from the anode, cathode, and center of gap region have been used. All electrodes were fabricated from brass; Lexan was the only dielectric material that was tested.

7.2 Procedure

Most of the components used in the experiment remained the same from setup to setup, with only some minor modifications. These components include the oscilloscopes used to collect data from the current and voltage sensors as well as from the PMT's. In addition, two high-speed, high-sensitivity cameras were used to capture the pre- and main breakdowns as well as the spectra produced by the spectrograph. The scopes used were two Agilent Infiniium 500MHz, 2GSa/s Digital Oscilloscopes with network capabilities, and the cameras were two ICCD Oriel InstaSpec V cameras, with TTL gated shutters capable of an exposure time of down to 2.5 ns. The cameras are controlled by two on-site computers and a gate pulse generator. The gate pulse generator is triggered by the output of one of the current sensors, to provide a gate to the camera when the pre or main breakdown occurs. The gate pulse trigger is designed to output an 80ns gate to the camera upon detecting a rising edge as low as 5mV at the input. After the initial gate, the trigger
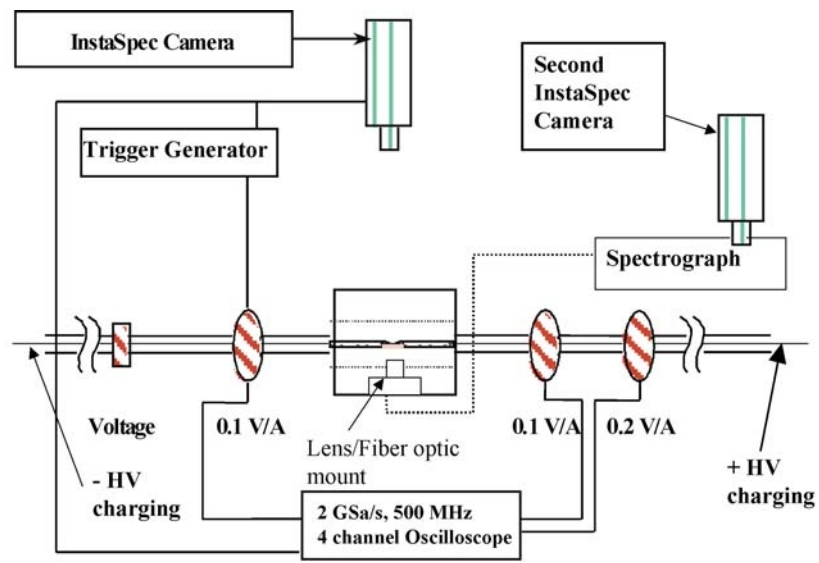
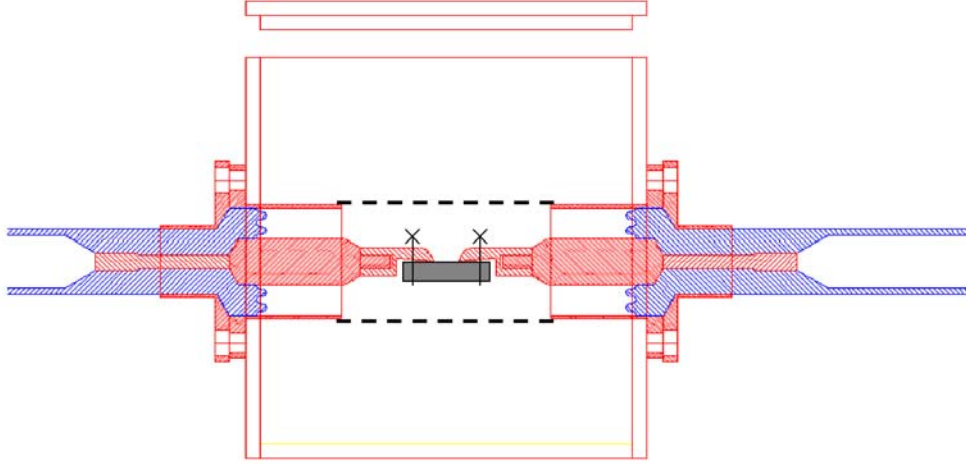Figure 25. Schematic of Experimental Setup for Surface Flashover Experiments at Atmospheric Pressure

Figure 26. Cross-Section of Test Chamber with Standard Electrode Geometry

must be reset manually after each test. This prevents any retriggering during a single test. For very small pre-breakdowns an amplifier is added between the current sensor and the trigger generator. To capture just the main breakdowns an attenuator is placed between the current sensor and the trigger generator. The chamber itself remained unchanged from setup to setup as well. It is about eight inches cubed and is made of half inch thick, clear Lexan. It has an input and relief port for filling the chamber with various gases, as well as fiber-optic feed-throughs to accommodate the cables leading to the PMT's and the spectrograph. A close-up of the chamber region of the experiment is shown in Figure 32.

The testing procedure varied only slightly from one experimental setup to another. When capturing a picture of breakdown along the surface the camera was fitted with a zoom lens that was also used for focusing purposes. The camera was set up just outside the chamber and aimed at the electrodes and the surface through a small hole in the outer conductor. First a reference shot was taken to check for focus and to help identify the sample and the electrodes in later shots. For capturing PMT or spectroscopy signals, a special, fiber-optic lens holder was placed inside the chamber, just above the sample inside the outer conductor. There are three lenses, one focusing light from the anode, one from the cathode, and one from the middle of the sample. Each lens focuses its light into a different fiber-optic cable that is then run through the small hole in the outer conductor and connected to one of the feed-throughs on the side of the chamber. Depending on which experiment is to be run, the other side of the feed-throughs are connected to either the fiber-optic cables leading to the PMT's or the cables leading to the spectroscope. The chamber was then filled with the appropriate gas for the particular experiment – air, nitrogen or otherwise. Once the camera – either with the zoom lens or on the spectrograph scope or scopes if the PMT's are being used – and gate pulse trigger are all armed, i.e. recording, the main power supply is slowly turned up until the breakdown occurs. The captured waveforms and images are then saved and the trigger is reset for the next run. It should be noted that all surface flashover experiments were carried out by slowly raising the applied gap voltage $\approx$ 2 kV/s, until breakdown occurred.

7.3   Results

7.3.1 Side-on Imaging for Modified Electrode Geometry with Groove in Dielectric Surface

The results shown in this section are of breakdowns and pre-breakdowns across the modified electrode geometry (Figure 27) with a grooved dielectric surface both in air and in nitrogen. The groove is shown

Figure 27. Modified Electrode Geometry Generating a Large Electric Field Component Normal to the Dielectric Surface
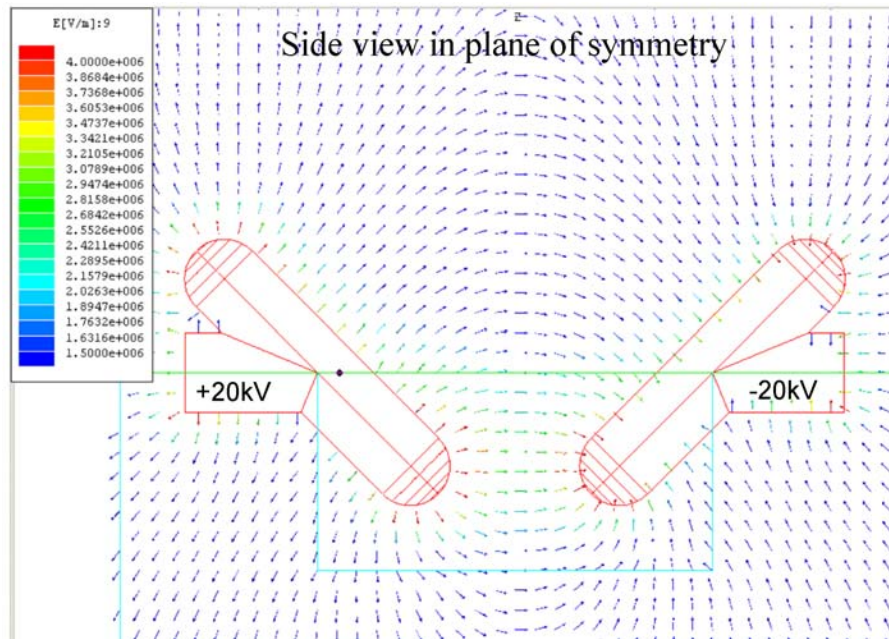

Figure 28. Electric Field (V/m) in the Plane of Symmetry of the Electrodes (Side View)
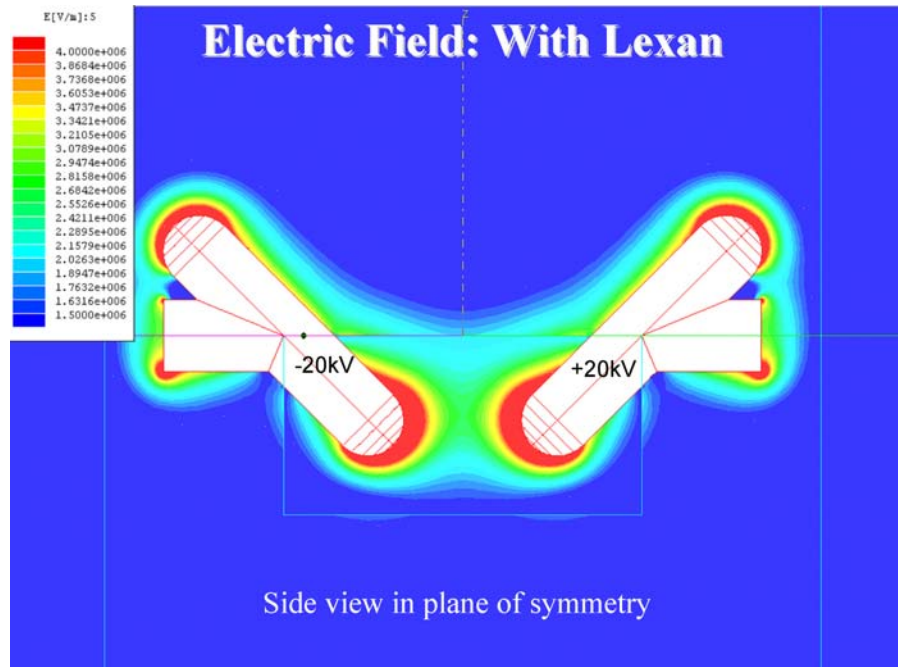
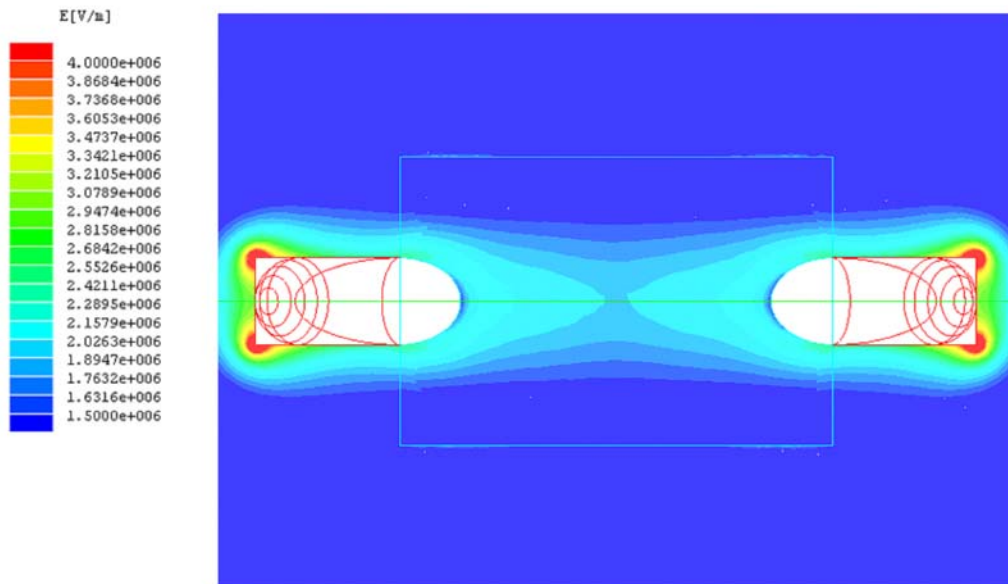Figure 29. Electric Field Magnitude (V/m) in the Plane of Symmetry of the Electrodes (Side View)

Figure 30. Electric Field Magnitude (V/m) in the Plane of the Lexan Surface (Top View)
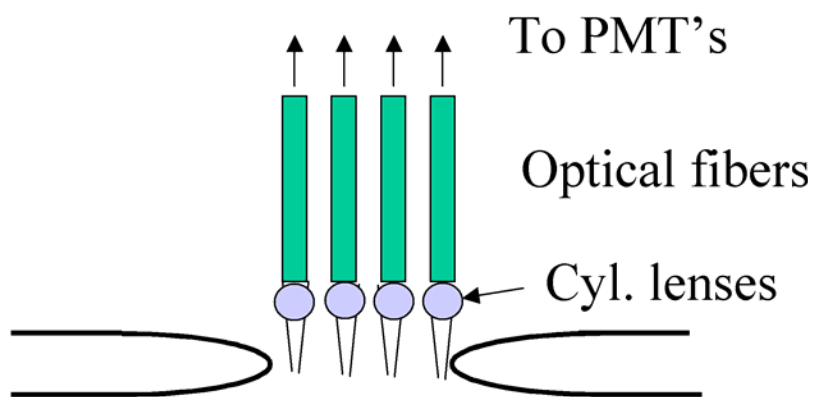
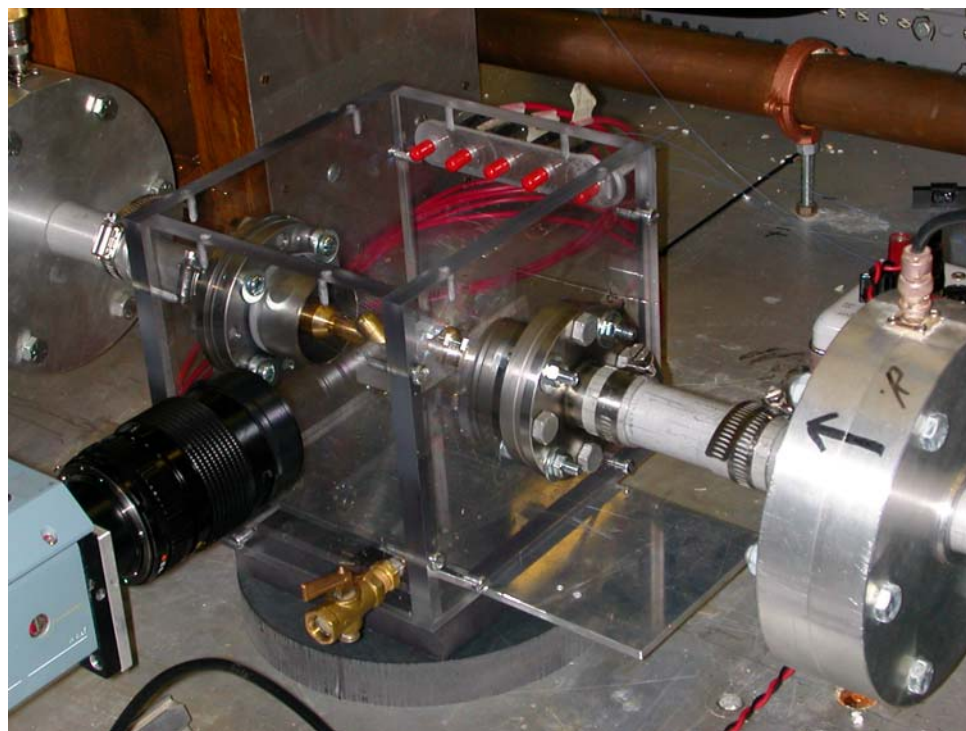Figure 31. Fiber-optics for Spatially Resolving Light Emission in the Gap

Figure 32. Experimental Setup Showing Camera, Electrodes and Gas Chamber
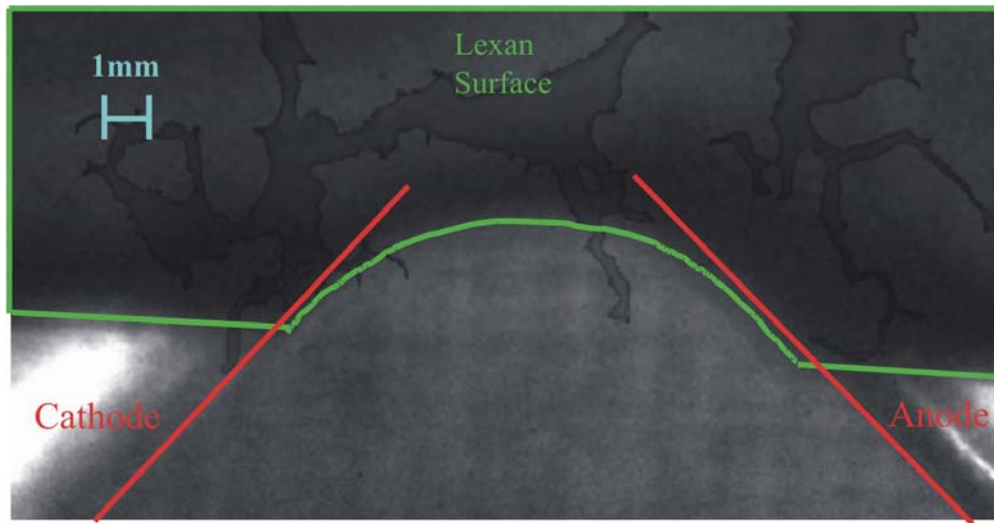
Figure 33. Side-on Reference Image with Groove, 12 mm Gap. Image Rotated 180^0 with Respect to Figure 29.

outlined in green in Figure 33. In the direction perpendicular to the plane of the paper the groove was cut wide enough so that it is essentially infinite in extent. The electrodes are outlined in red. The patterns in the upper part of the image are due to camera blemishes. Note that the image is rotated so that the gas is at the bottom of the figure and Lexan is at the top. This orientation will be used for all the side-on images in this report.

In air, the spark would follow the surface even though it was a shorter distance straight across from one electrode to the other. In nitrogen, the spark followed the electric field line from one electrode to the other. In both cases the pre-breakdowns followed the same path as the main breakdown. The only exception was in air, where the surface would become conditioned and the spark would cease to follow the surface, but would go straight from one electrode to the other.

All current traces depicted in Figures 35-37 result from the same, main breakdown event that is depicted in Figure 34. The signals are corrected for cable delay times and are accurate to within about 1 ns. Hence, although it appears as if the high sensitivity current (Figure 37) rises about 40 ns before the low sensitivity current (Figure 35), the small current amplitude remains just unresolved in the low sensitivity settings. A pre-breakdown event in air is captured in Figures 38-41. As previously mentioned, the breakdown in pure N_2 typically follows the electric field rather than the surface, as shown in Figures 42-45, which are results of a main breakdown event.
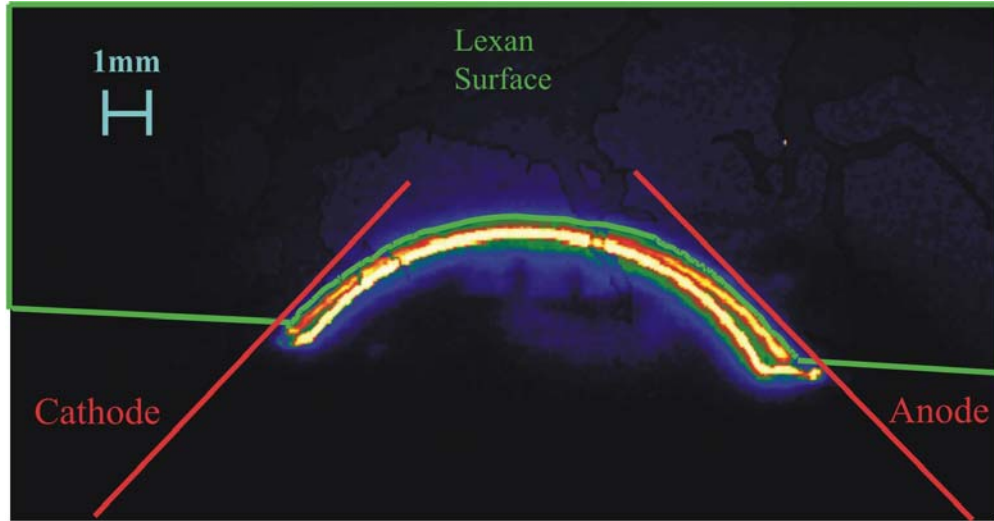
Figure 34. Side-on Image of Main Breakdown in Air with Groove, 12mm Gap. Breakdown Voltage, $V_b = 25$ kV.
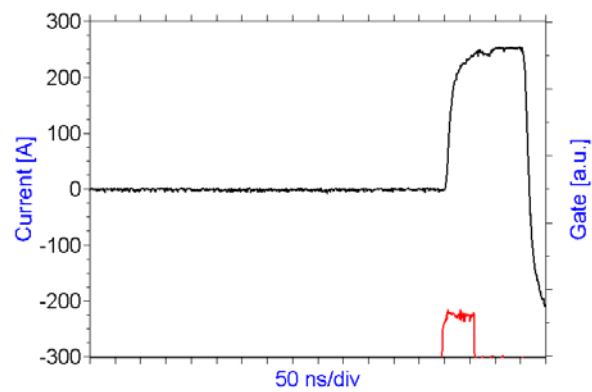

Figure 35. Discharge Current versus Time for Flashover Event Depicted in Figure 34. Sensor Set on Low Sensitivity. Red Trace Shows Camera Gate.
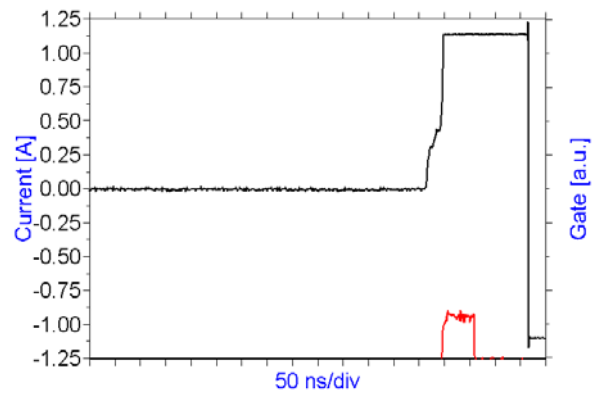
Figure 36. Same as Figure 35 but with Medium Sensitivity. Current Peak is Clipped. Sharp Drop in Current Near the End of the Graph is due to Reflected Current.
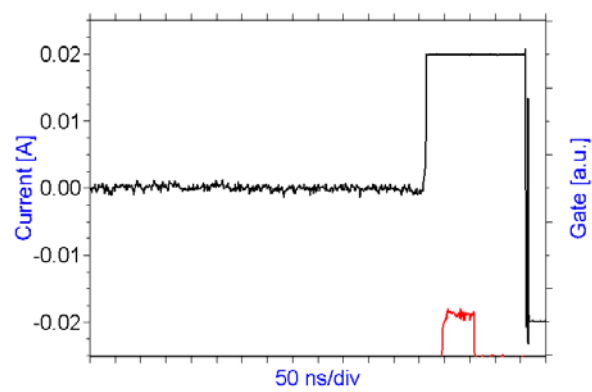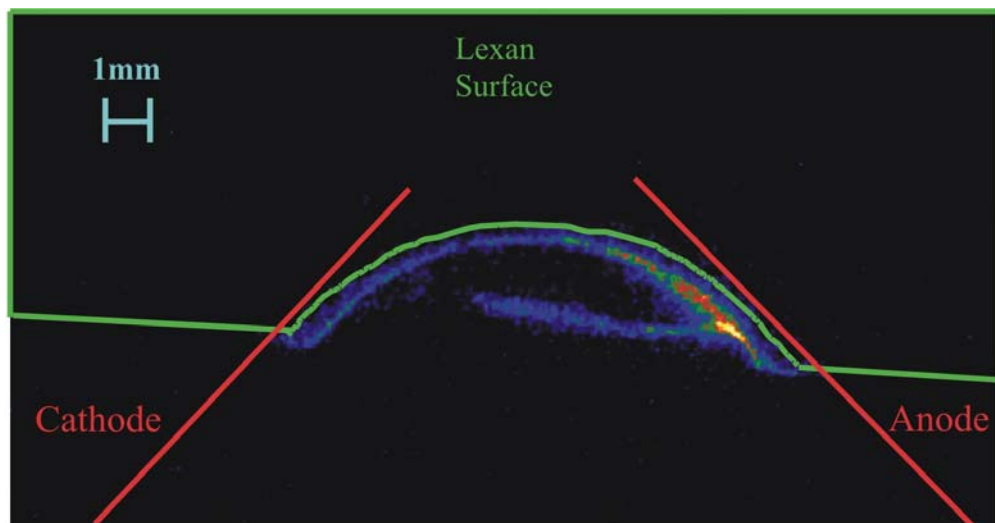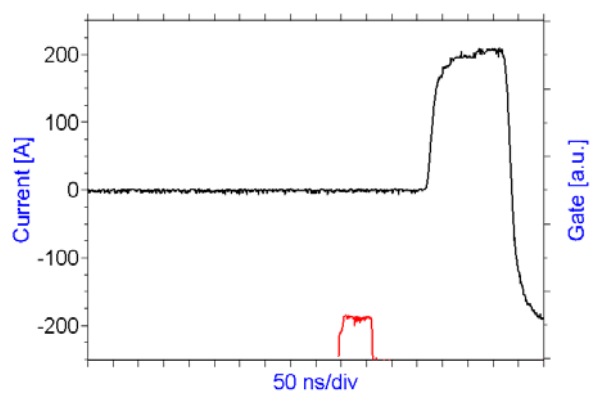

Figure 37. Same as Figure 35 but for High Sensitivity

Figure 38. Side-on Image of Pre-breakdown Pulse in Air with Groove, 12 mm Gap. Breakdown Voltage $V_b = 20$ kV.

Figure 39. Discharge Current versus Time for Flashover Event depicted in Figure 38. Sensor Set on Low Sensitivity. Red Trace shows Camera Gate. Note the Image is Taken 100 ns Prior to the Main Breakdown.
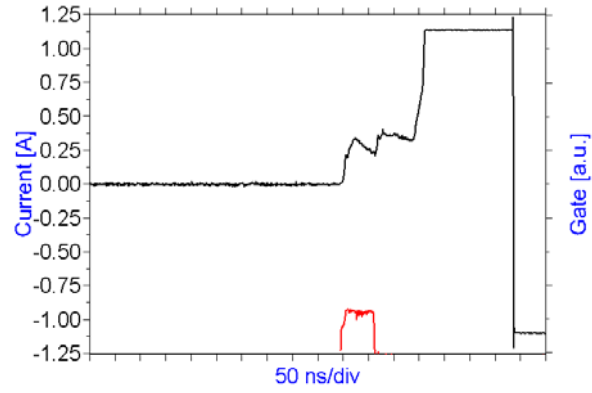
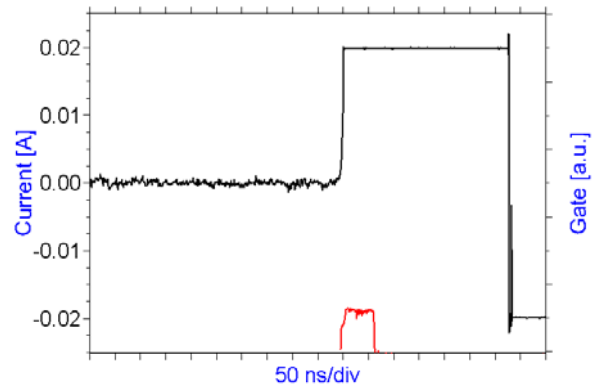Figure 40. Same as Figure 39 but with Medium Sensitivity. Current Peak is Clipped.

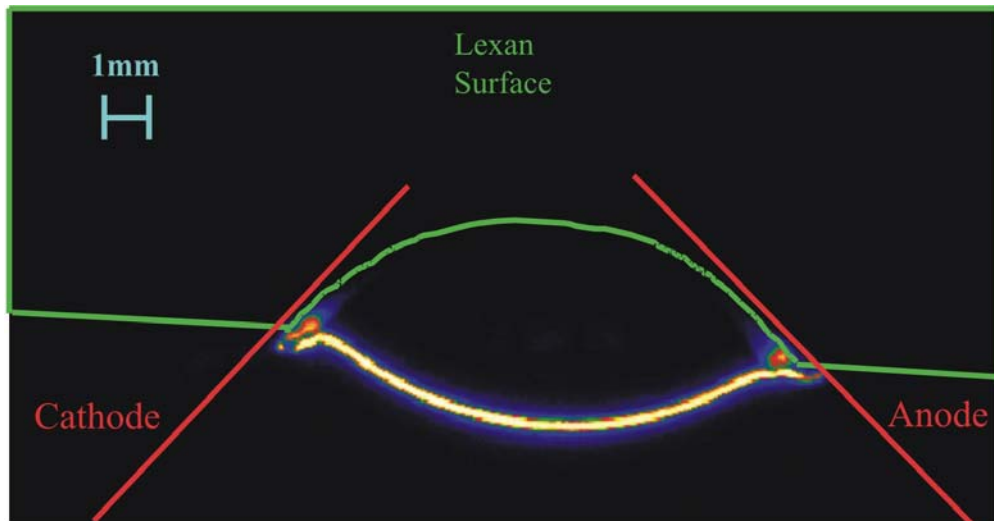Figure 41. Same as Figure 39 but with High Sensitivity. Current Peak is Clipped.

Figure 42. Side-on Image of Main Breakdown in N_2 with Groove, 12 mm Gap. Breakdown Voltage $V_b = 23.8$ kV.
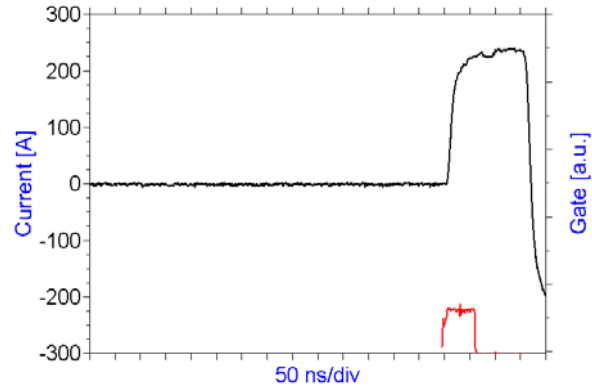
Figure 43. Discharge Current versus Time for Flashover Event Depicted in Figure 42. Sensor Set on Low Sensitivity. Red Trace Shows Camera Gate.
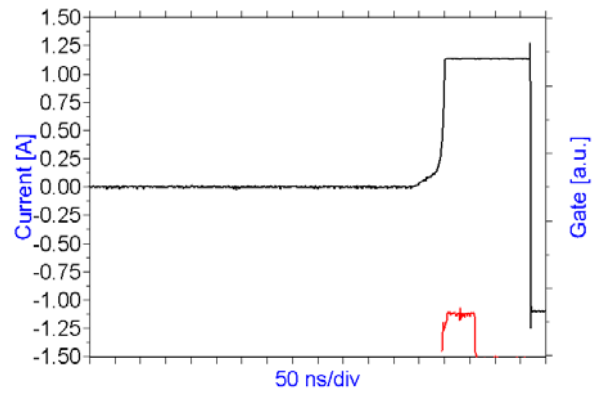

Figure 44. Same as Figure 43 but with Medium Sensitivity. Current Peak is Clipped.
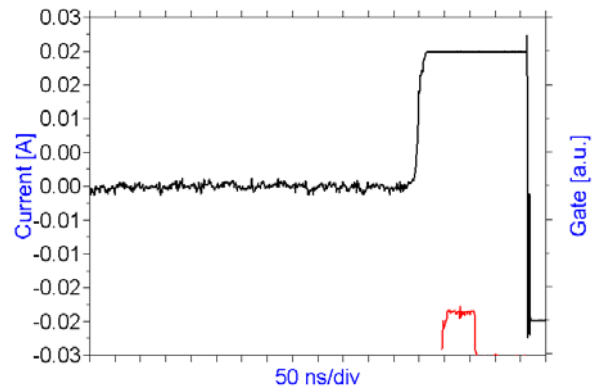

Figure 45. Same as Figure 43 but with High Sensitivity. Current Peak is Clipped.
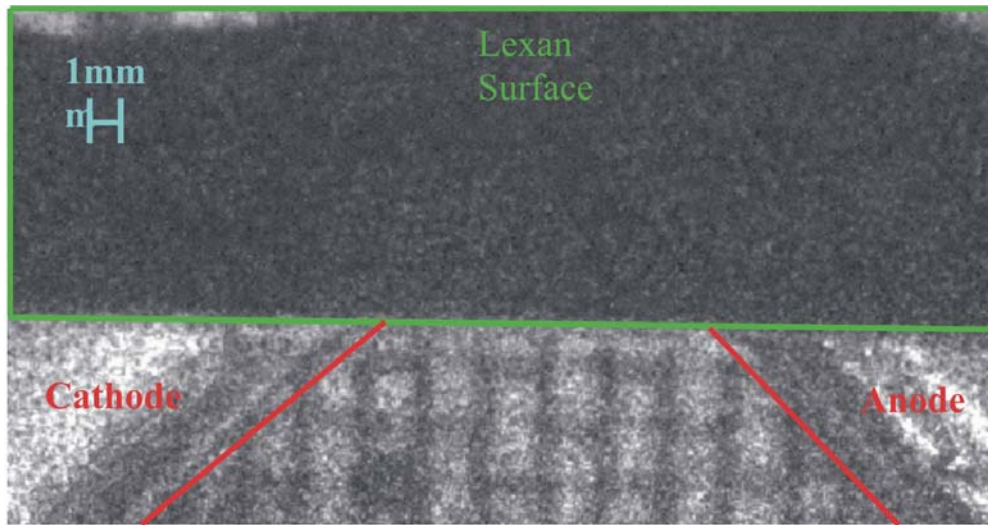
Figure 46. Side-on Reference Image with Planar Surface, 11 mm Gap. Image is Rotated 180^0 with Respect to Figure 29

7.3.2 Side-on Imaging for Modified Electrode Geometry with Planar Dielectric Surface

The same basic behavior was observed for a planar surface as was observed for the grooved surface. This is shown in Figures 46 through 58. The electrodes are again, the modified electrode geometry shown in Figure 27. A side view of the electrode-surface geometry (flipped 180°) is shown in Figure 46. The dielectric surface is outlined in green and the electrodes are outlined in red. Although there is a strong electric field component normal to the surface, the breakdown channel in air (Figure 55) never lifted off the surface, while it did lift off the surface in nitrogen (Figures 47 and 51).

7.3.3 Top-view Imaging and Current Waveforms of Pre-breakdown Pulses in Nitrogen

In this section we will examine images from the top view of the Lexan surface for various pre-breakdown pulses shown in the accompanying current waveforms. The electrodes are the modified electrode geometry shown in Figure 27. The gas is nitrogen.

Figures 59 and 60 are typical of the extremely early pre-breakdowns, which occurred least often of all the pre-breakdowns in nitrogen – happening roughly 10% of the time. The current trace shown in Figure 60 is from the high sensitivity current sensor. The off-axis nature of the breakdown image could be due to a small irregularity in the electrode-dielectric geometry. Figures 61 and 62 are typical of pre-breakdowns that occur just prior to the main breakdown; these are the second most common form of pre-breakdown occurring about 35% of the time. Finally, Figures 63 and 64 are typical of the most common form of pre-breakdown, which takes the form of a very slow rise in the current immediately preceding the main breakdown. This type of pre-breakdown occurs over 50% of the time. About 5% of the current waveforms lacked the slow rising phase almost completely and made a rather immediate transition to high current amplitudes.
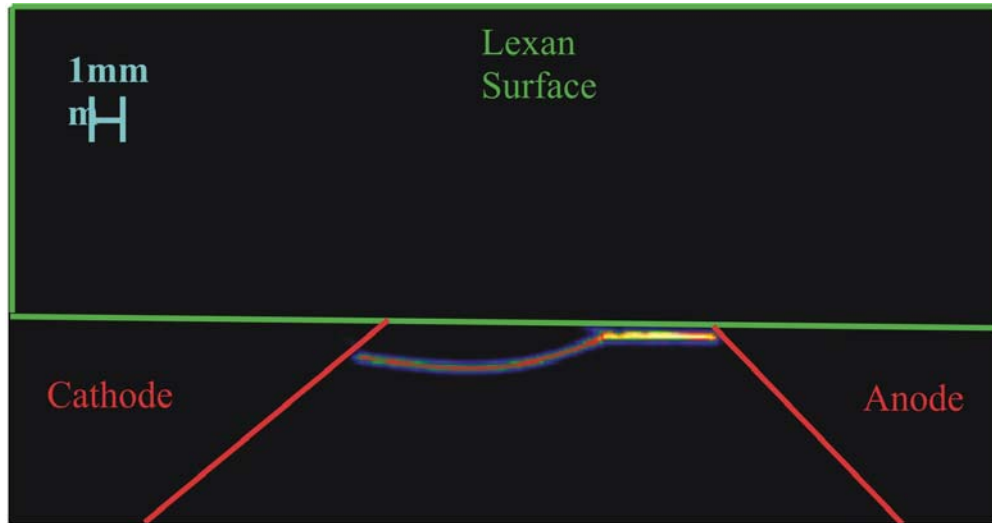
Figure 47. Side-on Image of Main Breakdown in N_2 with Planar Surface, 11 mm Gap. Breakdown Voltage, $V_b = 11$ kV.
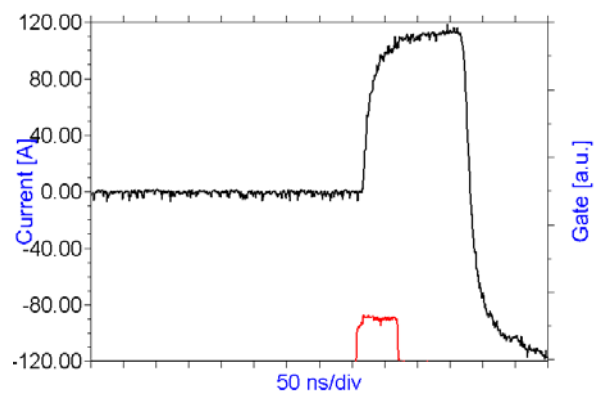

Figure 48. Discharge Current versus Time for Flashover Event Depicted in Figure 47. Sensor Set on Low Sensitivity. Red Trace Shows Camera Gate.
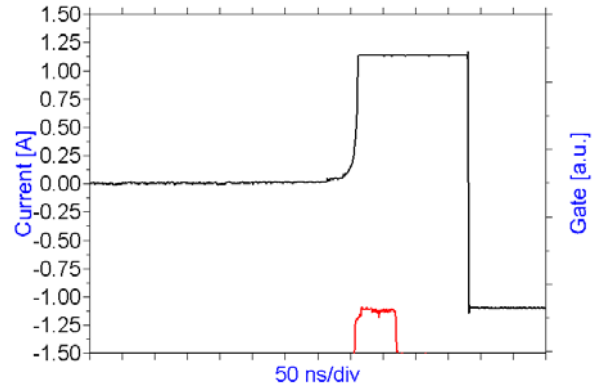
Figure 49. Same as Figure 48 but with Medium Sensitivity. Current Peak is Clipped.
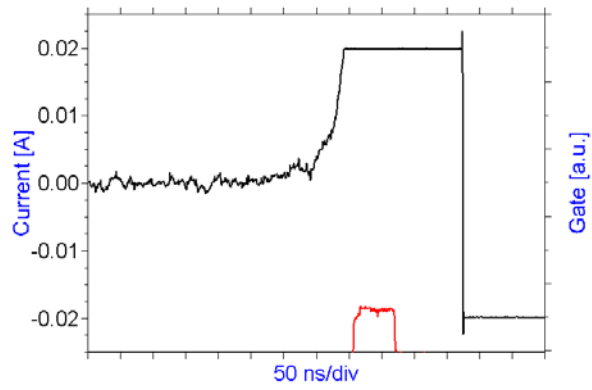

Figure 50. Same as Figure 48 but with High Sensitivity. Current Peak is Clipped.
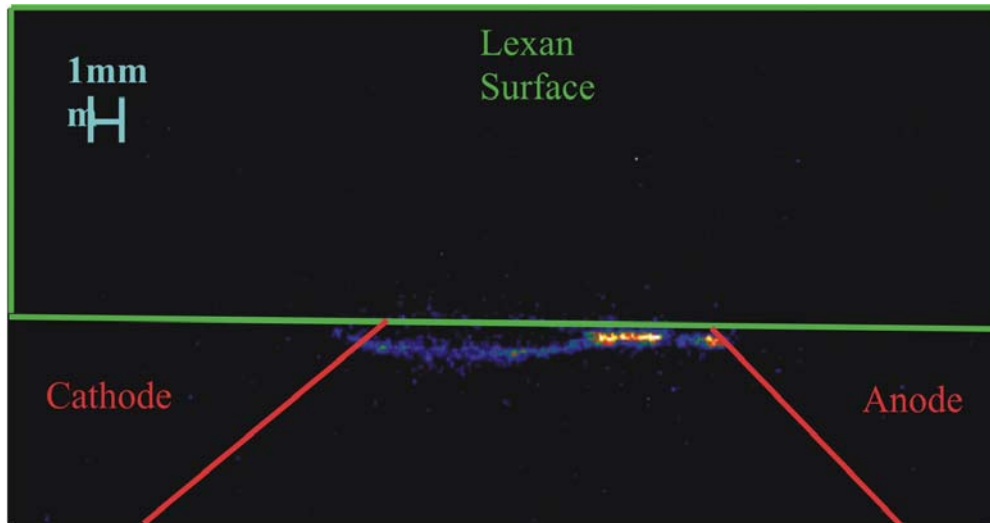

Figure 51. Side-on Image of Pre-breakdown in N_2 with Planar Surface, 11mm Gap. Breakdown Voltage, $V_b = 6.5$ kV.

Figure 52. Discharge Current versus Time for Flashover Event Depicted in Figure 51. Sensor Set on Low Sensitivity. Red Trace Shows Camera Gate.

Figure 53. Same as Figure 52 but with Medium Sensitivity. Current Peak is Clipped.

Figure 54. Same as Figure 52 but with High Sensitivity. Current Peak is Clipped.

Figure 55. Side-on Image of Main Breakdown in Air with Planar Surface, 11 mm Gap. Breakdown Voltage, $V_b = 20$ kV.
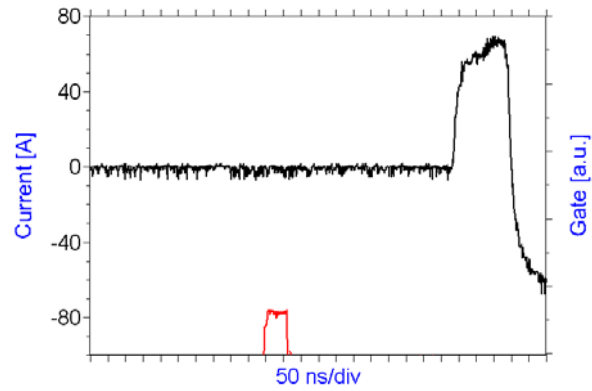

Figure 56. Discharge Current versus Time for Flashover Event Depicted in Figure 55. Sensor Set on Low Sensitivity. Red Trace Shows Camera Gate.
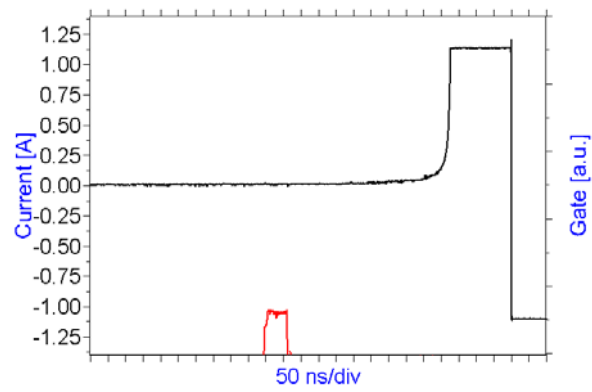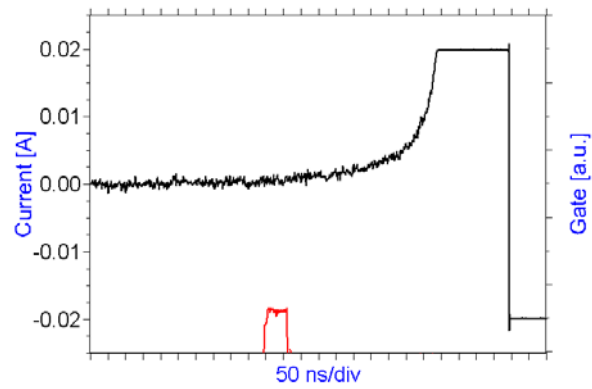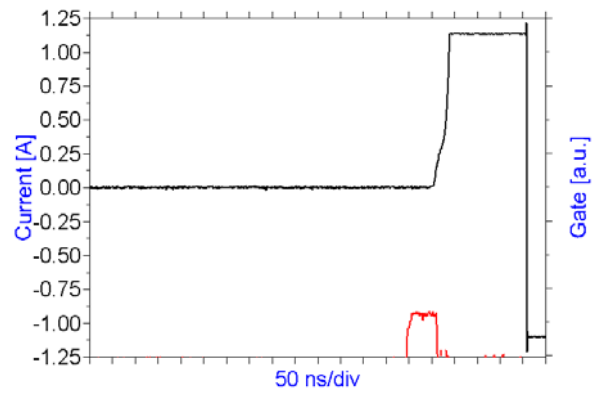
Figure 57. Same as Figure 56 but with Medium Sensitivity. Current Peak is Clipped.

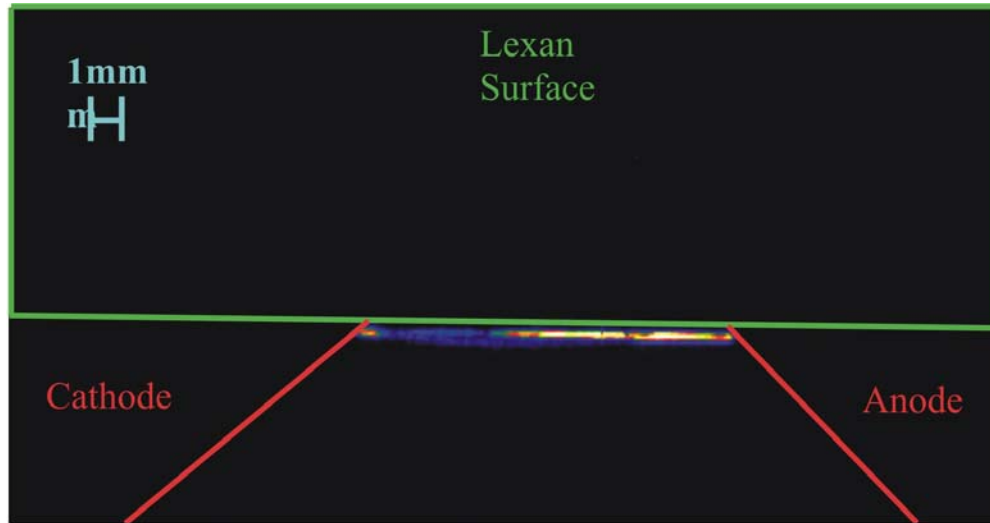Figure 58. Same as Figure 56 but with High Sensitivity. Current Peak is Clipped.

Figure 59. Top View of Pre-breakdown Across Flat Lexan Surface in N_2. Electrodes Shown in Red.

Figure 60. Discharge Current versus Time for Flashover Event Depicted in Figure 59. Sensor Set on High Sensitivity. Red Trace Shows Camera Gate.

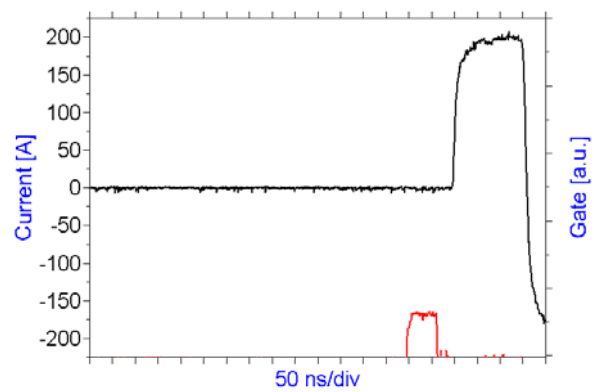Figure 61. Top View of Pre-breakdown Across Flat Lexan Surface in N_2. Electrodes Shown in Red.

Figure 62. Discharge Current versus Time for Flashover Event Depicted in Figure 61. Sensor Set on High Sensitivity. Red Trace Shows Camera Gate.
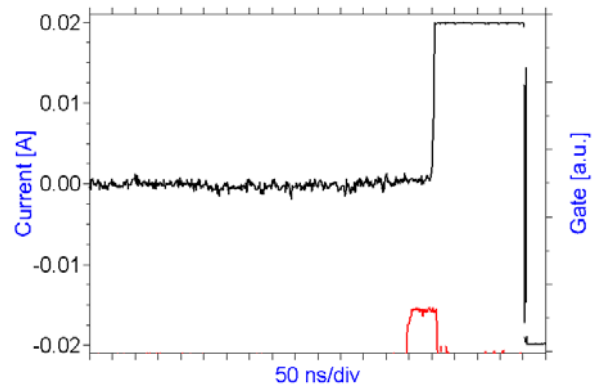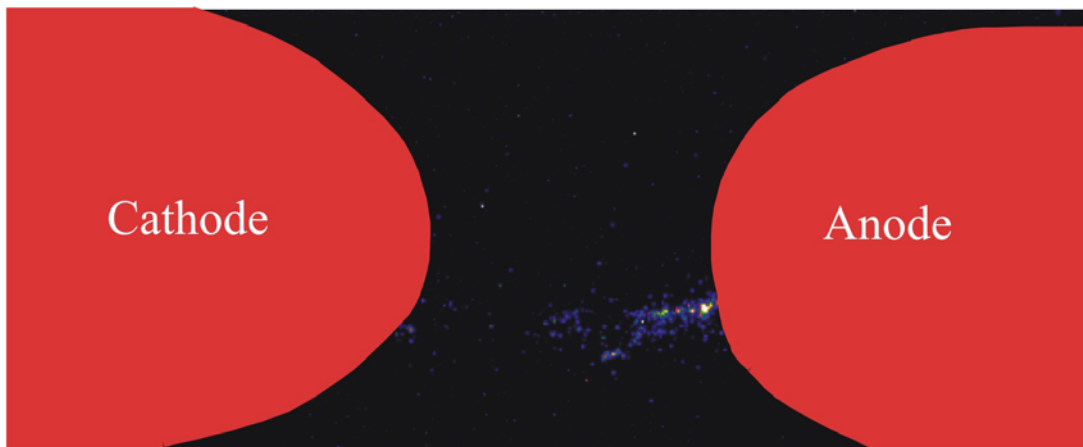
7.3.4 Side-view Imaging and Current Waveforms of Pre-breakdown Pulses in Air

In air pre-breakdown can occur anywhere from several μs (up to 100 μs or more) before main breakdown to immediately preceding the main breakdown. The pre-breakdowns occur just as often early as they do right before the main breakdown. Figures 65 - 70 show typical results progressing from very early pre-breakdown (Figures 65 and 66) to pre-breakdown 1 μs prior to main breakdown (Figures 67 and 68) and finally to pre-breakdown right before the main breakdown (Figures 69 and 70).

7.3.5 Temporally and Spatially Resolved Flashover Light Emission

Results in this section depict the light emission from anode and cathode as detected with fiber optics and individual PMT's, arranged as shown in Figure 31. It is apparent that the PMT's detect light emission before the current sensors can detect current, which simply means that the light detection scheme is more sensitive than the current diagnostics.

In general, any light emission is detected first from the cathode, which may be in the form of an early spike as visible, for instance, in Figures 71 and 72 (the black trace in the plots labeled "PMT Sensors"). After any initial spike, the anode signal rises earlier than the cathode signal, indicating a streamer growing from anode to cathode. If there is no initial spike, the cathode light signal stays up high and is followed by light emission from the anode about 100 to 150 ns later.
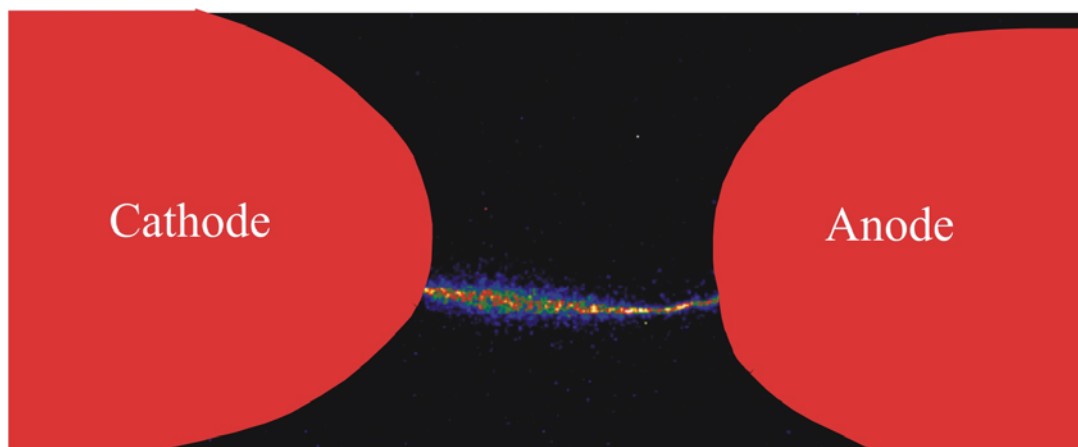
Figure 63. Top View of Pre-breakdown Across Flat Lexan Surface in N_2. Electrodes Shown in Red.
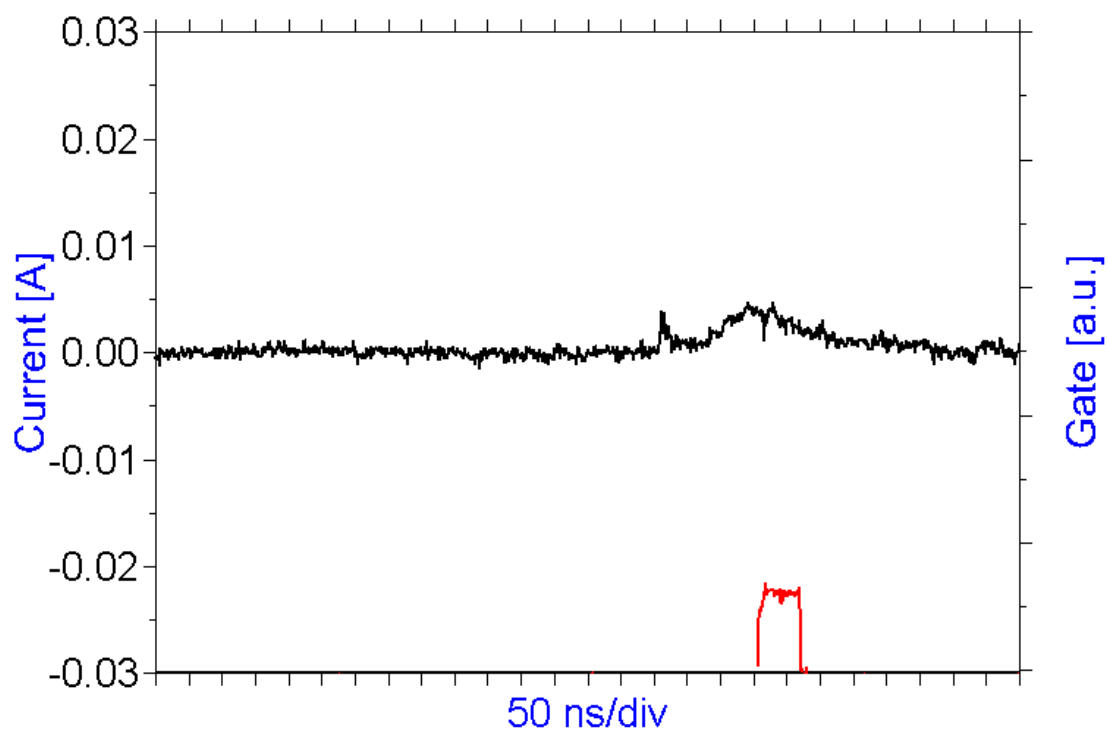

Figure 64. Discharge Current versus Time for Flashover Event Depicted in Figure 63. Sensor Set on High Sensitivity. Red Trace Shows Camera Gate.
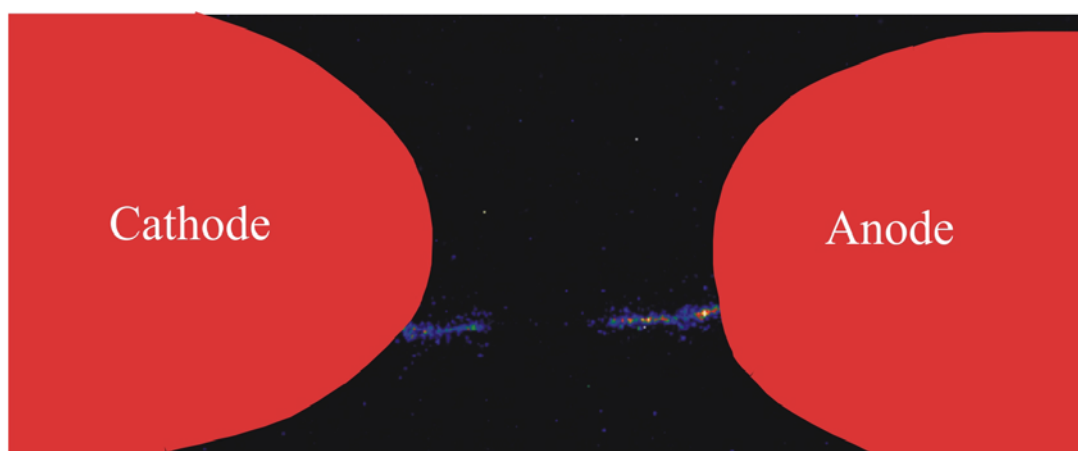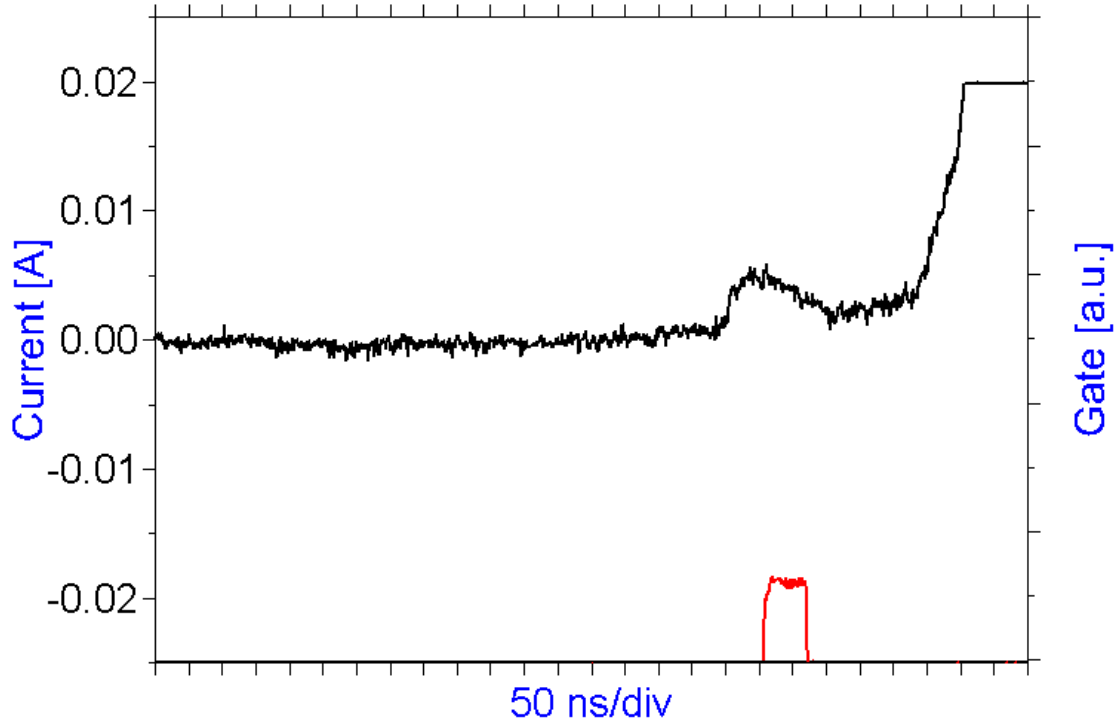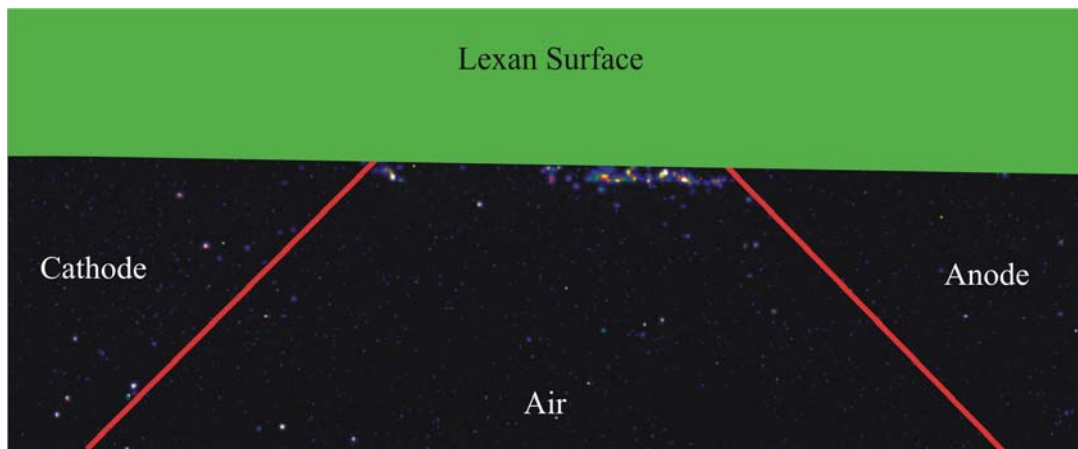
Figure 65. Pre-breakdown in Air
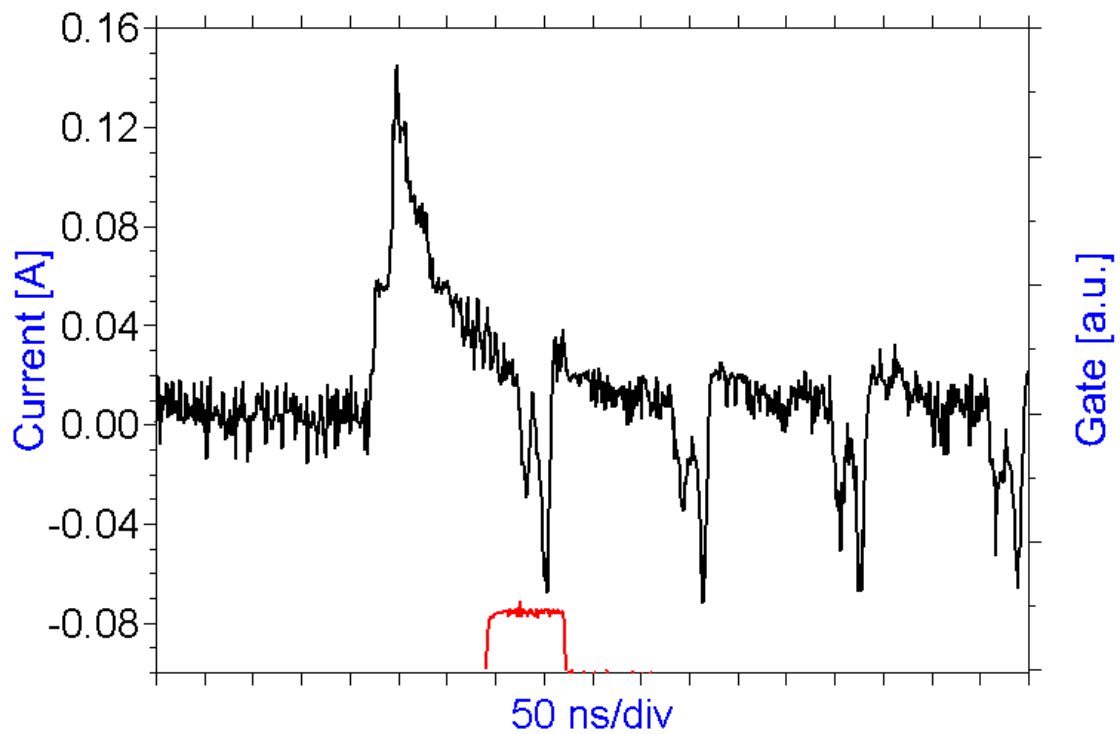
Figure 66. Discharge Current versus Time for Flashover Event Depicted in Figure 65. Sensor Set on Medium Sensitivity. Red Trace Shows Camera Gate.

Figure 67. Pre-breakdown in Air Approximately 1 μs Prior to Main Breakdown.

Figure 68. Discharge Current versus Time for Flashover Event Depicted in Figure 67. Sensor Set on High Sensitivity. Red Trace Shows Camera Gate.

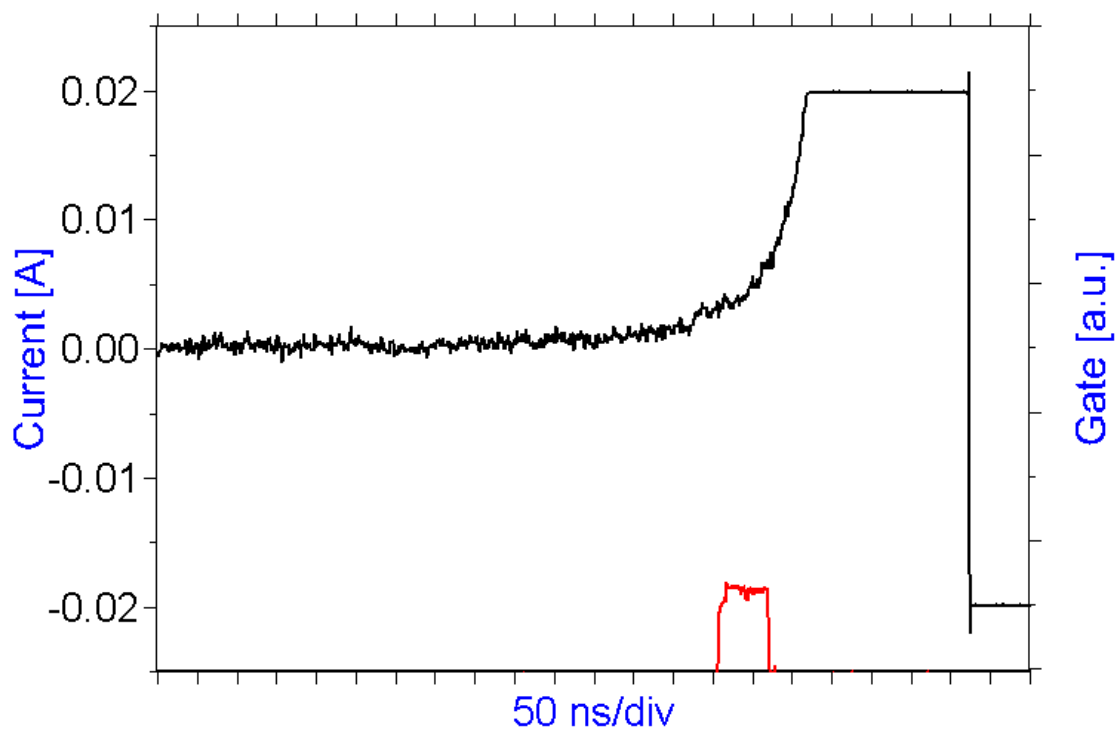Figure 69. Pre-breakdown ∼200 ns Prior to Main Breakdown.
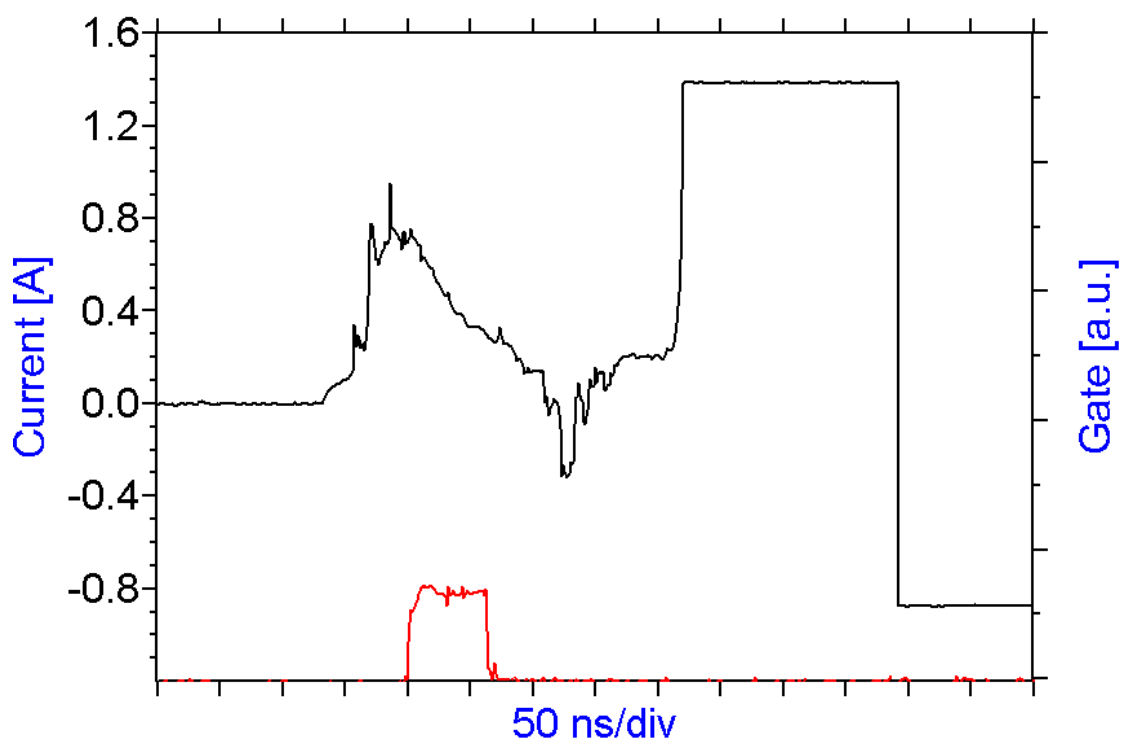
Figure 70. Discharge Current versus Time for Flashover Event Depicted in Figure 69. Sensor Set on Medium Sensitivity. Red Trace Shows Camera Gate.
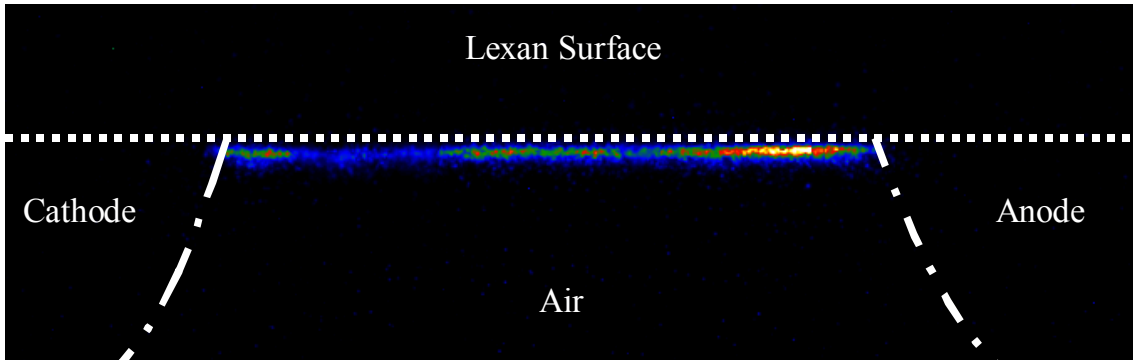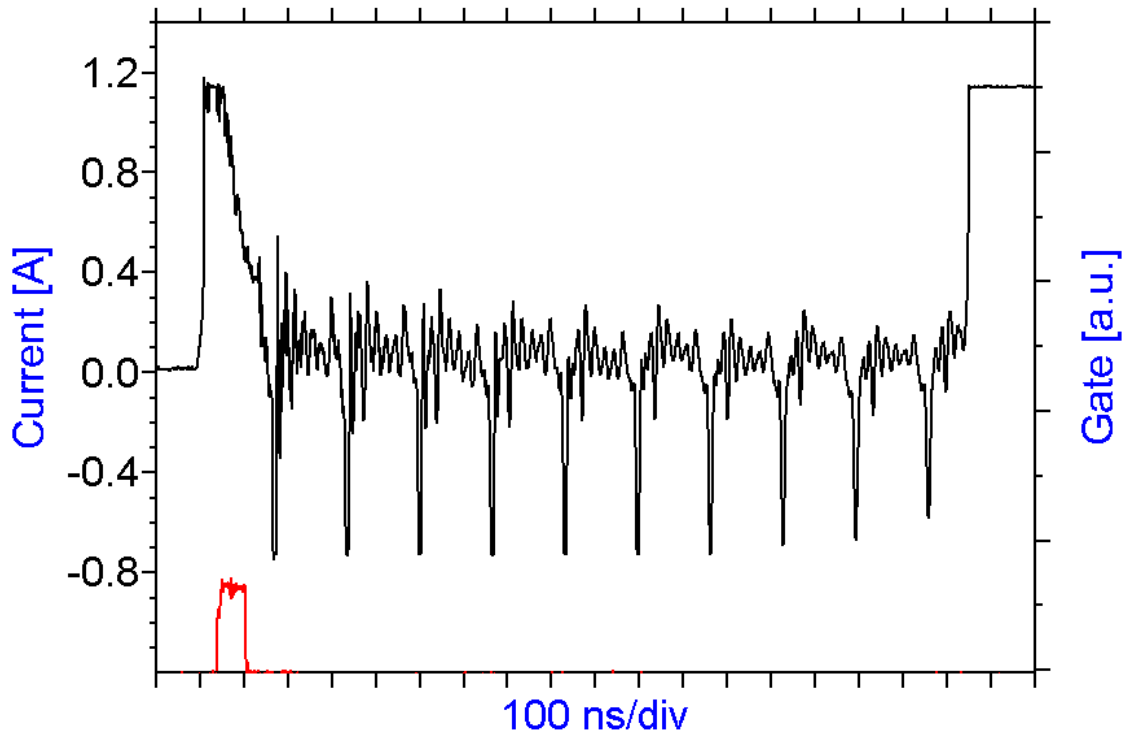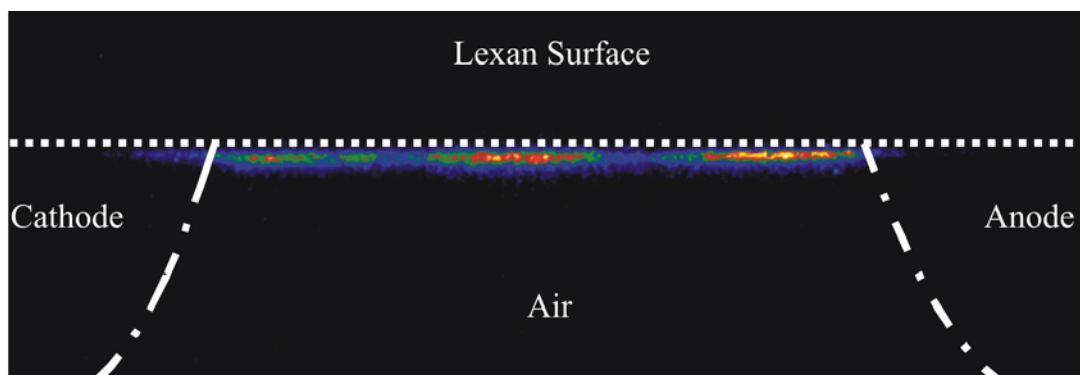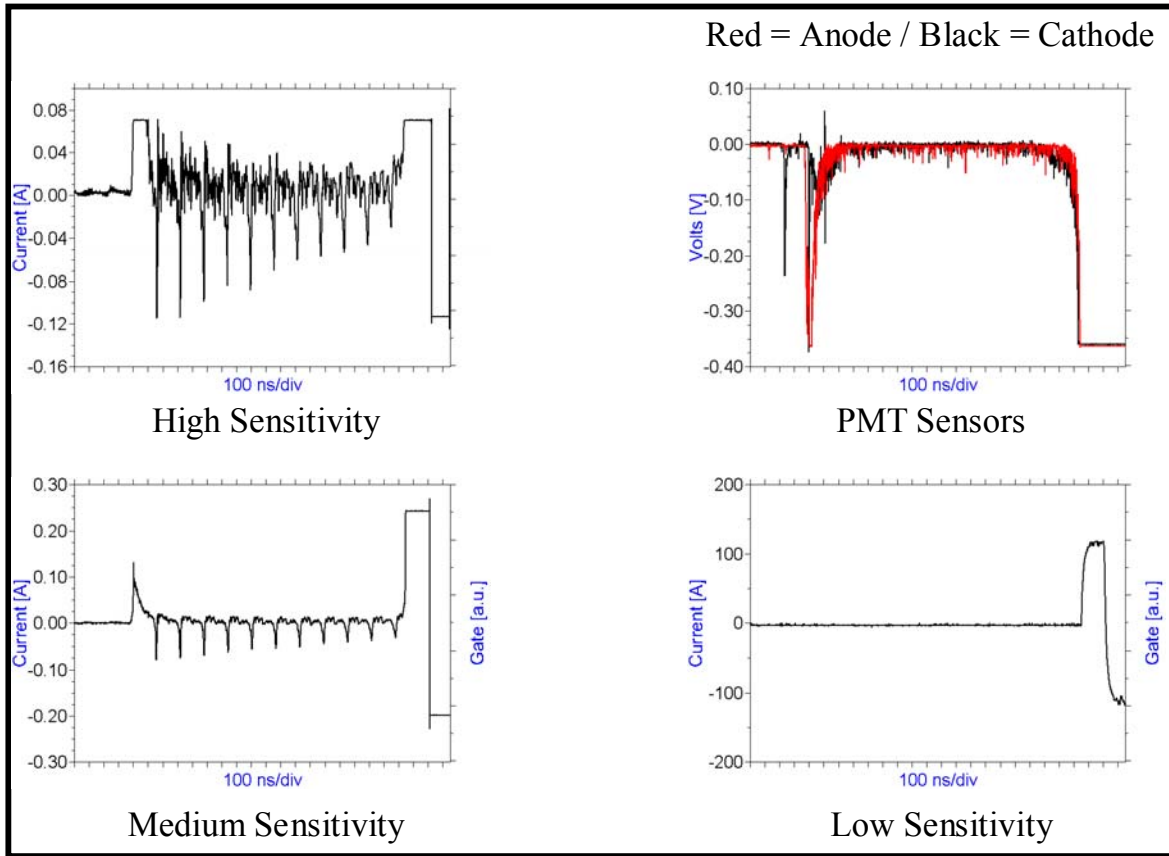
Figure 71. Current Waveforms and PMT Signals with 2 Channel PMT Setup

Results for the 3-channel setup are shown in Figures 73 - 77. It should be noted that the light emission in the center of the gap (red trace) is always last, which means that the discharge starts at cathode, moves to anode and propagates back towards the cathode from the anode.

7.3.6 Temporally and Spatially Resolved Flashover Optical Emission Spectroscope

Emission spectrum data were taken at various locations along the breakdown gap during the main discharge using the fiber-optic setup shown in Figure 31. The spectra at the different locations exhibit a distinct difference in the appearance of spectral peaks, as shown in Figure 78. In particular, the spectrum originating from the gap middle completely lacks any metal spectra, which are clearly visible at both anode and cathode. This was expected since the time scales of breakdown are much shorter than the time scales for diffusion across the 10 mm gap. Even ions are unlikely to make it across the gap due to their low mobility in the background gas at a pressure of 1 atmosphere. The calculated spectral library (only part of which is shown in Figures 80 - 83) aided in identifying some of the spectral lines. Some of the lines, however, remain unidentified and more spectra will need to be taken and analyzed in the future.

7.3.7 Measured DC Breakdown Voltage

We measured repeatedly the DC breakdown voltage using the standard electrode geometry shown in Figure 26 both with and without the Lexan surface present. Figure 84 shows the measured breakdown voltage as a function of test run. The gap was 12.4 mm wide and the surrounding gas was air. The results

High Sensitivity   PMT Sensors

Medium Sensitivity   Low Sensitivity
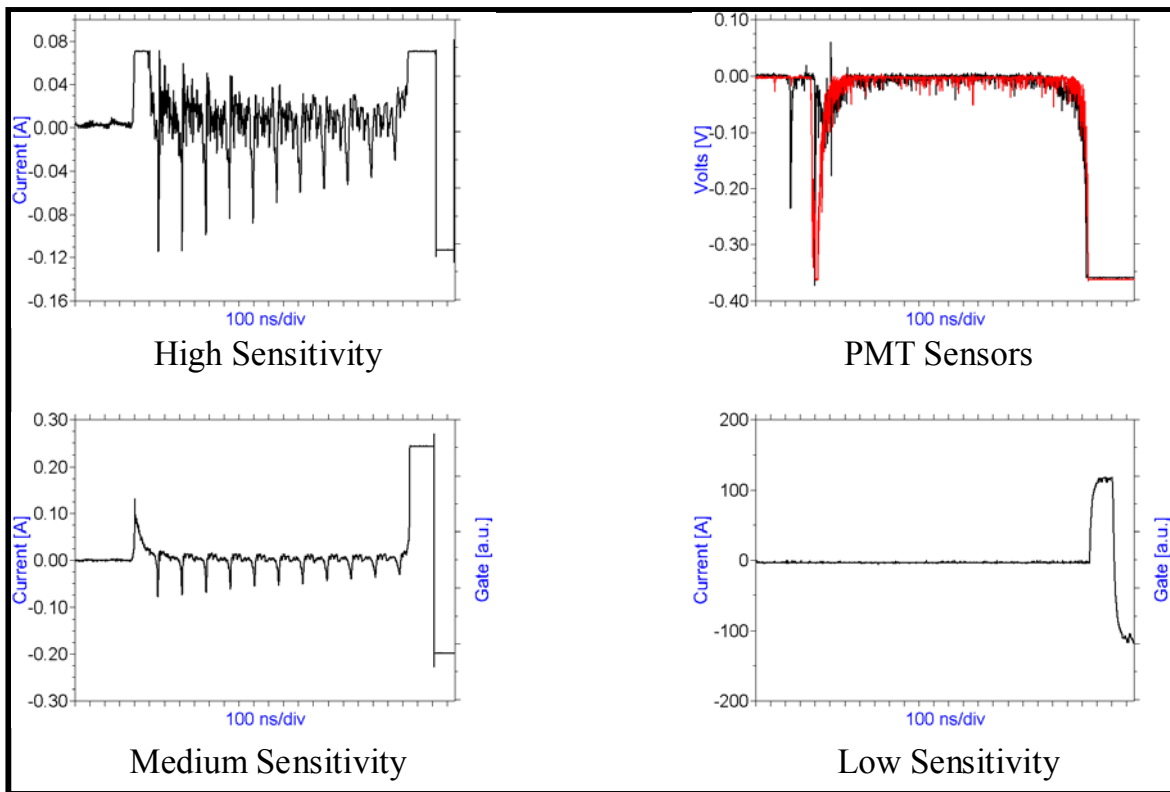
Figure 72. Current Waveforms and PMT Signals with 2 Channel PMT Setup
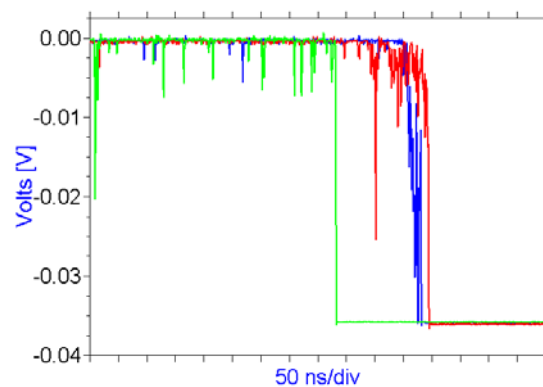
Figure 73. Three Channel PMT Setput.   Green is the Cathode PMT. Blue is the Anode PMT. Red is the PMT at Gap Center.
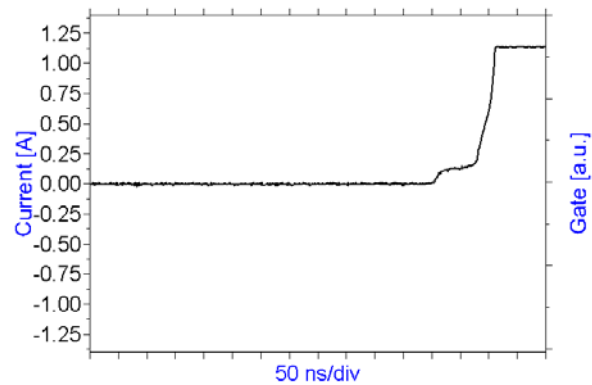
Figure 74. Current versus Time Measured with Medium Sensitivity Sensor for PMT Output of Figure 73. Current is Clipped.
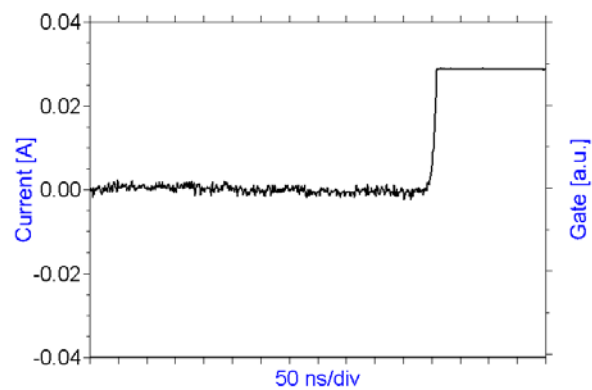
Figure 75. Current versus Time Measured with High Sensitivity Sensor for PMT Output of Figure 73. Current is Clipped.
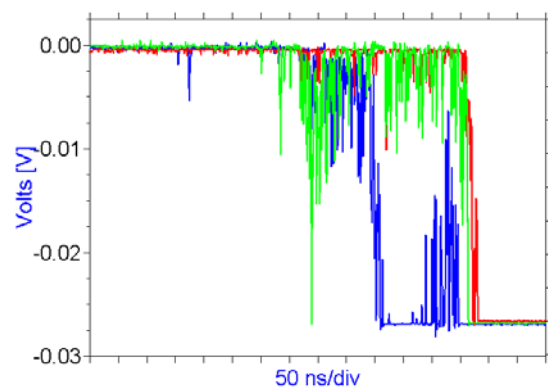
Figure 76. Three Channel PMT Setput. Green is the Cathode PMT. Blue is the Anode PMT. Red is the PMT at Gap Center.
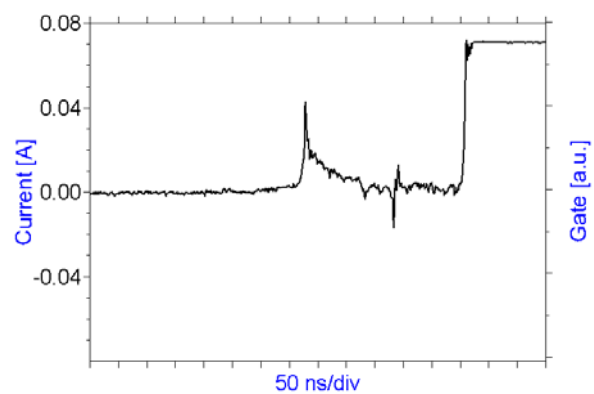
Figure 77. Current versus Time Measured by High Sensitivity Sensor for PMT Output of Figure 76.
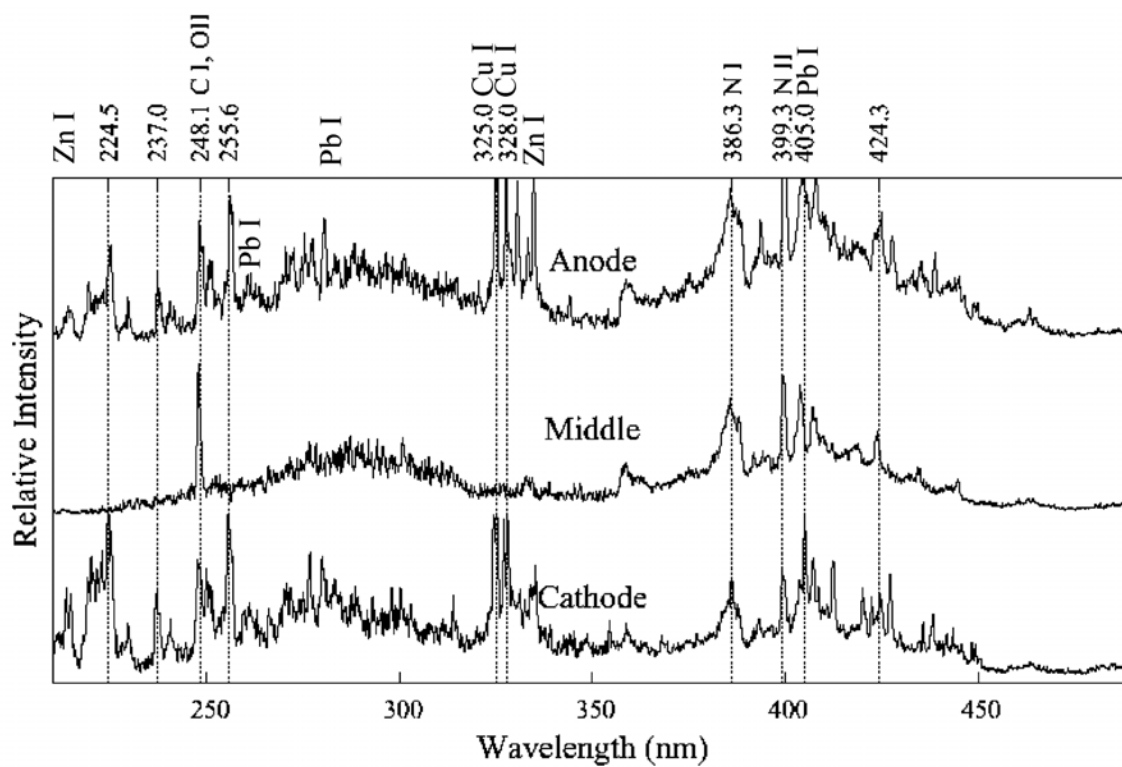
Figure 78. Emission Spectra in Air, Temporally Integrated over 80 ns.
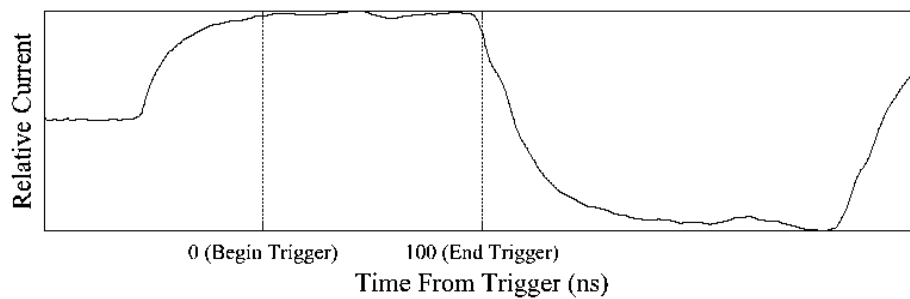
Figure 79. Current and Gate for Figure 78
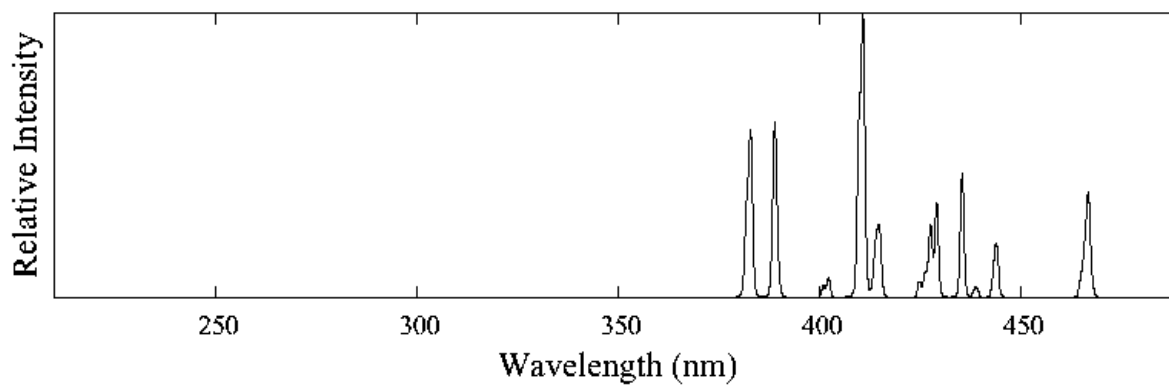
Figure 80. Calculated Emission Spectrum for NI at T=0.8 ev.
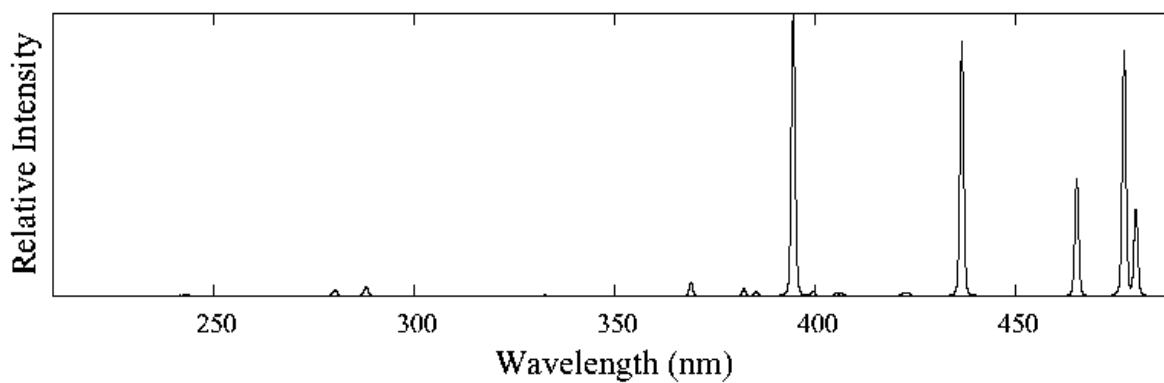
Figure 81. Calculated Emission Spectrum for OI at T=0.8 ev.
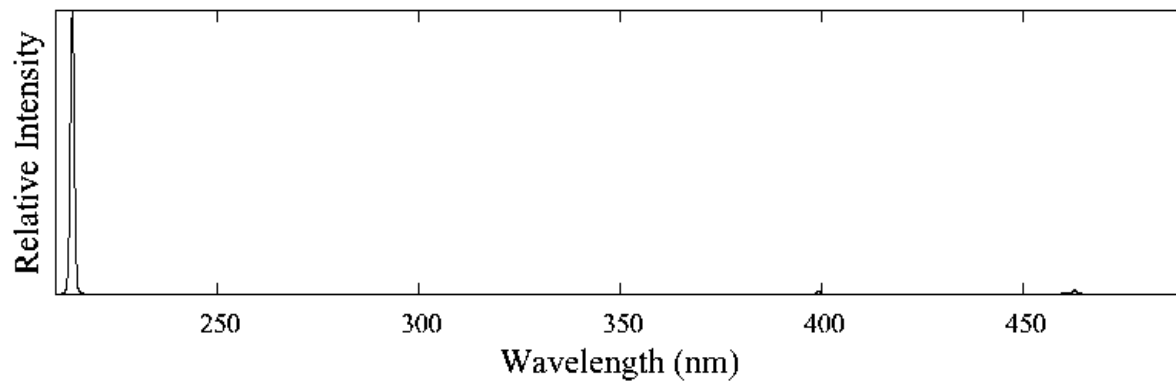
Figure 82. Calculated Emission Spectrum for NII at T=0.8 ev.
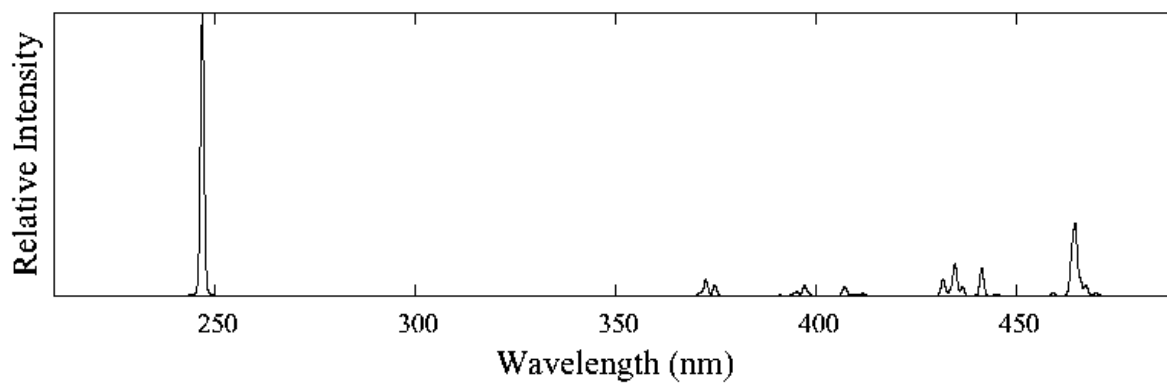
Figure 83. Calculated Emission Spectrum for OII at T=0.8 ev.
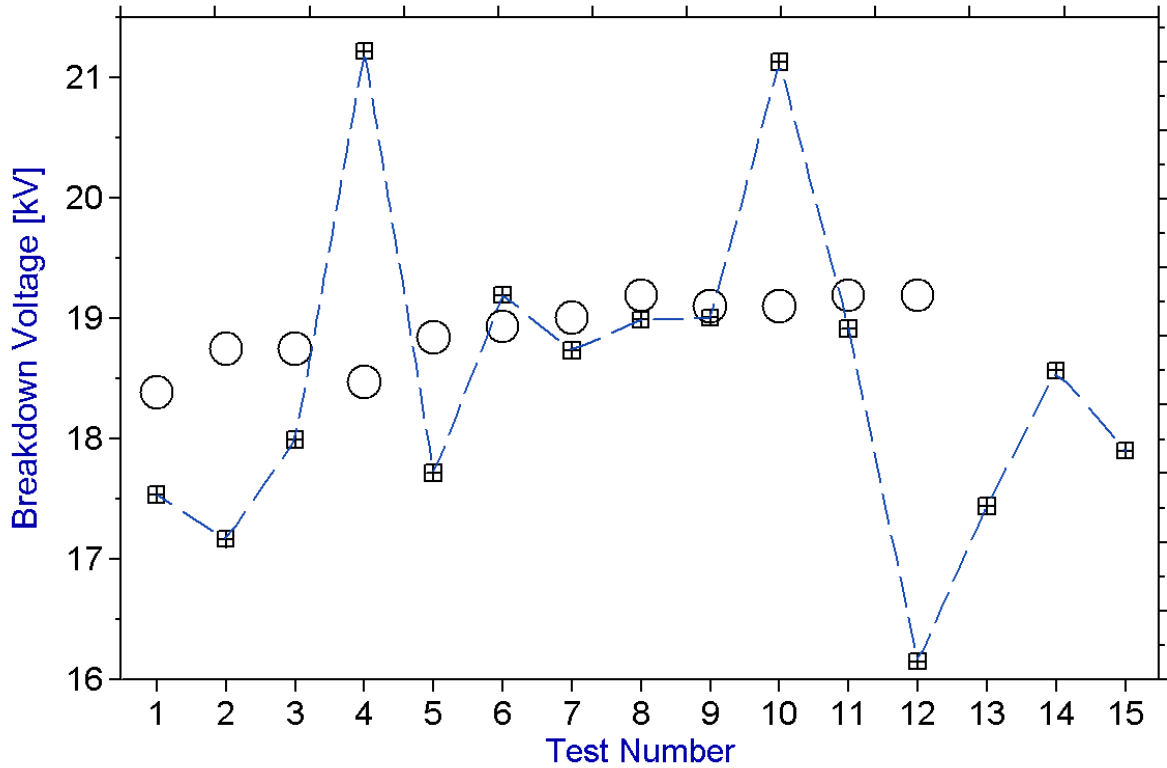
Figure 84. Breakdown Voltage Over a 12.4 mm Gap, Nonuniform Field, With (+) and Without (O) Lexan Surface Present.

show that the gap without Lexan breaks down between 18 kV and 19 kV. Adding the surface causes more variation in the breakdown voltage, perhaps caused by metallic deposits or residual charges that build up over several shots and are removed by subsequent shots. The variations are on the order of 10%. At this small gap width, we did not measure a large decrease in standoff voltage as one might expect due to the presence of the surface (see Figure 3).

7.4   Summary of Experimental Results

We have used state-of-the-art equipment to develop a detailed experimental picture of dielectric surface flashover at atmospheric pressure. Two gases, ambient air and dry nitrogen, have been tested and have exhibited significant differences in the observed discharge development.

In some cases the air flashover occurs at approximately twice the applied gap voltage as compared to dry nitrogen, however, statistically the voltages observed at flashover are about the same for dry nitrogen and air. The flashover-channel in air always follows the surface, even if there is a strong field component normal to the dielectric surface. The breakdown activity is generally detected first at the cathode, followed by the anode, and then the center of the gap, which is similar to the behavior of volume breakdown in gases. We consider this a strong indication of a first electron avalanche going across the gap, generating an appreciable amount of light as the electrons are emitted from the cathode, followed by a cathode-directed streamer.

The pre-breakdown current spikes, which can be as early as 100 μs or more before the final breakdown,

are considered a first unsuccessful electron avalanche that fails to make the transition to a fully developed arc channel. These unsuccessful avalanches are basically the rule in air, but are extremely rare in nitrogen. Hence, one must assume that the strong, electronegative oxygen in the air attaches to the electrons, thus preventing some avalanches from making the final transition to achieve breakdown.

At present, we suggest two electron amplification mechanisms. The first is associated with the volume alone, i.e. standard Townsend multiplication, and the second is electron emission from the surface. Electrons and/or photons in the UV impacting the surface trigger this electron emission from the surface. Volume ionization due to photoionization in the gas may also play some role in the initial phase and could be suggested as a third amplification process.

The two main amplification processes are weighted differently in air, which includes oxygen as a electronegative gas, and in nitrogen. In air, the surface electron emission plays a much more dominant role as corroborated by our side-on imaging always showing the flashover following the surface even in the presence of a strong normal electric field. In nitrogen, the flashover channel path depends to a much lesser extend on the presence of the surface. It might even lift off the surface under only a small normal electric field component and definitely lifts off in the geometry with the strong normal field component.

8   Conclusions

In this project we attempted to ascertain the role of photoemission in the breakdown process. Monte Carlo simulations indicate that photoemission does play a role at low field values near the breakdown threshold. The number of electrons contributed to the avalanche by the photoemission process is greater than the number of electrons contributed by the photoionization process and in some cases – in particular for polyethylene at low field – is greater than the number of electrons contributed by the collisional ionization process. We also found that the introduction of the surface introduces two processes that balance each other in terms of electron contribution to the problem space. At low energies, which are important to the beginning of the avalanche process, electrons stick to the surface due to secondary electron emission and are removed from the avalanche. Photoemission causes electrons to be added to the avalanche from the surface. The overall effect, though, is that more electrons are removed by the surface than added; approximately 6% of the electrons added by collision are removed by the surface. The removal of electrons by secondary electron emission is important to our simulations where we started with a fixed number of electrons and observed the growth of the electron avalanche. In fact, we found if we started with too few initial electrons (we started with 1000), the surface collected all of them and the avalanche stopped. If electrons were continually added to the problem space at the origin throughout the simulation eventually the surface would charge negatively, keep electrons from colliding with the surface and reduce the secondary electron emission effect. It is anticipated that then the surface would only supply electrons to the avalanche through photoemission. This is the subject of future work.

These results seem to support those of Verhaart [11], who noted that in SF6, photoemission became the prevalent contributor to the avalanche below a critical value of field. Verhaart also noted that no photoemission effect was observed in N_2 if the insulator was uncharged, or pre-charged with positive charge. Only if the insulator was pre-charged with negative charge was an effect observed. This leads us to speculate that the pre-charging of the surface could keep secondary electron emission effects from acting like a sink for the avalanche electrons so that only the photoemission effect would be observed.

This project suffered from a lack of data, particularly for photoemission. We were only able to find photoemission data for two materials: Teflon and polyethylene. Accounting for charging of the dielectric is critical to accurate measurements of photoemission and each experimenter seemed to handle charging differently. It was difficult to assess which experiment gave the most reliable quantum efficiency data.

Secondary electron emission data for polymers was more plentiful, but was directed at applications involving high energy electrons. It was, therefore, difficult to assess if the data at the low energies we needed were accurate. It would have been nice to have both secondary electron emission data and photoemission data for nylon, since a large effect was observed on the avalanche due to a nylon spacer [9].

In the future, with regard to the Monte Carlo simulation, we plan to add the effect of a continuous source of electrons from the cathode in order to observe the effect on secondary electron emission. We will also try pre-charging the surface before starting the simulation. If data on nylon become available, we will run a simulation on that material. Late in the project we discovered a listing of some apparent cross sections for excitation in nitrogen [38]. We will change to those to see if the results change.

Experimentally it would be instructive to test nitrogen/oxygen mixtures with various percentages of oxygen (starting at 21% for air to 0% for pure nitrogen). At a certain mixture ratio, the flashover channel should make the transition from always following the surface to lifting off the surface. The electron attachment rate at this point could be calculated and serve as a quantitative comparison for the rate of secondary electron amplification. Overall, further data evaluation and experimental work is needed to develop a more quantitative understanding of the surface flashover processes. Specifically, optical emission spectroscopy in connection with other gases such as dry air, nitrogen, or argon is considered to have a high pay-off potential. The overall goal should be to develop a model based on the observed physics that will mirror the experimental behavior.

9   References

[1]   J. M. Meek and J. D. Craggs, *Electrical Breakdown of Gases,* John Wiley and Sons, 1978, pp. 533-653.

[2]   J. M. Meek and J. D. Craggs, *Electrical Breakdown of Gases*, Oxford, Clarendon Press, 1953, pp. 337-340.

[3]   J. D. Cobine, *Gaseous Conductors Theory and Engineering Applications*, Dover, 1958, p. 166.

[4]   F. W. Maxstadt, "Insulator Arcover in Air," *Electrical Engineering*, vol. 53, July 1934, pp. 1062-1068.

[5]   R. E. Jorgenson, L. K. Warne and E. E. Kunhardt, "Lightning Induced Arcing: An LDRD Report," *Sandia Report SAND2000-3044*, Dec. 2000.

[6]   E. M. Bazelyan and Yu. P. Raizer, *Spark Discharge*, CRC Press, Boca Raton, FL, 1997, pp. 151-155.

[7]   G. L. Weissler, "Photoionization in Gases and Photoelectric Emission from Solids," *Encyclopedia of Physics, vol. 21*, S. Flugge Editor, Springer-Verlag, Berlin, 1956, pp. 305-341.

[8]   M. Fujihira and H. Inokuchi, "Photoemission from Polyethylene," *Chemical Physics Letters*, vol. 17, no. 4, December 1972, pp. 554-556.

[9]   S. M. Mahajan, T. S. Sudarshan "Measurements of Electrical Avalanches and Optical Radiation Near Solid Insulators in High Pressure (up to 0.3 MPa) Nitrogen Gas," *J. Appl. Phys.* vol. 69, no. 5, March 1991, pp. 2877-2884.

[10]   J. Tom, H. F. A. Verhaart, A. J. L. Verhage, C. S. Vos, "Photo-emission of Charged Insulators in Insulating Gases," *Proceedings of the 2nd International Conference on Conduction and Breakdown in Solid Dielectrics*, Erlangen, 1986, pp. 301-307.

[11]   H. F. A. Verhaart, J. Tom, A. J. L. Verhage, C. S. Vos, "Avalanches Near Solid Insulators," *Proceeding of the 5th International Symposium on HV Engineering*, Braunschweig, 1987, Paper 13.01.

[12]   A. Jaksts and J. Cross, "The Influence of a Solid Dielectric Spacer on Electron Avalanches in Nitrogen at Atmospheric Pressure," *Canadian Electrical Engineering Journal,* vol. 6, no. 2, 1981, pp. 14-18.

[13]   N. L. Allen, "The Propagation of Positive Streamers in Air and at Air/Insulator Surfaces," *American Institute of Physics, Conference Proceedings 1996*, no. 363, 1996, pp. 247-256.

[14]   N. L. Allen, A. Ghaffar, "Propagation of Positive Streamers of Insulating Surfaces in Air," *Proceedings*

of the Conference on Electrical Insulation and Dielectric Phenomena, 22-25 October 1995, Virginia Beach VA, pp. 447-450.

[15] N. L. Allen and P. N. Mikropoulos, "Streamer Propagation Along Insulating Surfaces," *IEEE Transactions on Dielectrics and Electrical Insulation*, vol. 6, no. 3, June 1999, pp. 357-362.

[16] E. Nasser, *Fundamentals of Gaseous Ionization and Plasma Electronics*, John Wiley and Sons, New York, 1971, pp. 191-197.

[17] R. V. Langmuir, *Electromagnetic Fields and Waves*, McGraw Hill Co. Inc., New York, 1961, pp. 63-64.

[18] G. F. Dionne, "Effects of Secondary Electron Scattering on Secondary Emission Yield Curves," *J. Apply. Phys.*, vol. 44, no. 12, December 1973, pp. 5361-5364.

[19] J. R. Young, "Penetration of Electrons and Ions in Aluminum," *J. Apply. Phys.*, vol. 27, no. 1, 1956, pp. 1-4.

[20] E. A. Burke, "Secondary Emission from Polymers," *IEEE Transactions on Nuclear Science*, vol. NS-27, no. 6, December 1980, pp. 1760-1764.

[21] J. J. Scholtz, D. Kijkkamp and R. W. A. Schmitz, "Secondary Electron Emission Properties," *Philips J. Res.*, vol. 50, 1996, pp. 375-389.

[22] R. F. Willis and D. K. Skinner "Secondary Electron Emission Behavior of Polymers," *Solid State Communications*, vol. 13, 1973, pp. 685-688.

[23] D. C. Cartwright, S. Trajmar, A. Chutjian, and W. Williams, "Electron Impact Excitation of the Electronic States of N_2. II. Integral Cross Sections at Incident Energies from 10 to 50 ev.," *Physical Review A*, vol. 16, no. 3, September 1977, pp. 1041-1051.

[24] M. Imami and W. L. Borst, "Electron Excitation of the (0,0) Second Positive Band of Nitrogen from Threshold to 1000 ev," *Journal of Chemical Physics*, vol. 61, no. 3, August 1974, pp. 1115-1117.

[25] L. G. Christophorou, *Atomic and Molecular Radiation Physics*, John Wiley and Sons, New York, 1971, pp. 109-146.

[26] R. W. B. Pearse and A. G. Gaydon, *The Identification of Molecular Spectra*, 3rd Edition, John Wiley and Sons, New York, 1976, pp. 217-229.

[27] A. Lofthus and P. H. Krupenie, "The Spectrum of Molecular Nitrogen," J. Phys. Chem. Ref. Data, vol. 6, no. 1, 1977, pp. 113-307.

[28] R. E. Huffman, Y. Tanaka, and J. C. Larrabee, "Fluorescence and Pre-Ionization in Nitrogen Excited by Vacuum Ultraviolet Radiation," *Journal of Chemical Physics*, vol. 38, no. 8, August 1963, pp. 910-925.

[29] R. E. Huffman, Y. Tanaka, and J. C. Larrabee, "Absorption Coefficients of Nitrogen in the 1000-580 Angstrom Wavelength Region," *Journal of Chemical Physics*, vol. 39, no. 4, April 1963, pp. 1920-1926.

[30] P. Lee, "Photodissociation and Photoionization of Oxygen (O_2) as Inferred from Measured Absorption Coefficients," *Journal of the Optical Society of America*, vol. 45, no. 9, September 1955, pp. 703-709.

[31] G. R. Cook, "Photodissociation Continuums of N_2 and O_2," Journal of Geophysical Research, vol. 78, no. 10, April 1973, pp. 1663-1667.

[32] W. H. Press, B. P. Flannery, S. A. Teukolsky, W. T. Wetterling, *Numerical Recipes*, Cambridge University Press, Cambridge, 1988, pp. 200-201.

[33] A. Beiser, *Concepts of Modern Physics*, McGraw-Hill, Inc., 1973, pp. 43-50.

[34] H. J. Wintle, "Photoelectric Effects in Insulating Polymers and their Relation to Conduction Processes," *IEEE Transactions on Electrical Insulation*, vol. EI-12, no. 2, April 1997, pp. 97-113.

[35] Y. Murata, "Photoelectric Emission and Contact Charging of some Synthetic High Polymers," *Japanese Journal of Applied Physics*, vol. 18, no. 1, January 1979, pp.1-8.

[36] N. Sato, H. Inokuchi, B. M. Schmid, "Ultraviolet Photoemission Spectra of Organic Single Crystals," *J. Chem. Phys.*, vol. 83, no. 11, December 1985, pp. 5413-5419.

[37] A. A. Guzhov and Yu. A. Shuba, "The Photoemission of Some Massive Insulators in the Vacuum Ultraviolet," *Optical Technology*, vol 38, no. 4, April 1971, pp. 198-199.

[38] A. V. Phelps, "Collision Cross Sections for Electrons with Atmospheric Species," *Ann. Geophys.*, vol. 28, no. 3, 1972, pp. 611-625.

Distribution:

4   Texas Tech University
     Attn: Prof. Andreas Neuber (1)
              Mr. John Krile (1)
              Prof. James Dickens (1)
              Prof. Hermann Krompholz (1)
     Department of Electrical and Computer Engineering
     P. O. Box 43102
     Lubbock, TX 79409-3102

1   Prof. Erich E. Kunhardt
     Department of Physics and Engineering Physic
     Stevens Institute of Technology
     Castle Point on Hudson
     Hoboken, NJ 07030

1   MS0188   D. Chavez, LDRD Office, 01011
5   MS1152   R. E. Jorgenson, 01642
10   MS1152   L. K. Warne, 01642
1   MS1152   M. L. Kiefer, 01642
1   MS1152   M. E. Morris, 01642
1   MS1152   M. Caldwell, 01643
1   MS1152   M. A. Dinallo, 01643
1   MS0319   S. D. Nicolaysen, 02613
1   MS0319   J. Brown, 02613
1   MS0316   H. P. Hjalmarson, 09235
1   MS0888   R. A. Anderson, 01843
1   MS0405   K. O. Merewether, 12333
1   MS0405   T. R. Jones, 12333
1   MS9018   Central Technical Files, 8945-1
2   MS0899   Technical Library, 09616
1   MS0612   Review & Approval Desk, 09612 For DOE/OSTI